

**DOSE CALCULATION METHODOLOGY FOR IRRADIATION TREATMENT  
OF COMPLEX-SHAPED FOODS**

A Dissertation

by

JONGSOON KIM

Submitted to the Office of Graduate Studies of  
Texas A&M University  
in partial fulfillment of the requirements for the degree of

DOCTOR OF PHILOSOPHY

August 2007

Major Subject: Biological and Agricultural Engineering

**DOSE CALCULATION METHODOLOGY FOR IRRADIATION TREATMENT  
OF COMPLEX-SHAPED FOODS**

A Dissertation

by

JONGSOON KIM

Submitted to the Office of Graduate Studies of  
Texas A&M University  
in partial fulfillment of the requirements for the degree of

DOCTOR OF PHILOSOPHY

Approved by:

Chair of Committee,	M. Elena Castell-Perez
Committee Members,	Leslie A. Braby
	Luis Cisneros-Zevallos
	Rosana G. Moreira
Head of Department,	Gerald L. Riskowski

August 2007

Major Subject: Biological and Agricultural Engineering

**ABSTRACT**

Dose Calculation Methodology for Irradiation Treatment of Complex-shaped Foods.

(August 2007)

Jongsoon Kim, B.S., Seoul National University, Korea;

M.S., Seoul National University, Korea

Chair of Advisory Committee: Dr. Elena Castell-Perez

Dose calculation methodology was developed for irradiation treatment of complex-shaped foods. To obtain satisfactory electron beam irradiation of food products, a strict process control is required to ensure that the dose delivered to all parts of the treated product falls within some specified range. The Monte Carlo electron transport simulation and computer tomography (CT) scan technology were used to predict the dose distribution in complex shaped foods, an apple phantom composed of paraffin wax, chloroform, and methyl yellow, and a chicken carcass. The Monte Carlo code used was successfully tested against the experimental data, resulting in less than 5% discrepancy between the simulated and measured data.

For 1.35 MeV electron beam simulation of apple phantom, tilting and axial rotation ensures dose distribution of the entire surface of the phantom, even reaching the critical regions of the apple stem and calyx ends. For 1 and 5 MeV X-ray simulations, both depth-dose curves show exponential attenuation after a build-up region. The depth to peak for the former is shorter than that of the latter.

For 1.35 MeV electron beam simulation of a chicken carcass, dose adsorption occurred up to 5-7 mm deep, resulting in surface irradiation of the carcass. For 10 MeV electron beam simulation, the doses within the carcass reached a peak of 1.2 times the incident dose with increasing depth. Two-sided X-ray (5 MeV) irradiation significantly improved the dose uniformity ratio, from 2.5 to 1.8.

A web-based integrated system was developed for data manipulation and management for irradiation treatment of foods. Based on CT scan, three dimensional geometry modeling was used to provide input data to the general Monte Carlo N-Particle (MCNP) code. A web-based interface provided the on-line capability to formulate input data for MCNP and to visualize output data generated by MCNP. The integrated Matlab and Matlab Web Server programs automatically functions through the steps and procedures for data input and output during simulation. In addition, a database having  $D_{10}$  values (decimal reduction value), food nutrition composition, and qualities was integrated into the dose planning system to support food irradiation treatment.



**DEDICATION**

To my parents, Kim, Dong Bae and Han, Hyun Sook

To my parents-in-law, Cho, Mun Sook and Park, Soon Ja

## ACKNOWLEDGEMENTS

I would like to thank my advisor, Dr. Elena Castell-Perez, for providing me with constant support in research and in other matters related to my graduate study. I am also deeply grateful to Dr. Rosana Moreira. She has not only given me the challenges which I could use to see my true potential, but also showed me the working attitude (“enthusiasm”) toward research. I would like to thank Dr. Leslie Braby for his advice and support about radiation physics and dosimetry. He has helped me develop a passion for that area. It was really a great experience for me to be working with him. I also thank Dr. Luis Cisneros-Zevallos for serving on my committee.

I am also thankful for Mr. Tony Restivo for helping with the maintenance of the Van de Graaff electron accelerator. His work experience was valuable. I will not forget my two friends, Giovanni Brescia and Ramiro Rivadeneira, who had worked together during the whole installation period of the electron accelerator. I am indebted to Dr. Yanbo Huang for his help with the installation of MCNP and the image processing of CT scan samples.

I would like to thank my colleagues in the Food Engineering Lab, Jaejoon Han, Paulo Da Silva, and Carmen Gomes, for their friendship and encouragement. I will always remember them.

Finally, I would like to thank my parents and my wife, Eun Hye, for their continuous and tremendous support during my long period of study for my Ph.D. degree. Without their support, I could not have come this far.

## TABLE OF CONTENTS

	Page
ABSTRACT.....	iii
DEDICATION.....	v
ACKNOWLEDGEMENTS.....	vi
TABLE OF CONTENTS.....	vii
LIST OF FIGURES.....	xii
LIST OF TABLES.....	xvii
 CHAPTER	
I INTRODUCTION.....	1
II LITERATURE REVIEW.....	4
2.1 Electron Beam Accelerators .....	4
2.1.1 Electrostatic (Van de Graaff) Electron Accelerator .....	4
2.1.2 Radio Frequency (RF) Electron Accelerator .....	7
2.1.3 X-ray Converter .....	9
2.2 Dosimetry in Food Irradiation Processing .....	10
2.2.1 Radiochromic Film Dosimeters .....	11
2.2.2 Alanine-ESR Dosimeters .....	13
2.2.3 Applicability for Food Irradiation Processing .....	13
2.3 Mathematical Methods for Dose Calculation .....	14
2.3.1 The Monte Carlo Method .....	15
2.3.2 Deterministic Methods .....	17
2.3.2.1 Discrete Ordinates Methods .....	17
2.3.2.2 Point Kernel Methods .....	18
2.3.3 Empirical and Semi-empirical Methods .....	18
2.3.4 Applications in Food Irradiation Processing .....	19
2.4 CT Scan Applications in Food Engineering .....	21
2.4.1 General Description of Computed Tomography (CT) ....	21
2.4.2 Third-generation CT Scanner .....	22
2.4.3 X ray Source in CT Scanner .....	25
2.4.4 X-ray CT Scan Applications in Food Engineering .....	25
2.5 Graphic User Interface (GUI) for Food Processing and Food Irradiation .....	27



CHAPTER	Page
4.4 Results .....	79
4.4.1 Dose Calculation Comparison Between the Phantom and an Actual Apple .....	79
4.4.2 Dose Measurement Using the Phantom Dosimeter .....	84
4.4.3 Rotation Strategies for Uniform Dose Distribution in Target .....	87
4.4.4 Simulated Dose Distribution in the Phantom .....	87
4.5 Conclusions .....	91
 V MONTE CARLO-BASED FOOD IRRADIATION SIMULATOR	 92
5.1 Overview .....	92
5.2 Introduction .....	93
5.3 Materials and Methods .....	95
5.3.1 Paraffin Apple-Phantom .....	95
5.3.2 3-D Image Reconstruction .....	96
5.3.2.1 CT Scanning .....	96
5.3.2.2 Reconstruction of CT-based Phantom .....	96
5.3.3 Monte Carlo Simulation .....	98
5.3.4 Dose Distribution Measurement .....	101
5.4 Results and Discussion .....	104
5.4.1 Dose Distributions of an Apple Phantom at 10 MeV Electron .....	104
5.4.2 Dose Distribution Simulation of a Real Apple at 1 and 5 MeV X-rays .....	110
5.5 Conclusion .....	117
 VI 3-D DOSE DISTRIBUTIONS FOR OPTIMUM RADIATION TREATMENT PLANNING OF COMPLEX FOODS .....	 118
6.1 Overview .....	118
6.2 Introduction .....	119
6.3 Materials and Methods .....	120
6.3.1 CT Data Acquisition .....	121
6.3.2 CT Data Visualization .....	122
6.3.3 CT Data Processing .....	123
6.3.4 3-D Geometric Reconstruction .....	126
6.3.5 Monte Carlo Simulation .....	128
6.3.6 Dose Distribution Measurement .....	133
6.4 Results .....	133
6.4.1 3-D Reconstruction of Food Products Using CT Scan Data .....	133

CHAPTER	Page
6.4.2 Dose Comparison of Chicken Carcass between Simulated and Experimental Data .....	135
6.4.3 Dose Distribution Simulations of Chicken Carcass at 1.35 MeV Electrons .....	139
6.4.4 Dose Distribution Simulations of Chicken Carcass at 10 MeV Electrons .....	139
6.4.5 Dose Distribution Simulations of Chicken Carcass at 5 MeV X-rays .....	145
6.5 Conclusions .....	149
VII A WEB-BASED INFORMATION SYSTEM FOR MCNP SIMULATION OF IRRADIATION OF COMPLEX SHAPED FOODS .....	150
7.1 Overview .....	150
7.2 Introduction .....	151
7.3 Background .....	152
7.3.1 Monte Carlo Method .....	152
7.3.2 Particle Transport Simulation Codes .....	153
7.3.3 Monte Carlo N-Particle (MCNP) Code .....	153
7.3.4 CT-based Geometric Modeling .....	154
7.3.5 GUIs of Simulation Codes .....	155
7.4 Materials and Methods .....	156
7.4.1 Food Products .....	156
7.4.2 CT Data Acquisition .....	156
7.4.3 CT Data Processing and Visualization .....	156
7.4.4 Information System Modules .....	157
7.4.4.1 MCNP Input Generation .....	157
7.4.4.2 MCNP Output Visualization .....	159
7.4.4.3 Food Irradiation Database .....	159
7.4.5 Information System Interface .....	159
7.4.6 System Server .....	160
7.4.7 System Structure .....	162
7.5 System Testing and Demonstration .....	162
7.5.1 MCNP Input Demonstration .....	165
7.5.2 MCNP Output Demonstration .....	168
7.5.3 Food Irradiation Database Demonstration .....	179
7.6 System Application Example With Broccoli .....	179
7.6.1 MCNP Input File Generation for Broccoli Simulation ....	184
7.6.2 Broccoli Output Visualization .....	187
7.7 Conclusion .....	194

CHAPTER	Page
VIII CONCLUSIONS .....	195
IX RECOMMENDATIONS FOR FURTHER STUDY .....	198
REFERENCES .....	199
APPENDIX A .....	216
APPENDIX B .....	218
VITA .....	225

## LIST OF FIGURES

FIGURE	Page
2.1 Schematic diagram of a Van de Graaff accelerator (Miller, 2005) .....	6
2.2 Principle of a linear accelerator (Hellborg, 2005) .....	8
2.3 Schematic illustration of CT work (ASTM, 2002a) .....	23
2.4 Third-generation CT scanner geometry (Hsieh, 2003) .....	24
2.5 <i>Escherichia coli</i> O157:H7 survival curve at beef tartar irradiated with gamma rays using Pathogen Modeling Program 7.0 (UDSA ARS, 2007) .....	29
3.1 Part of broccoli CT data file .....	32
3.2 Original CT slice deck of a Roman tomato .....	33
3.3 A CT image of a Roman tomato, showing artifact (tapes) .....	34
3.4 A processed CT image of a Roman tomato .....	36
3.5 All processed CT slices of a Roman tomato .....	37
3.6 Isosurfaces of a chicken carcass from CT data .....	39
3.7 Cutaway of a chicken carcass from CT data .....	40
3.8 Flow diagram of electron transport (Bielajew, 2001) .....	45
3.9 Beam scanning configuration at 10 MeV linac .....	57
3.10 Reference and body-attached coordinate system (Fu, Gonzales, & Lee, 1987) .....	59
3.11 Rotation of an apple phantom: (a) original position, and (b) rotation of 45 angle about <i>OX</i> axis followed by rotation of 30 angle about <i>OW</i> axis .....	62
4.1 Scanning electron beam .....	73



FIGURE	Page
4.2 Placement of the phantom dosimeter in front of the electron beam exit window .....	74
4.2 Placement of the phantom dosimeter in front of the electron beam exit window .....	74
4.3 The phantom and its regions: 0° and 180° corresponding to the right and left position, and 90° and 270° correspond to the top and bottom position, respectively .....	78
4.4 Total stopping power (TSP) of an actual apple and the phantom (paraffin apple) with corresponding electron energy .....	80
4.5 Simulated dose distribution for a 1.35 MeV e-beam source in the phantom (top) and an actual apple (bottom) .....	82
4.6 Depth-dose curves in the phantom (paraffin apple) and the actual apple for a 1.35 MeV e-beam source .....	83
4.7 Top: Density distribution in (a) actual apple; and (b) phantom. Bottom: Phantom: (a) before irradiation; (b) after irradiation; (c) vertical (y-z) plan view after irradiation .....	85
4.8 Simulated (top) and measured (bottom) dose contour maps in the phantom for a 1.35 MeV e-beam source. The target was rotated by its axis around the e-beam source .....	86
4.9 Simulated dose distribution in the phantom dosimeter for a 1.35 MeV e-beam source. Target rotated twice: (Top) first round the axis (up and down positions); (Bottom) second at an angle in front of the source, 0 and 180° .....	89
5.1 The steps required for the development of the 3-D image of a Red Delicious apple .....	97
5.2 Schematic representation of the experimental setup for irradiation of the apple using (a) 10 MeV LINAC in dual e-beam mode and (b) schematic of simulation setup of a broad parallel photon beams incident in an apple (1-5 MeV X-ray LINAC) .....	99

FIGURE	Page
5.3 Experimental setup for the apple phantom with 3 cm thick Lucite as attenuation material (target dose of 1 kGy). The Lucite material was placed on the top and bottom of the boxes and the phantom between the Lucite blocks .....	103
5.4 Simulated results of apple phantom with a 10 MeV e-beam source operating in dual mode for a conveyor speed of 0.3 m/s: (a) dose distribution (kGy) over the whole phantom; (b) dose distribution versus penetration depth (at different vertical planes of the phantom); (c) dose distribution versus penetration depth at different horizontal planes (beam source operating in single beam mode – top beam with conveyor speed of 0.3 m/s) .....	105
5.5 Dose distribution versus penetration depth (at different vertical planes of the phantom) for the phantom apples irradiated with a 10 MeV e-beam source using a 3 cm Lucite shielding material. Continuous lines indicate dose measured (RCF) and dots indicate dose calculated using MCNP5 .....	107
5.6 Experimental versus simulated results for the phantom apples irradiated with a 10 MeV e-beam using a 3 cm Lucite shielding material: (a) RCF after irradiation, (b) dose distribution calculation in the RCF using a flat scanner; and (c) simulation dose distribution using MCNP5 .....	108
5.7 Dose distribution (kGy) in an actual apple using: (a) 1 MeV photons and (b) at the vertical planes (2.6 cm and 4.1 cm); (c) 5 MeV photons and (d) at the vertical planes (2.6 cm and 4.1 cm) .....	112
6.1 Relationship between CT values and material densities .....	122
6.2 (a) Original CT slice deck of an apple: (b) Artifacts (paper towel, adhesive tape, and sample holder) showing in one of the CT slices of apple .....	124
6.3 (a) The ROI of the CT slice of apple; (b) Processed CT slice deck of the apple .....	127
6.4 (a) 3-D reconstruction of the apple with the CT slices; (b) 3-D subvolume reconstruction of the apple with the CT slices .....	129

FIGURE	Page
6.5 Electron beam direction in a chicken carcass for simulation of dose distribution using low (1.35 MeV) and high (10 MeV) energy e-beam source .....	131
6.6 Calculated X-ray spectra from the 5 MeV X-ray converter .....	132
6.7 3-D reconstruction of CT images using MATLAB, (a) a broccoli, (b) (a) a whole chicken .....	136
6.8 3-D reconstruction of CT images using Matlab showing internal composition, (a) a broccoli, (b) a whole chicken .....	137
6.9 Dose comparison between measured and simulated data in a whole chicken irradiated with a 10 MeV e-beam accelerator from an upper beam direction. Dose values evaluated at the horizontal points of 2.81 cm, 7.03 cm, and 11.95 cm .....	138
6.10 Simulated dose distributions (in kGy) of a whole chicken at 1.35 MeV electrons. (a) at upper beam direction, (b) at lower beam direction, (c) at upper and lower beam directions, (d) at the horizontal point (8.44 cm) .....	140
6.11 Simulated dose distributions (in kGy) of a whole chicken at 10 MeV electrons. (a) at upper beam direction, (b) at lower beam direction, (c) at double beam directions, (d), (e), and (f) at the horizontal point (7.03 cm) .....	142
6.12 Dose distribution (in kGy) of a whole chicken at 5 MeV X-rays: (a) at right beam direction, (b) at left beam direction, (c) at double beam directions, (d), (e), and (f) at the vertical point (7.03 cm) .....	146
7.1 Schematic diagram of a Matlab Web Server application .....	161
7.2 Structure of web-based information system for MCNP simulation of food irradiation .....	163
7.3 Front page of the web-based information system for MCNP simulation of food irradiation .....	164
7.4 Food product list page in the MCNP input module .....	166
7.5 Apple parameter specification page for MCNP simulation input .....	167

FIGURE	Page
7.6 Product page of MCNP simulation input generation for an apple .....	169
7.7 Product pages of MCNP simulation input generation for a (a) bunch of broccoli, (b) cantaloupe, (c) chicken, and (d) pomelo .....	170
7.8 Product page of MCNP simulation output visualization for an apple phantom .....	174
7.9 Product pages of MCNP simulation output generation for a (a) bunch of broccoli, (b) cantaloupe, (c) chicken, and (d) pomelo .....	175
7.10 The microorganism ( <i>Clostridium sporogenes</i> ) survival rate data (D- value) of mushroom .....	180
7.11 Broccoli's nutritional data and chemical composition (USDA, 2006) ...	181
7.12 Papaya's quality data .....	182
7.13 Self calculation of papaya's firmness: (a) the dose input and (b) the firmness calculation output .....	183
7.14 xyz coordinates for the scanned broccoli's position .....	185
7.15 Particle trajectories at 10 MeV electrons with 100 particle histories ; (a) upper beam direction, (b) lower beam direction .....	186
7.16 Broccoli's CT scan images .....	188
7.17 Density distribution of a broccoli head .....	189
7.18 Energy distribution around the broccoli head using 1.35 MeV electron source .....	190
7.19 Energy distribution around the broccoli head using 10 MeV electron source (LINAC) .....	192
7.20 Energy distribution around the broccoli head using 5 MeV X-rays source .....	193

**LIST OF TABLES**

TABLE	Page
4.1 The elemental composition and density of an actual apple and the phantom .....	71
5.1 Input parameter for the apple simulation .....	101
5.2 Output properties obtained by simulation of a real apple irradiated by 1 and 5 MeV X-rays .....	114
6.1 Input parameters for chicken carcass simulation .....	134
6.2 Material composition (%/weight) .....	134

## CHAPTER I

### INTRODUCTION

Numerous outbreaks of illness caused by bacteria, viruses, and parasites have been linked to consumption of raw fruits and vegetables and processed meat and poultry, which have been vehicles for transmission of pathogens. Thus, methods for decontamination of fresh produce are needed. One alternative is radiation treatment using gamma rays, electron beam, or X-rays.

The electron beams generated by accelerators have the ability to penetrate the product to a limited depth depending on the density and product characteristics. Gamma rays and X-ray are used to relatively thick and dense foods to achieve acceptable dose uniformity, since they have greater penetrating capability. For best results, all of the food has to receive the dose sufficient to produce desired irradiation effects, and none of it has to receive an excessive dose which might alter color, texture, flavor, or nutritional component.

The correct procedure for food irradiation processing depends to a large extent on accurate and reproducible measurement of radiation quantities. When irradiation is done on a commercial scale, due to the large dose uniformity ratio, a majority of the food item will receive significantly greater than the minimum absorbed dose.

Dose distributions are needed in determining positions of minimum and maximum dose inside the food to guarantee that all the food products will attain the

---

This dissertation follows the style and format of *Journal of Food Engineering*.

minimum required dose. When using conventional dosimetry technique, it is difficult to know exactly how much energy is absorbed in each element of the whole target, because of dosimeter's geometry limitation, poor accuracy and precision, and their nonlinearity with response energy. Even though several radiation transport computer codes have been developed and/or adapted for dose distribution calculation in radiation processing, they do not adequately account for the complex 3-D structure and non-homogeneity of foods. The main difficulty in applying those codes for complex-shaped foods lies in obtaining the actual product geometry and density values, which are critical factors in evaluation of electron/photon interactions.

Computed tomography (CT) scan is a diagnostic test that combines the use of X-ray with computer technology. The combination of CT scan, which provides the geometrical and density information of food item, with Monte Carlo simulation could provide detailed and high resolution dose maps for complex-shaped foods.

Calculation and measurement of dose in the same object is required to determine the precision of dose distributions calculated by mathematical models. Since a real food object would deteriorate during dose measurement, it is vital that we validate with a dependable food-substitute material (plastic or wax) that mimics the geometric and chemical properties of the food that are relevant to dosimetry. This food-substitute material can then be shaped into the desired 3-D geometry using molding technology.

Consequently, developments of accurate dose calculation methodology are needed for producing more high quality and safe irradiated food. Through a good irradiation planning based on the developed methodology, the increased shelf life and

improved quality of the food products would significantly reduce the economical losses from spoilage and would even allow for overseas marketing.

The main goal of this research was to develop a treatment planning to accurately predict dose distribution in complex-shaped foods.

The specific objectives were:

1. To develop a methodology to predict dose distribution of complex-shaped foods using the combination of computed tomography (CT) scanning with Monte Carlo simulation technique.
2. To validate the dose prediction methodology using phantoms exposed to low (1.35 MeV) and high (10 MeV) electron beams.
3. To simulate dose distribution in real complex-shaped food, such as chicken carcass, exposed electron beams (1.35 and 10 MeV) and X-rays (5 MeV).
4. To develop a user-friendly computer software package for food irradiation treatment using a web-based graphic user interface (GUI).



## **CHAPTER II**

### **LITERATURE REVIEW**

#### **2.1 Electron Beam Accelerators**

Electron accelerators generate electrons and X-rays that deliver ionizing dose to food products. All electron accelerators consist of two essential features: electron generation and acceleration. Electron generation technique in all accelerators is the same. Electrons are always generated from an electron gun, the cathode of which is raised to a sufficiently high temperature that electrons are emitted from the surface. In contrast, many different techniques have been used for accelerating electrons.

There are two categories of electron accelerators for food irradiation process: (1) direct methods, in which the accelerating field results from the direct application of a high potential difference across an insulating column; and (2) radio frequency methods, in which accelerating field results from oscillating electromagnetic fields established in a resonant microwave cavity structure (Miller, 2005). In this chapter, we will discuss characteristics of these accelerators, including their general operating principles.

##### **2.1.1 Electrostatic (Van de Graaff) Electron Accelerator**

The simplest direct acceleration method to visualize is that of the electrostatic accelerators. This approach establishes a large potential difference by physically transferring charge to a high voltage terminal.

A schematic of a Van de Graaff electron accelerator is illustrated in Fig. 2.1. The high-voltage terminal and the grounded pressure vessel constitute the two plates of a capacitor. The belt charge unit draws electrons from ground by an electric circuit and sprays them onto the belt by a corona discharge. These electrons are carried to the top where they are removed by a collector and deposited on high voltage terminal. The electron gun takes electrons from the high voltage terminal and emits them into the accelerator tube. The accelerator tube with its electrostatic field accelerates the electrons to an energy level determined by the voltage of the high-voltage terminal (High Voltage Engineering Corporation, 1954). This voltage is determined according to  $V=Q/C$ , where  $Q$  is the net transfer charge and  $C$  is the capacitance between the high voltage terminal and ground.

If the voltage delivered by a high voltage terminal to an accelerating tube is  $V$ , a particle that has a charge  $q$  acquires the kinetic energy given by

$$E_k = qV \tag{2.1}$$

Energy of one electron volt (eV) is gained by an electron where it is accelerated in an electric field whose potential difference is 1 V, thus  $1 \text{ eV} = 1.6 \times 10^{-19} \text{ J}$  since electron charge is  $1.6 \times 10^{-19} \text{ C}$ .

Van de Graaff accelerators provide beams of high quality since they feature a comparatively small scatter and high terminal energy stability. Another advantage is that they produce no ripple voltage which is one of the main characteristics of other high

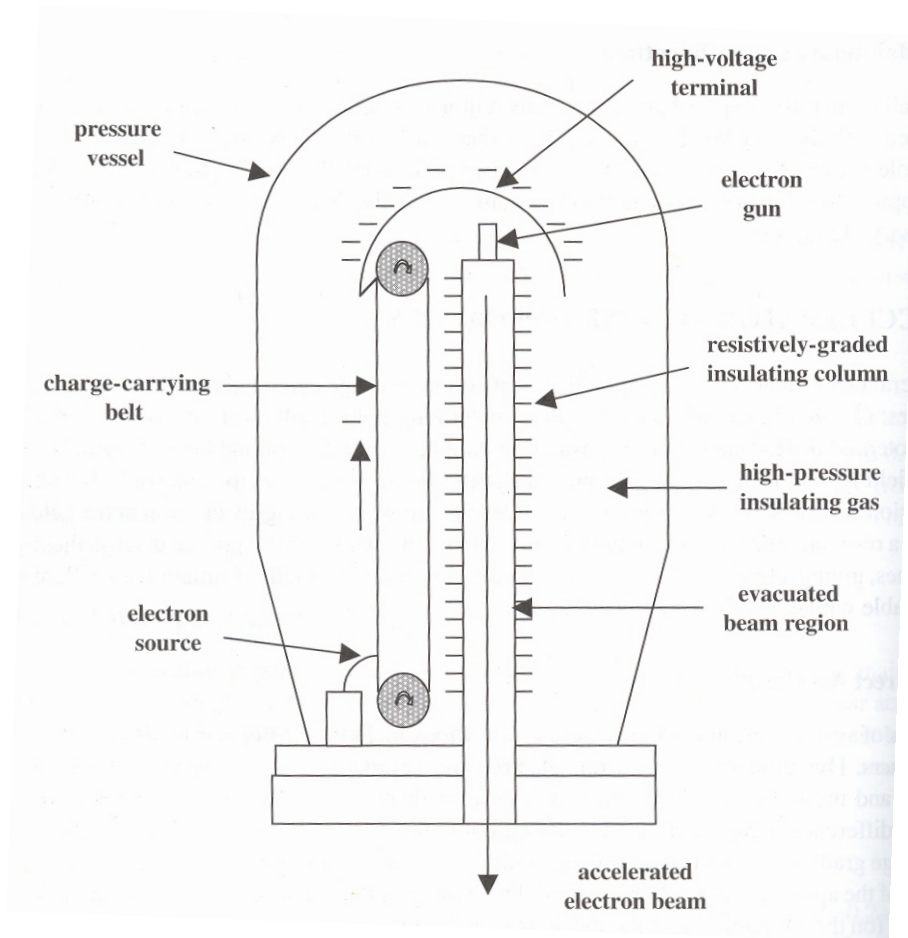


Fig. 2.1. Schematic diagram of a Van de Graaff accelerator (Miller, 2005).

voltage accelerators. They are quite large, however, and maintaining the insulating column and repairing the charge transfer apparatus can be laborious (Miller, 2005).

Even though 70 years have passed since the first machine constructed, the Van de Graaff accelerator is still used in basic research in nuclear physics, radiation therapy, and food processing (Wilson, 2001). More recently Rivadeneira (2004) used a 2 MeV Van de Graaff electron accelerator for surface irradiation of complex-shaped food.

### **2.1.2 Radio Frequency (RF) Electron Accelerator**

Radio frequency linear accelerators (LINAC) are more powerful and efficient than electrostatic accelerators. Fig. 2.2 shows the principle of a linear accelerator. Electrons are produced in an electron gun. They are emitted from a cathode, and formed into a pencil beam. Upon entering the interior of an electrode, electrons drift in a field-free region for a time equal to half the period of the RF voltage. While electrons are within the drift tube, the polarity of the voltage is reversed and the electrons are then accelerated as they cross the next gap (Hellborg, 2005). In this way, a much bigger energy gain is obtained compared with the acceleration voltage. Since these processes are done in a series of drift tube in a straight line, it is called a linear accelerator (LINAC).

A klystron is a linear beam device that uses the principle of velocity modulation to generate radio frequency pulses. When used in a linac system for food irradiation, it is operated at a voltage of the order of 100 kV, generating 5 MW pulses at average power levels (Miller, 2005).

Unlike Van de Graaff accelerators, the linac system is modular with components that can be quickly replaced in the event of failure. However, the radio frequency source operates in pulsed mode, so voltage fluctuation affects both the electron kinetic energy and the delivered dose; 1% of voltage change causes 1.1% change in beam kinetic energy and 4.8% change in dose (Miller, 2005). Nevertheless, linacs have the flexibility to process almost every type of food product in an effective manner in facilities of reasonable size and cost.

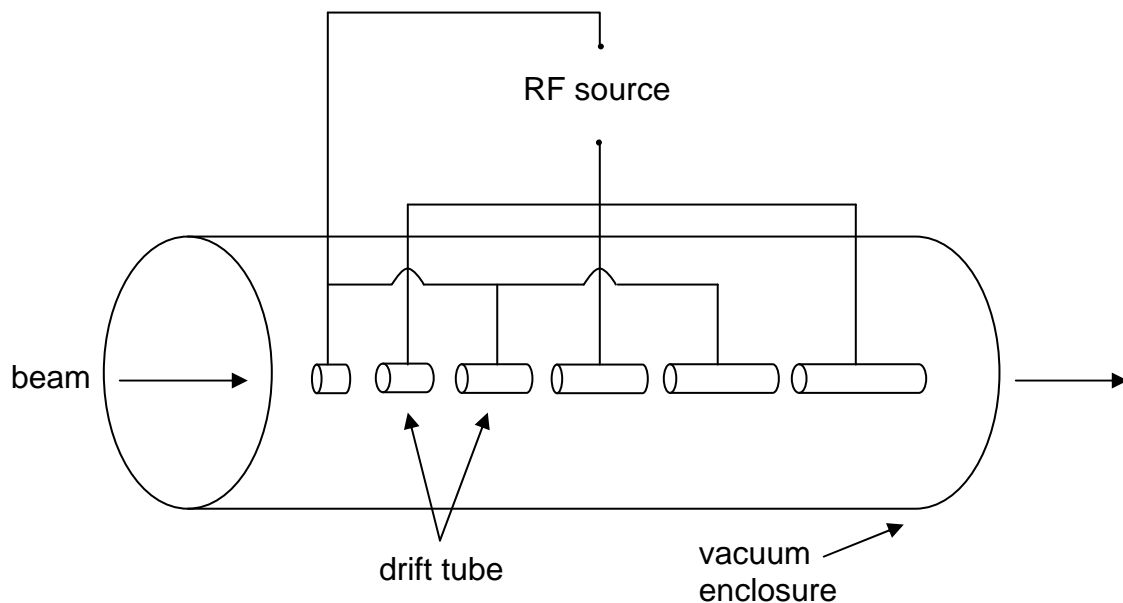


Fig. 2.2. Principle of a linear accelerator (Hellborg, 2005).

### 2.1.3 X-ray Converter

X-rays in food irradiation processing are generated using the same electron accelerators, such as a linac, but afford considerably more flexibility because of their greater penetrating power.

The bremsstrahlung X-rays are generated by accelerating an electron beam and allowing it to strike a metallic target. The X-ray energy production increase with the kinetic energy of the electron and the atomic number ( $Z$ ) of the target (Attix, 1986). Therefore, the converter should be made of high  $Z$  material, but one with good thermal conductivity and a high melting point because most of the electron energy is deposited in the target and appears as heat. Tantalum (Ta,  $Z = 73$ ), Tungsten (W,  $Z = 74$ ), and Gold (Au,  $Z = 79$ ) are widely used for converter materials.

The X-ray converter for food irradiation processing consists of a thin layer of high  $Z$  material and a thick layer of low  $Z$  material (Meissner et al., 2000). The thickness of high  $Z$  material should maximize the forward-going X-ray fluence. The second layer, the low  $Z$  material, is chosen such that X-ray self absorption is minimized and all primary electrons are stopped; otherwise, the surface of the product will receive a low energy electron overdose. Aluminum is good for the second layer, because it has low X-ray absorption coefficient over the operating energy range and good thermal conductivity. In addition, an aluminum backplate can be easily cooled with flowing water (Miller, 2005).

In X-ray radiation therapy, a flattening filter is used to make X-ray beam intensity uniform (Khan, 1984). However this decreases the penetrating power of an X-

ray beam (Podgorsak, Rawlinson, & Johns, 1975). Thus filters are not used in X-ray generation for food irradiation processing.

## **2.2 Dosimetry in Food Irradiation Processing**

The effectiveness of ionizing radiation in food processing applications depends on proper delivery of absorbed dose. Reliable techniques for measuring dose, called dosimetry, are also crucial for ensuring the integrity of the irradiation process. There are four categories of dosimetry system, according to their intrinsic accuracy and usage: (1) primary standard dosimeters, (2) reference standard dosimeters, (3) transfer standard dosimeters, and (4) routine dosimeters (ASTM, 2002c).

Primary standard dosimeters use basic scientific principles, thus do not require calibration against other standards. These dosimeters are established and maintained by national standards laboratories for calibration of radiation environments. The two most commonly used primary standard dosimeters are ionization chambers and calorimeters.

Reference standard dosimeters provide high quality dose measurements, and are used to calibrate routine dosimeters. They are also used in routine dosimetry applications when high quality measurements are necessary. The alanine dosimeters, and various liquid chemicals that form stable radiolytic byproducts with yields proportional to the absorbed dose, are widely used in food irradiation as reference standard dosimeters.

Transfer standard dosimeters are especially selected for transferring dose information from accredited or national standard laboratories to an irradiation facility to establish traceability. These dosimeters should be sufficiently precise and stable. Most

reference dosimeters and some routine dosimeters can be used as transfer standard dosimeters.

Routine dosimeters are used in radiation processing facilities for dose mapping and process monitoring. They are typically the least accurate, but are easy to use, low in cost and available in relatively large quantities. They must be frequently calibrated against reference or transfer dosimeters, because they show significant variations from batch to batch. Radiochromic film dosimeters are used for routine dosimeters in food irradiation processing.

The following section presents a summary of the most common dosimeters used in food irradiation processing (dose range of 0.1-10 kGy).

### **2.2.1 Radiochromic Film Dosimeters**

Various radiochromic dyes, which become colored on exposure to ionizing radiation, have been successfully developed as dosimeters. These dyes are mainly hydrophobic-substituted triphenyl methane leucocyanides that undergo a heterolytic bond scission of the nitrile group, which forms a highly colored dye salt in solid polymeric solution. These molecules require a host material for film development, which normally consists of a styrene, vinyl, or nylon based polymer (McLaughlin, 1970).

Radiochromic film dosimeters, generally, have long shelf lives and a simple read-out procedure using a spectrophotometer. The wavelength of the peak used in a spectrophotometer is dependent on the specific dye. These dosimeters, however, must be protected from UV (Ultra Violet) or fluorescent light and humidity changes, and should



therefore be hermetically sealed in light-tight pouches. Their optical surfaces should not be touched or scratched. Coloration is not immediate and can take hours and days in some cases. In addition, incubation at elevated temperatures can significantly reduce the color development time, e.g., 15 min at 60 °C with B3<sup>®</sup> radiochromic dosimeters.

Radiochromic film dosimeters are readily available in the market. For example, B3 WINDose film dosimeters (GEX Corporation, Centennial, CO) use pararosaline cyanide dye which changes from clear to purple, and consist of thin plastic squares (approximately 1 cm × 1 cm) mounted in cardboard backing for relatively easy handling using tweezers (Miller, Batsberg, & Karman, 1988). They are packaged in poly-foil laminated pouch and suggested dose range is 2-80 kGy.

GAFCHROMIC<sup>®</sup> HD-810 film dosimeters (ISP Technologies Inc, Wayne, NJ) use aminotriphenyl-methane dye, which changes from clear to blue. Its size is 20.3 cm (8") × 25.4 cm (10") and thickness is approximately 0.1 mm. These sheets are readily cut and used for dose distribution in a two dimensional plane (Rivadeneira, 2004).

More recently, flat bed scanners have been used to obtain dose distribution of radiochromic film as quick, reliable, and inexpensive dosimetry devices (Alva, Mercado-Uribe, Rodríguez-Villafuerte, & Brandan, 2002; Aydarous, Darley, & Charles, 2001; Rivadeneira, 2004).

### **2.2.2 Alanine-ESR Dosimeters**

The interaction of ionizing radiation with organic compounds forms free radicals, which can serve as the basis for high quality dosimeters, provided that the concentration is precisely related to the absorbed dose. These dosimeters consist of the crystalline amino acid  $\alpha$ -alanine and small amounts of binder material, such as paraffin. The free radical concentration is stable because of trapping in the crystalline lattice (Regulla & Deffner, 1982). The free radical concentration can be measured by electron spin resonance (ESR) spectroscopy. Since this measurement is nondestructive, the alanine dosimeter can be used multiple times. The dose range of the alanine dosimeter is  $1-10^5$  Gy (ASTM, 2002d).

Two types of alanine dosimeters are commercially available: the pellet (Harwell dosimeter) (Harwell Dosimeter, LTD, Oxfordshire, UK) and films (Kodak's Biomax Alanine dosimeters) (Eastman Kodak Company, Rochester, NY). The humidity problem of the films has been solved with air-tight pouch, and they also provide the dose precision as good as that of the pellets. Only disadvantage of these dosimeters is cost. For example, the ESR spectroscopy is more expensive than a spectrophotometer, and both pellets and films are approximately \$1 each (Miller, 2005).

### **2.2.3 Applicability for Food Irradiation Processing**

Dose mapping is one of the typical applications for which dosimeters are used in a food irradiation facility. Dose mapping studies, determining the positions of minimum and maximum dose at product samples, need many dosimeters in a short time, so low

cost is highly desirable. Radiochromic film dosimeters meet this requirement; however, they have relatively low accuracy (5-10%). Alanine dosimeters are good choice for high quality dose measurement (accuracy of 2-3%) (Miller, 2005). However, as mentioned in the previous section, they are expensive, and alanine pellets are not well suited for electron kinetic energy measurement due to their height (approximately 3 mm). None of the dosimeters currently used in food irradiation processing satisfies those requirements for dose mapping.

Dose calculation using computer simulation could be a solution to this problem, because it provides two or three dimensional dose distribution with high accuracy. This approach is better than the conventional dose mapping studies, which focus on determining the positions of maximum and minimum dose zones at product samples (ASTM, 2003).

### **2.3 Mathematical Methods for Dose Calculation**

Radiation transport in matter has been an intensive subject of study since the beginning of the 20<sup>th</sup> century. When high energy X-rays, gamma rays, or electrons are incident on a medium, multiple interactions occur and give rise to secondary particles; the interactions include ionization that produces secondary electrons and photons of lower energies (Attix, 1986). After each interaction of a particle, its energy is reduced and further particles are generated. Those secondary particles undergo their own interactions until they dissipate by molecular excitation and thermal processes at very low energies.

Mathematical methods for radiation transport can be used to estimate the dose delivered to a small volume or point, and the angular distribution of all particles throughout the entire object. The dose distribution can be determined by calculations at different points within the object. There are three types of radiation transport models in use: Monte Carlo, deterministic, and empirical (semi-empirical) (ASTM, 2002b). Both Monte Carlo and deterministic methods are based on the detailed physics of the interaction of radiation with the matter.

### **2.3.1 The Monte Carlo Method**

The Monte Carlo method simulates the paths of particles such as electrons and photons and estimates dose by summing and averaging the histories of many particles. This calculation proceeds by constructing a series of trajectories, each segment of which is randomly chosen from a distribution of applicable processes. For example, the energy loss and angular deflection of the electron during each of the steps can be sampled from probability distributions based on the appropriate multiple scattering theories. By tracing a large number of particle histories, it is possible to track the interactions of individual particles in their passages through the matter and to obtain distributions of many desired physical quantities. The particle history is established as the particle undergoes the interactions, and it ends when the particle becomes absorbed, leaves the region of interest, or loses energy to a significant degree (Cashwell & Everett, 1959).

Unlike other methods, the Monte Carlo method can theoretically account for all particle transport and provide a faithful and accurate simulation of actual events.

Nowadays, the Monte Carlo method is the most widely used in simulating the actual radiation transport in complex three-dimensional geometry.

Monte Carlo calculations, however, require large amount of computing time to obtain satisfactory precision of dose estimates. To decrease computing time, approximate trajectories using large path length steps and a multiple-scattering approaches to particle deflection were used in Monte Carlo codes (Berger, 1963). Such approximation paths may cause significant errors, particularly when the particle tracks are generated in the vicinity of an interface, i.e., a surface separating two media of different compositions. The variance reduction technique improves the efficiency of the Monte Carlo method without increasing the computer effort. There are four classes of variance reduction techniques (Forster, Little, Briesmeister, & Hendricks, 1990): truncation methods, population control methods, modified sampling methods, partially-deterministic methods.

There are several codes available to calculate the transport of electrons and photons: Electron TRANsport through extended media (ETRAN) (Seltzer, 1991), Integrated Tiger Series (ITS) (Halbleib, Kensek, Valdez, Seltzer, & Berger, 1992), Electron Gamma Shower (EGS4) (Nelson, Hirayama, & Rogers, 1985), Monte Carlo N-Particle transport (MCNP) (Brown, 2003), PENetration and Energy Loss of Positrons and Electrons (PENELOPE) (Baro, Sempau, Fernandez-Varea, & Salvat, 1995), GEometry ANd Tracking (GEANT) (Agostinelli et al, 2003). These codes are continually being upgraded to improve accuracy.

### **2.3.2 Deterministic Methods**

Deterministic methods use mathematical equations (Boltzmann equation) to calculate the radiation field over all space as a function of radiation source and boundary conditions. The Boltzmann equation is an integro-differential equation describing the radiation transport. The equation is a continuity equation of the angular flux in the phase space consisting of three space coordinates of the geometry, the corresponding direction cosines, and the kinetic energy. This equation is derived by considering the mechanisms by which particles enter or leave any small volumes in space (NCRP, 2003).

Since the Boltzmann equation is, in general, extremely difficult to solve, several approximation methods have been devised to yield useful results. These methods usually simplify the description of particle transport and reduce the computational effort. However, the result is only valid for a given unit path length and does not account for scattered radiation from the rest of the problem (three-dimension). Besides, there is no estimate provided for any error. The next section discusses two of the most important methods to solve the transport equation.

#### **2.3.2.1 Discrete Ordinates Methods**

These approximation methods have been used for both electron and photon transport in one-dimension (Drumm, Fan, & Renken, 1991; Lorence, 1992). This name is given to several closely related techniques for obtaining approximate solutions to the transport equations that contain both integral and partial derivative terms. The methods visualize the phase space to be divided into many small boxes, and the particles move

from one box to another. These methods can be powerful for one dimensional problem with simple geometry; the problem geometry must be one of three basic geometries (rectangular, cylindrical, or spherical). However, problems with irregular boundaries are difficult to solve accurately with the discrete ordinate methods. Extension of this technique to two dimensions has been done by several researchers (Datta, Altekhar, Ray, & Morel, 1996; Drumm, 1997).

### **2.3.2.2 Point Kernel Methods**

Point kernel methods are used mainly for photon transport problems (Chilton, Shultis, & Faw, 1984). The radiation source is modeled by a large number of isotropic point sources. The total absorbed dose at a dose point is obtained by integrating the contribution from each of the point sources. The calculation takes account of the distance between the dose point and the source point, and approximates the contribution of scattered particles from surrounding materials through the use of a build-up factor. Build-up factors are theoretically calculated and sometimes fitted to empirical functions (ASTM, 2002b). More recently, this technique has been used to predict the dose around gamma and beta emitters (Janicki, Duggan, & Rahdert, 2001; Janicki & Seuntjens, 2004).

### **2.3.3 Empirical and Semi-empirical Methods**

These methods are the simplest techniques and may not rely on any computer codes at all. Empirical methods generally involve fitting an approximating function (for

example, polynomial) to the experimental data or Monte Carlo calculation result. The model equations are only useful for a specific facility or product, and their predictive capabilities are not generally transferable to other facilities or products. Simple equations exist for calculating the range of electrons (Cleland, Lisanti, & Galloway, 2004; Lisanti, 2004; Tabata, Andreo, & Shinoda, 1996) and electron energy loss (Tan & Heaton, 1994).

In semi-empirical methods, the fitting parameters are constrained so that the model satisfies one or more physical laws or rules. This characteristic enables the model to be more applicable over a wide range of energies and materials. The semi-empirical methods have been used to calculate absorbed dose in the sample irradiated by electrons (Tabata, Ito, Kuriyama, & Moriuchi, 1989; Vazquez-Polo, Valdivia, Abrego, Mijangos, & Garcia, 2002) or X-rays (Garth, 1989). Even though empirical and semi-empirical models are fast and do not require cross sections and build-up factors, they are difficult to implement for systems with complicated geometry.

#### **2.3.4 Applications in Food Irradiation Processing**

Mathematical methods for calculating absorbed dose have been applied to food irradiation processing. These methods determine dose distributions for photons emitted from  $^{137}\text{Cs}$  or  $^{60}\text{Co}$ , energetic electrons from particle accelerators, or bremsstrahlung X-rays generated by electron accelerators.

Several computer codes have been developed and/or adapted for dose distribution calculation in industrial gamma radiation processing (Piña-Villalpando &



Sloan, 1998; Stenger, Halmavánszki, Falvi, Fehér, & Demirizen, 1998) and electron beam processing (Rakhno & Roginets, 1998).

Currently, the maximum photon energy for food treatment is limited to 5 MeV, and scientific evidence proved that X-ray treatment of food up to 7.5 MeV can be safe (FAO/IAEA, 1995). Meissner et al. (2000) applied the Monte Carlo method (ITS) (Halbleib et al., 1992) to simulate the X-ray conversion process and to calculate dose distribution in homogeneous phantoms (stacked-polyethylene plates,  $49 \times 80 \times 40$  cm) at 5 and 7.5 MeV incident electron energies. At 7.5 MeV, the efficiency for producing X-rays and the optimum product thickness was higher than at 5 MeV.

McKeown et al. (1998) examined the feasibility of X-ray converters over the electron range 7 to 11 MeV. ITS and MCNP were used to calculate the depth-dose calculation, and its model product consisted of 80 cm cube of water.

Recently, the Monte Carlo simulation (GEANT) (Agostinelli et al., 2003) has been applied to predict the performance of X-ray irradiation systems (Stichelbaut, 2004a and 2004b). Dose mapping was obtained for product loaded on industrial pallets on both irradiation systems.

An empirical model was also developed for characterizing the X-ray depth-dose distribution (Miller, 2003); the model was compared with Monte Carlo calculations (ITS).

However, all these methods did not adequately account for the complex three dimensional structures of foods, since most geometry was confined to the conventional shapes and sizes used in the commercial food irradiation processing.

More recently, a few researchers calculated dose distribution of complex-shaped foods using Monte Carlo simulation. Bresica, Moreira, Braby, and Castell-Perez (2003) used MCNP to determine the dose distribution at the surface of an apple irradiated with electron beams. The apple geometry was constructed by joining two spheres. However, such approximate geometry did not provide an accurate description of real food geometry.

Borsa et al. (2002) combined CT scanning and radiation treatment planning program to generate dose maps in irradiated foods such as frozen whole chicken, cured ham, and boxed frozen ham. This clinical radiotherapy technique could provide detailed and high resolution dose maps for complex-shaped fruit and vegetables.

## **2.4 CT Scan Applications in Food Engineering**

### **2.4.1 General Description of Computer Tomography (CT)**

A computed tomography (CT) scan uses X-rays to produce detailed pictures of structures of the target. Because of the relatively good penetrability of X-ray, CT permits the nondestructive physical characterization of the internal structure of the materials.

CT uses a computer to reconstruct an image of a cross-sectional plane through the object. The resulting cross-sectional image is a quantitative map of the linear X-ray coefficient at each point of the plane. The linear X-ray attenuation coefficient is proportional to material density, which is of course a fundamental physical property of all matter. CT information is obtained from a large number of measurements of X-ray

transmission at different viewing angle, and an image is then reconstructed with the aid of a computer (ASTM, 2002a).

Fig. 2.3a shows X-ray measurements made on an object containing two attenuating disks of different diameters. The X-ray attenuation measurement made at a particular angle, which is referred to as a single view. Fig. 2.3b, unlike Fig. 2.3a, shows measurements taken at several different angles  $f_{\phi_i}(x')$ . Each attenuation measurement is digitized and stored in a computer, where is subsequently conditioned and filtered. The next step in CT image processing is to reconstruct the view. Backprojection, the standard reconstruction method, consists of projecting each view back along a line corresponding to the direction in which the projection data were collected. The backprojections, when enough views are employed, form a faithful reconstruction of the object (ASTM, 2002a).

#### **2.4.2 Third-generation CT Scanner**

Since the development of the CT scanner in 1971 (Hounsfield, 1980), tremendous advancements have been made in CT technology. The third-generation CT, one of the most popular scanner types, is illustrated in Fig. 2.4. In this configuration, the sets of readings taken are in the form of a fan. A curved detector array consisting of sufficiently large detectors is mechanically coupled to the X-ray source, and both rotate together. This rotation-only mechanism is able to significantly reduce the data acquisition time; however, the X-ray fan beam must be wide so that the entire object is within the detector field at all times (Hsieh, 2003).

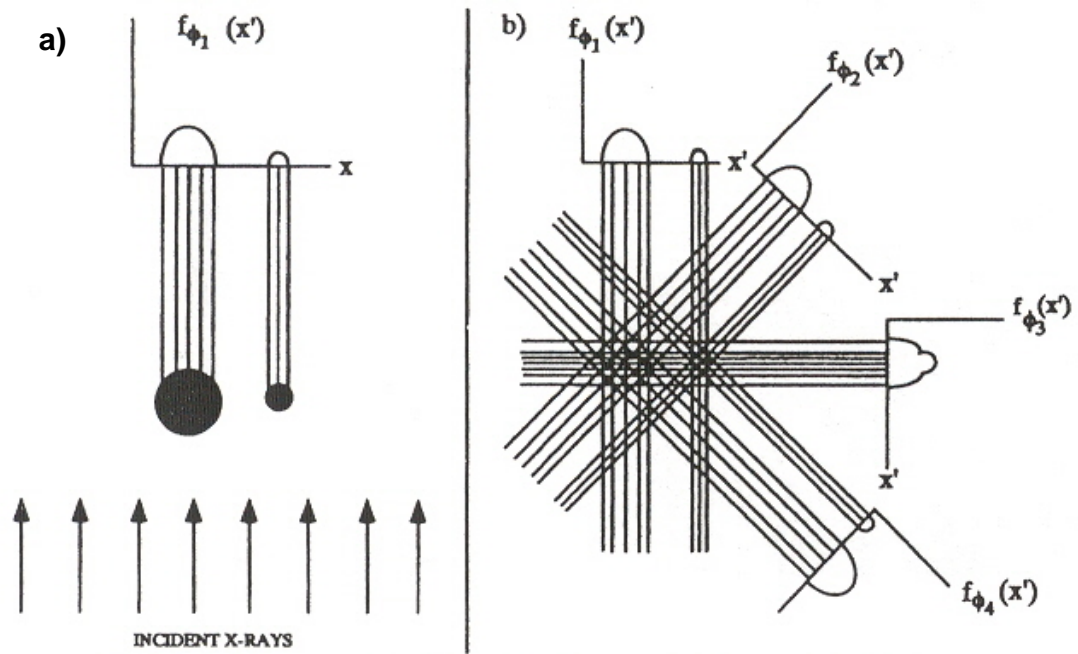


Fig. 2.3. Schematic illustration of CT work (ASTM, 2002a).

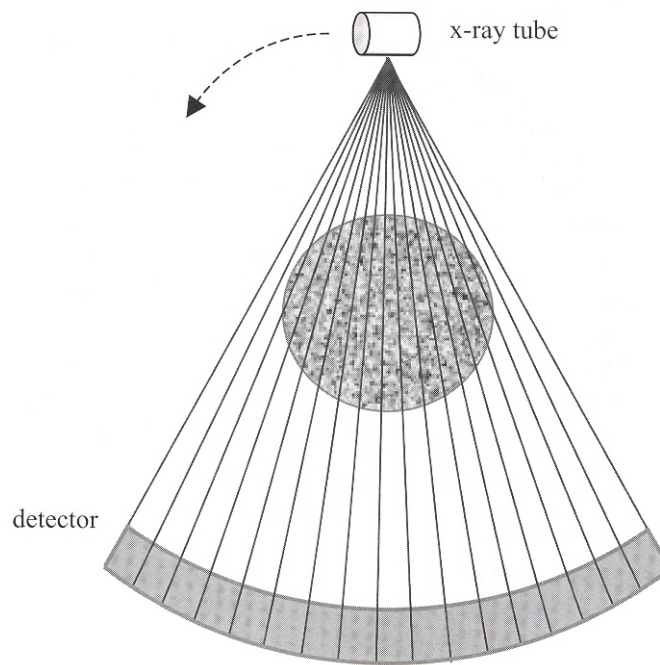


Fig. 2.4. Third-generation CT scanner geometry (Hsieh, 2003).

### 2.4.3 X-ray Source in CT Scanner

CT scanners use bremsstrahlung X-rays as a source of radiation. This bremsstrahlung X-rays are produced by accelerating electron beams onto a target anode. The anode area from which X-rays are emitted is called the focal spot (Cunningham & Judy, 2003).

The intensity of X-ray beam is attenuated by absorption and scattering processes as it penetrates the object. The X-ray attenuation depends on the energy spectrum of the incident X-ray as well as on the average atomic number and mass density of the object. The transmitted intensity is given by

$$I_t = I_o e^{-\int \mu(s) ds} \quad (2.2)$$

where  $I_o$  and  $I_t$  are incident and transmitted beam intensities, respectively, and  $\mu(s)$  is the linear absorption coefficient at each point on the X-ray path. The fractional transmitted intensity,  $I_t/I_o$ , is measured for a large number of X-ray paths through the object. These values are then stored to obtain a set of line integrals for input to the reconstruction algorithms (ASTM, 2002a).

### 2.4.4 X-ray CT Scan Applications in Food Engineering

X-ray technology is not new to food process engineering. Schatzki, Witt, Wilkins, and Lenker (1981) demonstrated a technology for determining lettuce leaf density before its harvest. X-ray machines have also been used for detecting hollow

heart in potatoes (Finney & Norris, 1978), split-pit defect in peaches (Han, Bowers, & Dodd, 1992), and insect-infested pistachio nuts (Keagy, Parvin, & Schatzki, 1996). In a food processing plant, X-ray technology has successfully detected foreign materials (e.g., stones, bones, metal, and glass) in the food (Graves, Smith, & Batchelor, 1998). This conventional X-ray technology, known as direct transmission x-radiology, is useful for evaluating the overall internal quality of many food products.

X-ray CT scan imaging is an advanced method for nondestructively evaluating a cross section of an object. While a point on a conventional X-ray imaging represents the average volume of many volume elements between the X-ray source and the detector, each point on a CT image represents a small volume in the scanned slice. Tollner, Hung, Upchurch, and Prussia (1992) used CT scan images to quantify the physical properties (density and water content) of apples.

CT scan has been used to study the interior of agricultural and horticultural produce. Brecht, Shewfelt, Garner, and Tollner (1991) used CT scan to monitor maturity changes in tomato fruit. Barcelon, Tojo, and Watanabe (1999) studied the potential of CT scan to measure internal quality of peaches at different physiological maturity stages. CT scan was used to image interior region of Red Delicious apples under varying moisture content and density conditions (Toller et. al, 1992). The X-ray absorption of apples with watercore disorder was larger than apples without watercore disorder, due to increased water content of the injured tissue. CT scan also has been used to detect internal defects of other fresh produce (e.g., core breakdown in pears (Lammertyn, Jancsok, Dresselaers, Hecke, Wevers, Baerdemaeker et. al, 2001), woolly breakdown in

nectarines (Sonega, Ben-Arie, Raynal, & Pech, 1995), and section drying in tangerine (Peiris, Dull, Leffler, Burns, Thai, & Kays, 1998)). Shahin, Tollner, and Prussia (1999) designed a noise removal filter for CT scan imaging to improve accuracy of feature detection (watercore and bruise features in apples and diseases features in onions).

Most of CT scan applications in food processing have dealt with the nondestructive evaluation of the interior of an object. Little information is available in the literature regarding CT scan technique for food irradiation process. More recently, Borsa, Chu, Sun, Linton, and Hunter (2002) successfully used CT scan technique to obtain dose maps in irradiated foods such as frozen whole chickens, cured hams, and boxed frozen chicken breasts.

## **2.5 Graphic User Interface (GUI) for Food Processing and Food Irradiation**

Graphic User Interface (GUI) takes advantage of the computer's graphic capability to make a program easier to use. Nowadays, GUI tools are widely used in computer program because of their interactive demonstration capabilities. After the introduction and popularization of Hyper Text Markup Language (HTML) for the web and internet browsers, web pages have been used as one of the user interfaces. Using the Hyper Text Transfer Protocol (HTTP), the GUI can support not only the standalone platform but also internet network application. The rest of this section deals with GUI applications in food processing and irradiation area.

Interactive computer models have been developed for grain drying (Wang, Fon, & Fang, 2002) and heating process of microwavable foods (Jun & Puri, 2004). In both



models, MATLAB (Mathworks, Inc., Natick, Mass.) was used as a GUI development tool.

A rice quality inspection software with a graphical user interface was developed to facilitate machine operation, parameter preparation, and sorting precision adjustment (Wan, Lin, & Chiou, 2002). This software demonstrated performance comparable to subjective human inspection.

A three dimensional user interface was designed to a Monte Carlo program (GEANT4, Agostinelli et al., 2003) for process development and control in electron beam technology (Mittendorfer, Colon, & Gratzl, 2004). Its input window consisted of three parts: materials (elements and its compositions), detectors, and electron gun (energy and scan function). Virtual Reality Modeling Language (VRML) was used for the visualization of dose and particle trajectories.

A Java interface for a Monte Carlo code, called SimulRad, was developed to visualize water radiolysis (Plante, Filali-Mouhim, & Jay-Gerin, 2005). This interface enables a user to either visualize the spatial distribution of all reactive species presented in track of an ionizing particle or present an animation of the chemical development of the particle track. This interface developed for pure water could be extended to include the visualization of radiation effects on aqueous solutions containing solutes or biological molecules (such as DNA, proteins, etc).

More recently, a predictive microbiology program (Pathogen Model Program 7.0) was developed by the Agricultural Research Services (ARS) (USDA ARS, 2007).

This program was designed as a research tool for estimating the effects of multiple variables on the growth, inactivation, or survival of foodborne pathogens (Fig. 2.5).

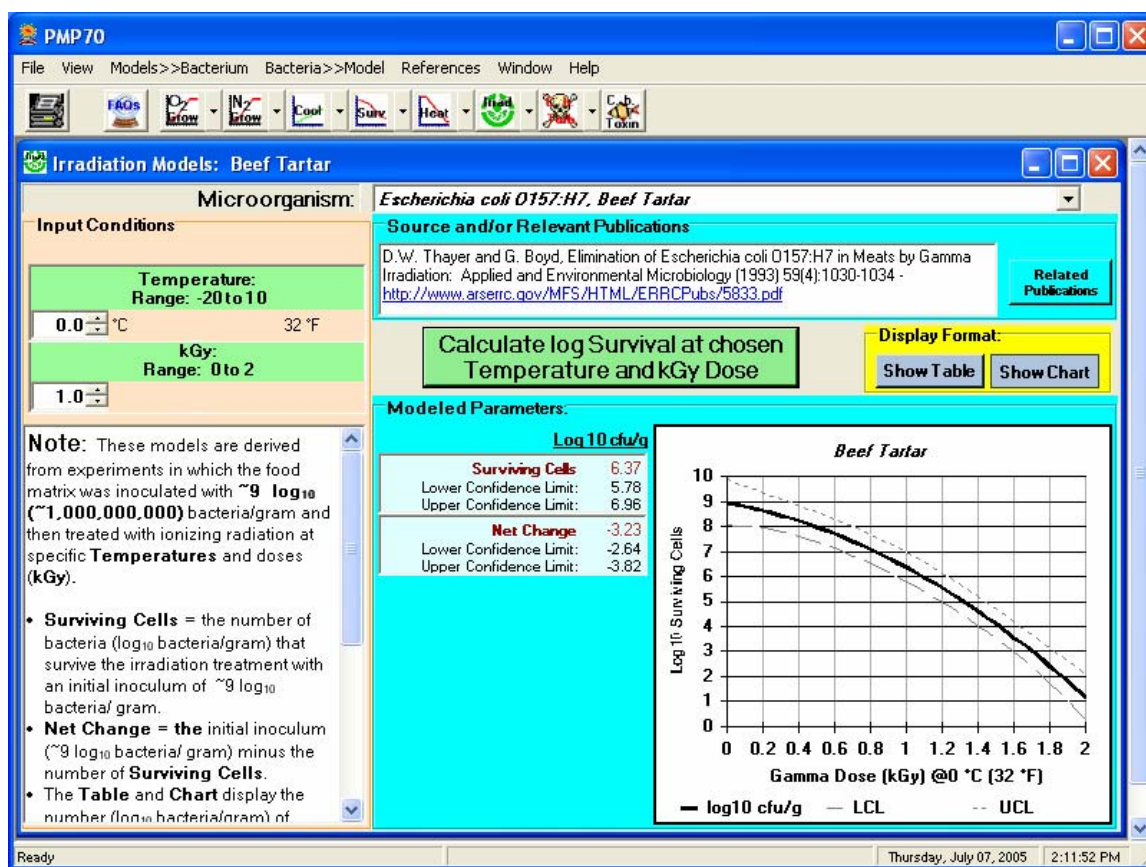


Fig. 2.5. *Escherichia coli* O157:H7 survival curve at beef tartar irradiated with gamma rays using Pathogen Modeling Program 7.0 (USDA ARS, 2007).

## CHAPTER III

### THEORY

#### 3.1 CT Scan Technique

##### 3.1.1 Principles of CT Scan

X-ray CT uses the rectilinear propagation and attenuation of X-rays that pass through an object. CT image represents the spatial variability of the attenuation coefficient  $\mu$  without superimposing structures. A two dimensional CT image is thus required to supply the values  $\mu(x, y)$  as a function of the spatial coordinates  $x$  and  $y$ .

The X-ray attenuation measurements are taken at several different angles and each attenuation measurement is digitized and stored in a computer to reconstruct CT image. Image reconstruction is carried out in two steps. The first step is the convolution step according to which all line integrals are convolved with a certain function. The second step is the backprojection step according to which the convolved line integrals are summed up for all projection angles between 0 and  $\pi$  (Oppelt, 2005).

There are two important factors on the quality of the reconstructed image: the number of projections and the spatial sampling interval of projections. Better quality images are constructed with a large number of projections. Higher resolution images can be obtained if the projections are acquired with a high spatial sampling rate.

Each pixel in the reconstructed image is assigned a number, referred to as a CT number (Hounsfield number). CT numbers are related to the linear attenuation coefficient ( $\mu$ ) of the scanned object, and can be calculated as follows (Hsieh, 2003):

$$CT\_number = \frac{\mu - \mu_{water}}{\mu_{water}} \times 1000 \quad (3.1)$$

CT numbers are established on a relative base, with the attenuation of water used as a reference. Thus, the CT number for water is always 0, and that for air is almost -1000.

The linear attenuation coefficient is the sum of the coefficients for several physical attenuations (Compton scattering, photoelectric effect, and pair production), each of which varies with the X-ray photon energy. It is thus essential that the CT system ensure the accuracy and reliability of those CT numbers. CT numbers are also used for analogous parameters such as electron density or mass density (ASTM, 2002a).

### 3.1.2 CT Data File

A CT data file consists of four columns: x and y coordinates of pixels, slice number, and CT number. Fig. 3.1 shows part of broccoli's CT data file.

Field of view (FOV) is the physical size of the area to be examined at CT scan, e.g., 12 cm × 12 cm, or 24 cm × 24 cm. The pixel resolution can be calculated by dividing the FOV by the matrix size of pixel, which is usually 512 × 512. For instance, since the field of view of broccoli is 12 cm, the pixel resolution is 0.23 mm (= 12 cm / 512). High resolution data can be obtained by decreasing the field of view. A Matlab script file, which can read raw CT data, extract CT number, and plot CT slice image, is presented in Appendix A.1.

212	305	13	50
212	305	14	-30
212	305	15	-949
212	305	16	-941
212	305	17	-950
212	306	0	-963
212	306	1	-956
212	306	2	-903
212	306	3	34
212	306	4	-106
212	306	5	-965

Fig. 3.1. Part of broccoli CT data file.

### 3.1.3 Two Dimensional CT Data Processing

The Matlab Image Processing Toolbox (MathWorks, Natick, Massachusetts) was used to make the image deck of the original and processed CT slices. The artifacts on the original CT slices, such as tape for holding sample, was removed and cropped to fit the region of interest (ROI). Inside the ROI, the target product was then segmented out from the background.

In Matlab, loading the CT data constitutes two variables to the workspace:  $X$  ( $r \times c \times n$ , class unit 8) and a grayscale colormap,  $\text{map}$  ( $N \times 3$ , class unit 8). The variable  $r$  and  $c$  are the number of rows and columns of each slice, respectively, and  $n$  is the number of slices.  $N$  is the index scales of each slice. Since grayscale colormap is an intensity image of class unit 8, which is 8 bit integers in the range  $[0, 255]$ ,  $N$  is usually is 256. For example, a Roman tomato scanned by the CT scanner produced 10 slices ( $512 \times 512$ ) with a  $256 \times 3$  colormap. With Matlab, these slices can be loaded into a four

dimensional ( $512 \times 512 \times 1 \times 10$ ) array  $X$ , where the third dimension represents the index channel which works together with `colormap` to generate color images.

The image decks were generated using the Matlab command `montage(X,map)` to show all raw CT images in one sheet. Fig. 3.2 shows the original image deck of CT slices of a Roman tomato.

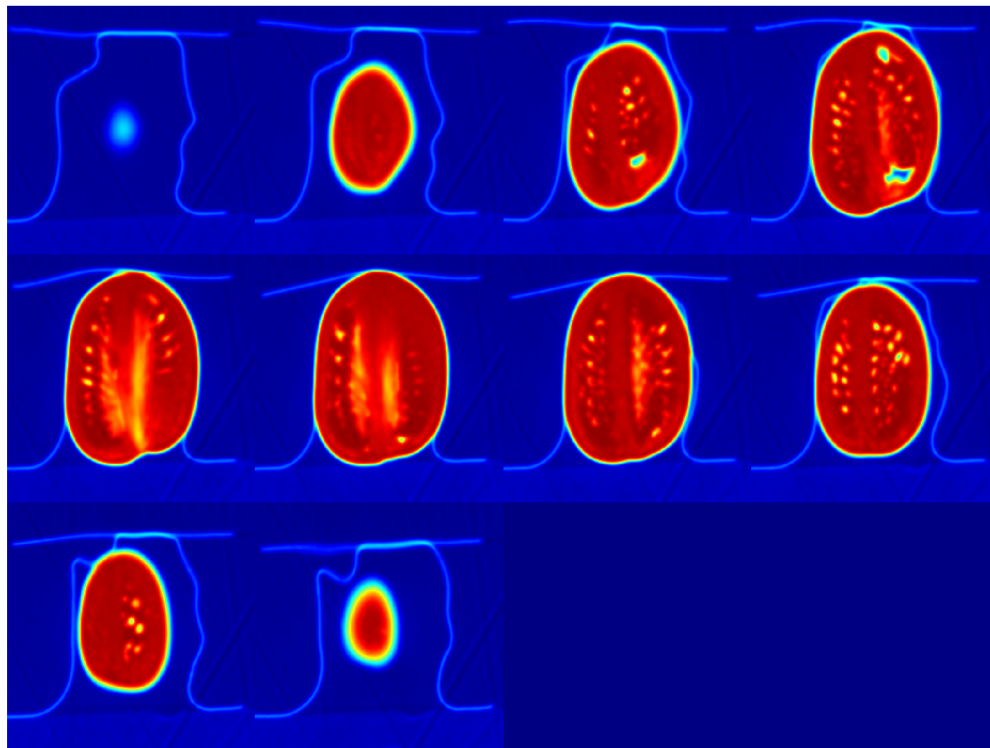


Fig. 3.2. Original CT slice deck of a Roman tomato.

Artifacts on the images must to be removed to obtain a clean image.

Thresholding is one of the most important and fundamental approaches to image segmentation. When the intensity histogram shows some distinct groups depending on objects, one way to extract the objects from the background is to select a threshold  $T$  that separates these groups. In the Roman tomato CT image, the major artifact is the tapes, used for holding the sample on the CT moving bed (Fig. 3.3).

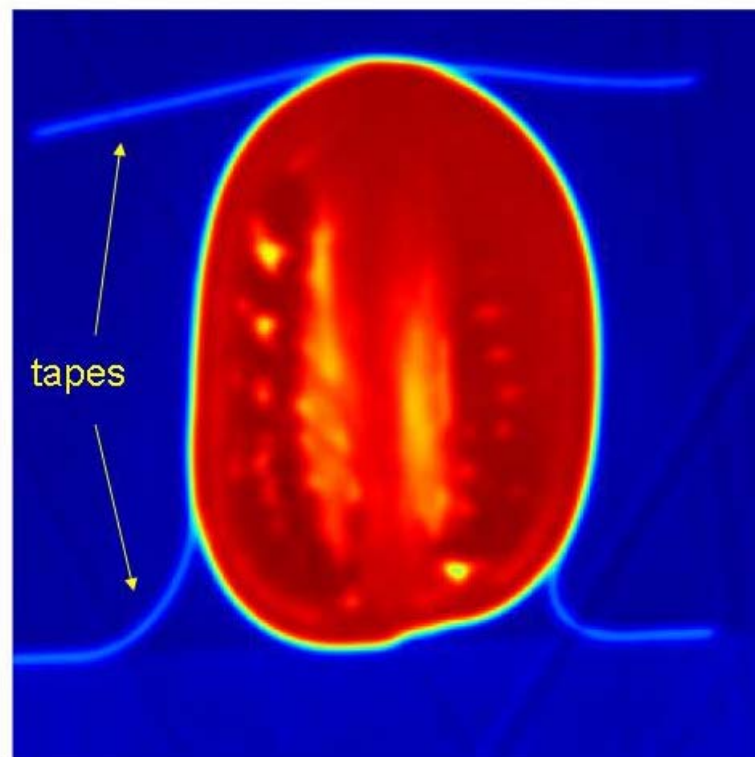


Fig. 3.3. A CT image of a Roman tomato, showing artifact (tapes).

The artifact can be removed with masked filtering with Matlab. We can easily remove tapes because of their relatively low index values, which are related to CT numbers. The mask image can be generated by the Matlab command  $mask = (X(:,:,1,k) < Z)$  where  $k = 1$  and  $Z = 80$  for example. Then, the tapes can be removed from all of the slices with Matlab as

```

if mask(i,j) == 0
    X(i,j,1,k) = 0;
End

```

After removal of the artifacts, image cropping is required to eliminate the background of CT images. A region of interest (ROI) is then defined so that the images are focused on the target. This operation will reduce the size of the image slices and make further manipulation easier. The operation of cropping can be done on the slices by the Matlab command  $imcrop(X(:,:,l,k),[x,y,dx,dy])$  where  $(x,y)$  is the cropped image origin at the upper-left corner and  $dx$  and  $dy$  are the width and height of the cropped images, respectively.

Fig. 3.4 shows the ROI of the CT image of a Roman tomato after artifact removal and image cropping have been performed. Fig. 3.5 shows the processed image deck of all CT slices of a Roman tomato. With Matlab, the artifact removal and image cropping can be implemented simultaneously and automatically.



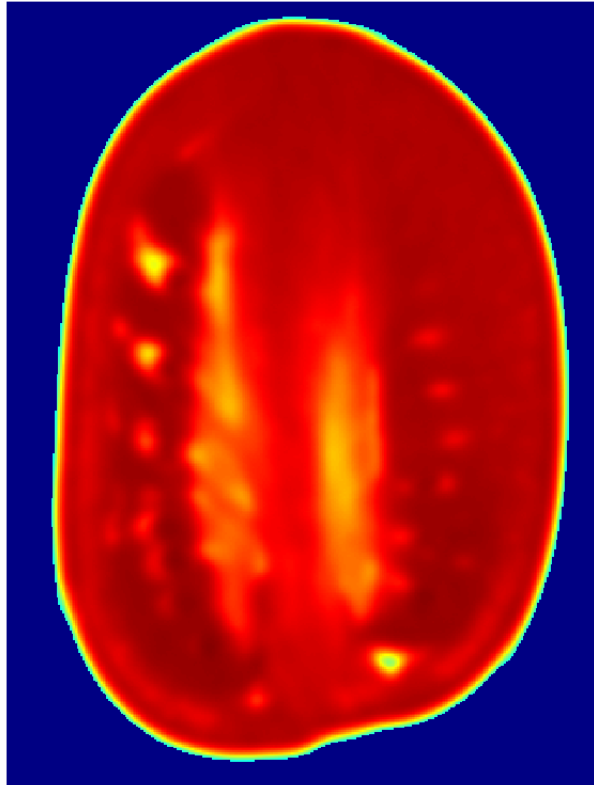


Fig. 3.4. A processed CT image of a Roman tomato.

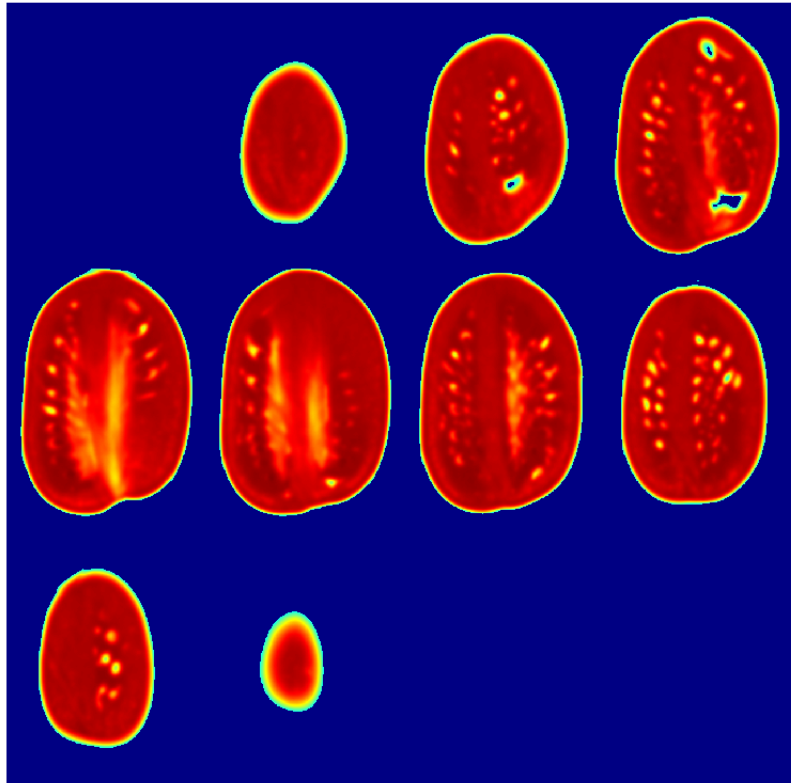


Fig. 3.5. All processed CT slices of a Roman tomato.

### 3.1.4 Three Dimensional Reconstruction and Visualization

Nowadays, the advanced imaging techniques such as CT produce enough data to display volumetric visualization. Because a CT slice has the dimensions of depth (slice thickness), the pixel is transformed into a voxel.

Surface rendering (isosurface) techniques do not process the whole volume data for visualization purposes. The marching-cubes algorithm (Lorenson & Cline, 1987) is used to extract isosurfaces. In this algorithm, the data volume is divided into a grid of cells, each cell consisting of 8 neighboring voxels. In each grid cell that contains voxel values both above and below the threshold, polygons are generated and connect the interpolated points on the edges with the threshold value.

Volume rendering is done in two steps. In a first step, polygons are defined for each of the original CT slices and placed within the 3D scene. In the second step, on each of the polygons the image content of the corresponding CT slices is filled in. Thus, each image is mapped onto the correct polygon. Finally, all the polygons have to be combined by the application of a compositing step (Oppelt, 2005).

These two schemes have been adopted at the Matlab image processing toolbox. We can not only display the overall structure of a volume (Fig. 3.6), but also show the cutaway surface (Fig. 3.7) using Matlab. Appendix A.2 is the Matlab file for 3D visualization.

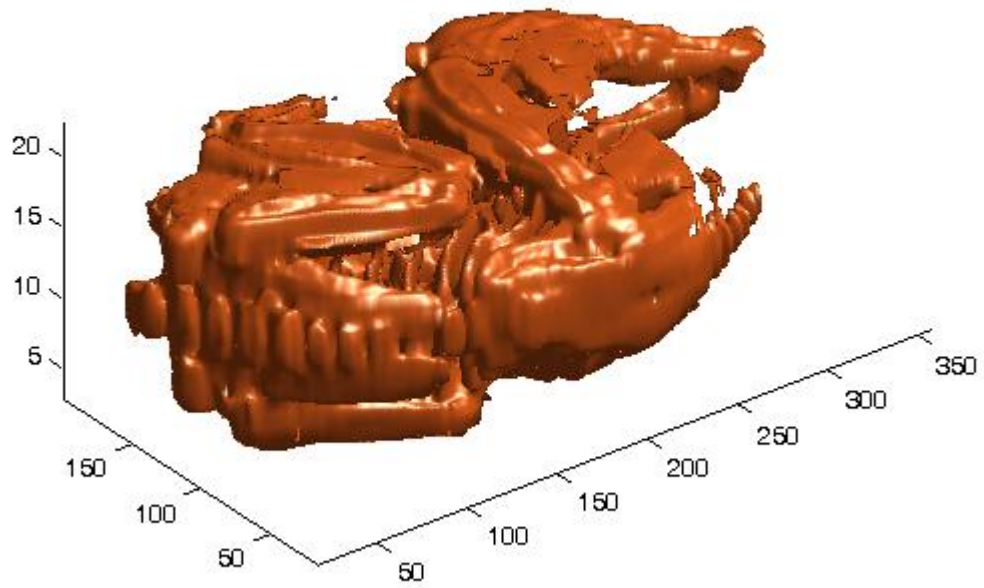


Fig. 3.6. Isosurfaces of a chicken carcass from CT data.

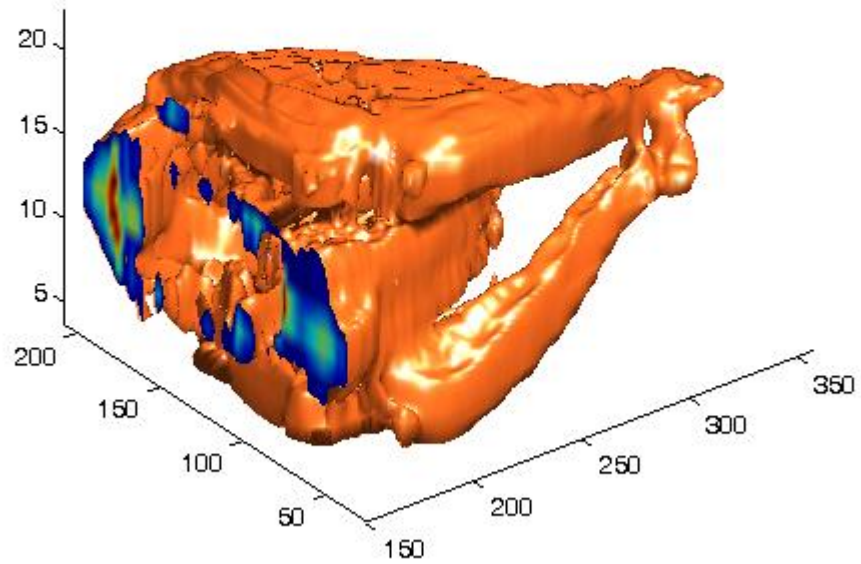


Fig. 3.7. Cutaway of a chicken carcass from CT data.

## **3.2 Monte Carlo Simulation**

### **3.2.1 Electron Transport in MCNP**

The result of a Monte Carlo radiation transport is a simulated track consisting of the geometrical positions of all energy deposition events as well as the amount of energy deposited at each interaction point. Since the transport of electrons is dominated by the long range of Coulomb force, the electron Monte Carlo histories are significantly longer than neutron and photon histories.

At electron Monte Carlo transport, each electron track starts off at a given position, with initial direction and energy. The state of a particle after interaction is defined by its position coordinates, energy, and direction cosines of the direction of flight. An electron path is broken into many steps to follow an electron through a significant energy loss. These steps are chosen not only to be long enough to include many collisions so that multiple-scattering theories are valid (“major steps”), but also to be short enough that mean energy loss in any step is small (“sub-steps”). The energy loss (Berger, 1963) and angular deflection (Goudsmit & Saunderson, 1940) of the electron during each of steps can then be sampled from probability distributions on the appropriate multiple scattering theories. It is impractical to model all many individual interactions. Instead, well-established statistical theories (“condensed history”) are used to describe those interactions into single steps. The electron tracks are finished either when they leave the material system or when the energy becomes smaller than an energy cutoff, which is the energy where particles are assumed to be effectively stopped and absorbed in the medium.

In this section outlines of electron transport used in MCNP Monte Carlo simulations are described in some detail, including the scoring scheme.

### 3.2.1.1 Electron Transport Mechanics

#### 3.2.1.1.1 Electron Steps of the Random Walk

In condensed random walk, the electron trajectories can be described by a series of states  $s_n$ ,  $E_n$ ,  $t_n$ ,  $\vec{u}_n$ , and  $\vec{v}_n$ , which are the total path length, energy, time, direction, and position of electrons at the end of  $n$  steps. A condensed history is sampled by letting the particle carry out a random walk in which each step, from state  $n$  to state  $n+1$ , takes into account the combined effect of many collisions.

The path length is chosen by the constant factor  $k (=E_{n+1}/E_n)$ , which is the energy loss per step. Given  $E_n$  and  $s_n$ , the  $s_{n+1}$  is then determined by

$$1 + \frac{1}{E_n} \int_{s_n}^{s_{n+1}} \frac{dE}{ds} ds = k, \quad (3.2)$$

where  $dE/ds$  is the mean rate of energy loss per unit path length resulting from ionization. In MCNP, the commonly used value of  $k$  is  $2^{-1/8}$ , which results in the electron lost 8.3% of its energy during each step (Brown, 2003).

The size of the steps of the random walk ( $\Delta s_n = s_{n+1} - s_n$ ) determined by equation (3.2) is called major step. The condensed random walk for electrons is carried out in terms of these major steps. The energy straggling and the angular scattering are

applied per major step with satisfactory accuracy. However, the electron trajectory with many small steps will be more accurate if the angular deflections are required to be small or electrons across a boundary of interest. Therefore, MCNP breaks the major steps into smaller substeps. At these substeps, angular deflections and the production of secondary particles are sampled. A major step of path length  $s$  is divided into  $m$  substeps, where  $m$  depends on material atomic number  $Z$ . At a very small material region, where pre-determined substeps for an accurate simulation of the electron trajectory are not enough, it would be desirable to increase the value of  $m$  (Brown, 2003).

#### **3.2.1.1.2 Simulation of Electron Radiation Transport**

At the initiation step of an electron transport calculation, all necessary data are pre-calculated or read from the electron data file. These data include the electron energy grid, stopping powers, electron ranges, energy step lengths, substep lengths, and probability distribution for angular deflections and for the production of secondary particles (Brown, 2003).

The collision energy loss rate is sampled at the beginning of each major step. Since fluctuations in every loss rate occurs due to the cumulative effect of many individual random collisions,  $m$  substeps are required and taken in the current major step. The detailed simulation of electron history, except for the energy loss and straggling calculation, takes place in the sampling of substeps. At the end of each substep, the direction of electron is determined with the Goudsmit-Saunderson theory for angular deflection, and the projected energy is calculated with the current energy loss



rate and the substep length. Finally, secondary particles are generated using the appropriate probability distributions. They include knock-on electrons and bremsstrahlung photons, and move separately with their own energy.

This process continues until they meet the terminal conditions, including escape (entering a region of zero importance), loss to time cutoff, loss to a variety of variance reduction process, and loss to energy cutoff. Fig. 3.8 is a schematic flow chart showing electron transport algorithms.

### 3.2.1.2 Energy Loss

#### 3.2.1.2.1 Scattering by Electron (Knock-on Electron)

The Møller cross section (Møller, 1932) for scattering of electrons by electrons is

$$\frac{d\sigma}{d\varepsilon} = \frac{C}{E} \left\{ \frac{1}{\varepsilon^2} + \frac{1}{(1-\varepsilon)^2} + \left( \frac{\tau}{\tau+1} \right)^2 - \frac{2\tau+1}{(\tau+1)^2} \frac{1}{\varepsilon(1-\varepsilon)} \right\} \quad (3.3)$$

Here  $\varepsilon$  represents the energy transfer as fractions of electron kinetic energy  $E$ ;  $\tau$  is the electron kinetic energy in units of the electron rest mass; and the coefficient of  $C$  is given by

$$C = \frac{2\pi e^4}{mv^2}, \quad (3.4)$$

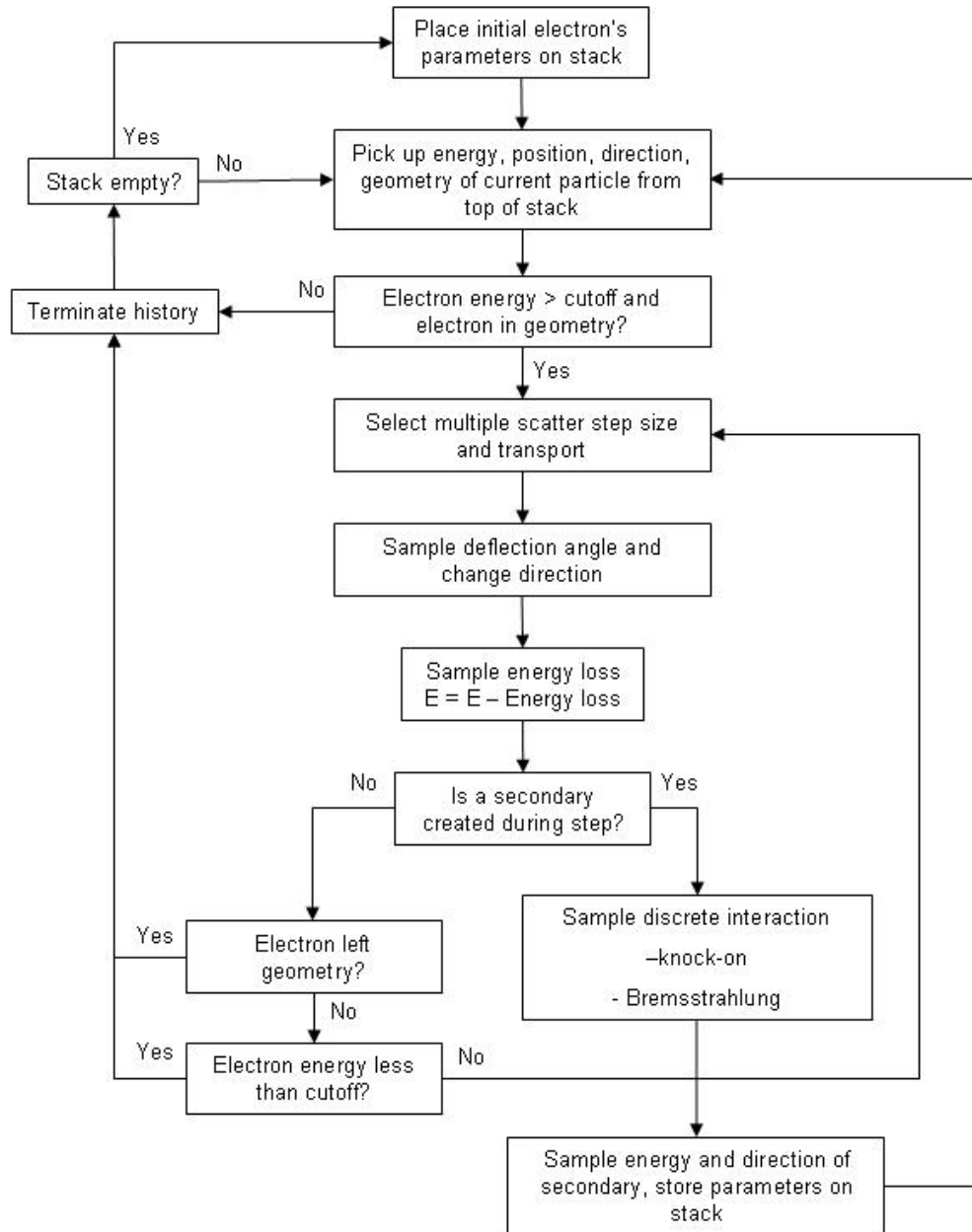


Fig. 3.8. Flow diagram of electron transport (Bielajew, 2001).

where  $m$ ,  $e$ , and  $v$  are the rest mass, charge, and speed of electron, respectively.

For the sampling of transportable secondary particles, the probability of electron transfer is greater than  $\varepsilon_c$  representing the energy cutoff of secondary particles, and less than  $\frac{1}{2}$ , because the outgoing electron of higher energy is the primary electron. Explicit integration of Equation 3.3 from  $\varepsilon_c$  to  $\frac{1}{2}$  leads to

$$\sigma(\varepsilon_c) = \frac{C}{E} \left\{ \frac{1}{\varepsilon_c} - \frac{1}{1-\varepsilon_c} + \left( \frac{\tau}{\tau+1} \right)^2 \left( \frac{1}{2} - \varepsilon_c \right) - \frac{2\tau+1}{(\tau+1)^2} \ln \frac{1-\varepsilon_c}{\varepsilon_c} \right\} \quad (3.5)$$

Then the normalized probability distribution for generation of secondary electrons is given by (Brown, 2003)

$$g(\varepsilon, \varepsilon_c) d\varepsilon = \frac{1}{\sigma(\varepsilon_c)} \frac{d\sigma}{d\varepsilon} d\varepsilon \quad (3.6)$$

At each electron sub step, MCNP uses  $\sigma(\varepsilon_c)$  to determine whether knock-on electrons will be generated. Once it has been generated, the angle between the primary electron and the direction of secondary particle is determined by momentum conservation. However, neither the energy nor the direction of the primary electron is changed by the sampling of the secondary particle, because both have been taken into account by the multiple scattering theories.

### 3.2.1.2.2 Stopping Power for Electron

#### 3.2.1.2.2.1 Collision Stopping Power

The mean energy loss by ionization per unit path length (“stopping power”) resulting from collision with energy transfers  $\varepsilon < \varepsilon_c$  is calculated as (Berger, 1963),

$$-\left(\frac{dE}{ds}\right)_{\varepsilon_c} = NZ \int_0^{\varepsilon_c} \varepsilon \frac{d\sigma}{d\varepsilon} d\varepsilon \quad (3.7)$$

where  $N$  is number of atoms per  $\text{cm}^3$ , and  $Z$  is atomic number. Applying the Møller cross section and the Bethe theory (Bethe & Heitler, 1934) of stopping power to equation (3.7), Berger (1963) gives the restricted electron collision stopping power in the form

$$-\left(\frac{dE}{ds}\right)_{\varepsilon_c} = NZC \left\{ \ln \frac{E^2(\tau + 2)}{2I^2} + f^-(\tau, \varepsilon_c) - \delta \right\} \quad (3.8)$$

where

$$f^-(\tau, \varepsilon_c) = -1 - \beta^2 + \left(\frac{\tau}{\tau + 1}\right)^2 \frac{\varepsilon_c^2}{2} + \frac{2\tau + 1}{(\tau + 1)^2} \ln(1 - \varepsilon_c) + \ln[4\varepsilon_c(1 - \varepsilon_c)] + \frac{1}{1 - \varepsilon_c} \quad (3.9)$$

$I$  is the mean ionization potential in the same units as  $E$ , and  $\delta$ , the density effect correction factor, represents the reduction of the mean energy loss caused by the polarization of the medium.

In order to calculate the total energy loss to collision,  $\varepsilon_c$  is set as  $1/2$ .

With  $\varepsilon_c = 1/2$ , equation (3.9) becomes

$$f^-(\tau, \varepsilon_c) = -\beta^2 + (1 - \ln 2) + \left(\frac{1}{8} + \ln 2\right) \left(\frac{\tau}{\tau + 1}\right)^2 \quad (3.10)$$

Next supplementary constant  $C_2$ ,  $C_3$ , and  $C_4$  are introduced so that the resulting form for collision stopping power used by MCNP is

$$-\left(\frac{dE}{ds}\right) = \frac{10^{24} \alpha^2 h^2 Z}{2\pi m \beta^2} \left\{ \ln[\tau^2(\tau + 2)] - C_2 + C_3 - \beta^2 + C_4 \left(\frac{\tau}{\tau + 1}\right)^2 - \delta \right\} \quad (3.11)$$

where  $\alpha = \frac{2\pi e^2}{hc}$  and  $h$  is Plank's constant. Other constants are:  $C_2 = \ln(2I^2)$ ,  $C_3 = 1 -$

$\ln 2$ ,  $C_4 = 1/8 + \ln 2$  (Brown, 2003).

The mean ionization potential ( $I$ ) and density effect correction ( $\delta$ ) depend on the state of the material, either gas or solid. The physical state of the material (compositions and densities) also modifies the density effect calculation (Sternheimer & Peierls, 1971).

### 3.2.1.2.2 Radiative Stopping Power

The radiative stopping power due to bremsstrahlung emission is written as

$$-\frac{1}{\rho} \left( \frac{dE}{ds} \right)_{rad} = \frac{N}{A} \alpha r_e^2 Z^2 (T_1 + mc^2) \Phi_{rad} \quad (3.12)$$

where  $\rho$  is mass density,  $A$  is the atomic weight of the medium,  $r_e$  is the classical electron radius,  $T_1$  is the incident electron kinetic energy,  $mc^2$  is the electron rest mass, and  $\Phi_{rad}$  is the dimensionless, scaled, integrated bremsstrahlung energy loss cross section.  $\Phi_{rad}$  can be written as the sum of the electron-nucleus and the electron-electron components:

$$\Phi_{rad} = \Phi_{rad}^{(n)} + Z\Phi_{rad}^{(e)} \quad (3.13)$$

or

$$\Phi_{rad} = \left( 1 + \frac{\bar{\eta}}{Z} \right) \Phi_{rad}^{(n)} \quad (3.14)$$

where  $\bar{\eta}$  is a parameter to account for the contribution of the electron-electron bremsstrahlung to the integrated radiative energy loss cross section.

$$\bar{\eta} = \frac{\Phi_{rad}^{(e)}}{\left(\frac{1}{Z^2} \Phi_{rad}^{(n)}\right)} \quad (3.15)$$

With equation (3.14), equation (3.12) for the radiative stopping power can be rewritten as

$$-\frac{1}{\rho} \left( \frac{dE}{ds} \right)_{rad} = \frac{N}{A} \alpha r_e^2 Z(Z + \bar{\eta})(T_1 + mc^2) \Phi_{rad}^{(n)} \quad (3.16)$$

which is used in MCNP. Numerical values of  $\Phi_{rad}^{(n)}$  are taken from Seltzer and Berger (1985) and Seltzer (1988a). The dimensions of the radiative stopping power are the same as the collisional stopping power.

### 3.2.1.2.3 Energy Straggling

The energy loss  $\Delta$  due to multiple ionization and excitation collision in a path length  $s$  is described by the Landau distribution (Landau, 1944). Let  $f(s, \Delta)d\Delta$  be the probability distribution of an energy loss between  $\Delta + d\Delta$  in a path length  $s$ . In Landau theory, it can be expressed in terms of a universal function of a single scaled variable,

$$f(s, \Delta)d\Delta = \phi(\lambda)d\lambda, \quad (3.17)$$

where

$$\lambda = \frac{\Delta}{\xi} - \ln \left[ \frac{2\xi m v^2}{(1-\beta^2)I^2} \right] + \beta^2 + \delta - 0.42278. \quad (3.18)$$

The parameter  $\xi$  is given by

$$\xi = \frac{0.154}{\beta^2} \frac{Z}{A} s \quad (3.19)$$

and can be interpreted as the single-scattering energy loss that is exceeded, on the average, only once in a path length  $s$ . The universal function  $\phi(\lambda)$  is defined by

$$\phi(\lambda) = \frac{1}{2\pi i} \int_{x-i\infty}^{x+i\infty} \exp[u \ln(u) + \lambda u] du \quad (3.20)$$

where  $x$  is a positive real number specifying the line of integration. This function  $\phi(\lambda)$  was tabulated by Börsch-Supan (1961) for values of  $\lambda$  between -4 and 100. For  $\lambda < -4$ ,  $\phi(\lambda)$  is negligible, so that this range is ignored. For  $\lambda > 100$ , the asymptotic formula was given by Börsch-Supan (1961):

$$\phi(\lambda) \approx \frac{1}{w^2 + \pi^2} \quad (3.21)$$

where  $w$  is the auxiliary variable, and  $\lambda = w + \ln w - 0.92278$ .



The asymptotic form for  $\phi(\lambda)$  shows that arbitrarily large energy losses are allowed in single inelastic collisions, so  $\phi(\lambda)$  does not have a finite mean energy loss. Therefore, material and energy dependent cutoff  $\lambda_{\text{cut}}$  is imposed on the sampling of  $\lambda$ . For each material and electron energy, the MCNP code uses the known mean collisional energy loss  $\bar{\Delta}$ , interpolating in this tabular function to select a suitable value of  $\lambda_{\text{cut}}$ , which is then stored in the dynamically-allocated array. During the electron transport calculation, any sample value of  $\lambda$  greater than the limit ( $\lambda_{\text{cut}}$ ) is rejected. In this way, the correct mean energy loss is preserved.

### 3.2.1.3 Change of Direction

The MCNP code relies on the Goudsmit-Saunderson multiple-scattering theory for the net angular deflection from the combined effect of the elastic and inelastic collisions in a single substep. Goudsmit-Saunderson theory is exact for any angle because it was derived in a small angle approximation, and it can be evaluated with any desired single scattering cross section.

According to the Goudsmit-Saunderson distribution, the angular deflection of the electron is

$$F_{GS}(\theta, s) = \sum_{l=0}^{\infty} \frac{2l+1}{2} \exp(-sG_l) P_l(\cos \theta) \quad (3.22)$$

where

$$G_l = 2\pi N \int_{-1}^{+1} \frac{d\sigma(\theta, T)}{d\Omega} [1 - P_l(\cos\theta)] d(\cos\theta) \quad (3.23)$$

In equation (3.22),  $s$  is the length of sub step,  $\cos\theta$  is the angular deflection from the direction at the beginning of the sub step, and  $G_l$  is the  $l^{\text{th}}$  Legendre polynomial.

$d\sigma(\theta, T)/d\Omega$  is the single scattering cross section for an electron with kinetic energy  $T$ , and  $N$  is the number of atoms per unit volume.

For low energy electrons, Berger and Wang (1988) generated a set of elastic scattering cross sections from 1 to 1024 keV, for all elements (atomic numbers  $Z=1$  to 100). For high energy electrons, the single scattering cross section is approximated as a combination of the Mott (1929) and Rutherford (1911) cross sections. The former is exact for the unscreened point nucleus, and includes spin and relativistic effects, and the latter was modified with the screen correction term from the work of Molière (1947). Using this approximation, Seltzer (1988b) presents the cross section as

$$\frac{d\sigma(\theta, T)}{d\Omega} = \frac{Z^2 e^2}{p^2 v^2 (1 - \cos\theta + 2\eta)^2} \left[ \frac{(d\sigma_{Mott} / d\Omega)}{(d\sigma_{Rutherford} / d\Omega)} \right] \quad (3.24)$$

where  $Ze$  is the nuclear charge,  $p$  is the momentum, and  $v$  is the velocity of the incident electron. Currently, MCNP uses the screening correction  $\eta$  developed by Seltzer (1988b) as below,

$$\eta = \frac{1}{4} \left( \frac{\alpha mc}{0.885 p} \right)^2 Z^{2/3} \left[ 1.13 + 3.76 (\alpha Z / \beta)^2 \left( \frac{\tau}{\tau + 1} \right)^{1/2} \right] \quad (3.25)$$

where  $\tau$  is the kinetic energy of the electron in units of its rest energy.

### 3.2.1.4 Bremsstrahlung

For the sampling of bremsstrahlung photons, MCNP relies on Bethe-Heitler (1934), Born-approximation results that have been used in ETRAN (Seltzer, 1991). The production cross section for bremsstrahlung photons and spectra are evaluated by Seltzer (1988a) and Seltzer and Berger (1985). At electron-nucleus bremsstrahlung cross section, the evaluation below 2 MeV uses results of Pratt, Tseng, Lee, Kissel, MacCallum, and Riely (1977) based on numerical phase-shift calculations. For 50 MeV and above, the analytical electron-nucleus bremsstrahlung theory of Davies, Bethe, Maximon, and Olsen (DBMO) (Davies, Bethe, & Maximon, 1954; Olsen, 1955) is used to evaluate the bremsstrahlung cross sections. Their cross section is written in terms of the Bethe-Heitler, Born approximation formula, screening effects, and a Coulomb correction term. The interpolation across the gap region  $2 \text{ MeV} < T_l < 50 \text{ MeV}$  is carried out by fitting a cubic splines to the cross sections at lower and higher energies. The electron-electron bremsstrahlung theory of Haug (1975), combined with screening corrections derived from Hartree-Fock incoherent scattering factors, is also included in the cross section evaluation.

MCNP checks production of bremsstrahlung photons at each electron substep. The tables of production probabilities are used to determine whether a bremsstrahlung photon will be generated. This bremsstrahlung production is sampled from a Poisson distribution, and the photon energy is subtracted from the electron energy. However, the direction of the electron is unaffected by the generation of the photon, because the angular deflection of the electron is controlled by the multiple scattering theory.

If the sampled photon energy is greater than a pre-determined cutoff value, the photon history is traced. The starting position for the photon is chosen at random along the substep. The photon emission angle (relative to the direction of the primary electron) is sampled from an angular distribution derived from a combination of Bethe-Heitler cross sections (Koch & Motz, 1959).

#### **3.2.1.5 Pulse Height Tally**

MCNP provides four standard electron tallies: surface current, surface flux, track length estimate of a cell flux, and pulse height tally (Brown, 2003). All those tallies are normalized to be per starting particle.

The pulse height tally provides the energy deposition in a cell. This tally is analogous to a physical detector, and the tally bins correspond to the total energy deposited in a detector. Unlike other tallies, which estimate macroscopic variables, such as flux, whose values are determined by large number of microscopic events, the pulse height tally records the energy deposited in a cell by each source particles and its

secondary particles. For the pulse height tally, microscopic events are modeled more realistically (Brown, 2003).

Scoring the pulse height tally is done at the end of each history. When a particle crosses surface, the energy is added to the account of the cell that it is entering, and is subtracted to the account of the cell that it is leaving. At the end of all history, the account of each cell is divided by the total number of source. The absorbed dose in each cell is determined by the ratio of its energy deposition to its mass.

### 3.2.2. Dose Calculation Procedure

After the Monte Carlo process is finished, doses are calculated by dividing the total energy deposited in each voxel by its material mass. Conversion to units of kiloGray (kGy) can be achieved using the conversion factor, the beam current ( $I$ ), and the area irradiated ( $A$ ) (ASTM, 2002b). The conversion factor is derived from the following equivalents:

$$1 \text{ kGy} = 6.24 \times 10^{12} \text{ MeV/g}, \quad (3.26)$$

$$1 \text{ mA} = 6.24 \times 10^{15} \text{ electrons/s}, \quad (3.27)$$

and  $1 \text{ MeV} \cdot \text{cm}^2/(\text{g} \cdot \text{electron})$

$$\begin{aligned} &= [1.6 \times 10^{-13} \text{ kGy} \cdot \text{cm}^2/\text{electron}][1 \text{ electron}/(1.6 \times 10^{-16} \text{ mA} \cdot \text{s})] \\ &= 1000 \text{ kGy} \cdot \text{cm}^2/(\text{mA} \cdot \text{s}) \end{aligned} \quad (3.28)$$

Thus, the absorbed dose ( $D$ ) for electron beam is

$$D = 1000 \frac{EI}{mA} \quad (3.29)$$

where  $D$  is the absorbed dose (kGy),  $E$  is the energy absorbed (MeV),  $I$  is the beam current (mA),  $m$  is the mass (g), and  $A$  is the irradiated area ( $\text{cm}^2$ ).

For instance, in a 10 MeV linac, an electron beam current is 1.4 mA. Considering its beam configuration and conveyor system (Fig. 3.9), the area irradiated ( $A$ ) is equal to the product of the scan width ( $W$ ) and the conveyor speed ( $V$ ). Assuming that the scan width is 60.96 cm (2 ft) and the conveyor speed is 30.3 cm/sec (60 ft/min), the area irradiated is  $1858 \text{ cm}^2/\text{sec}$ . Since current is quantity of charge per second, the current density ( $I/A$ ) is, in this case,  $7.53 \times 10^{-4} \text{ mA}/\text{cm}^2$ . Thus, the absorbed dose at the voxel is 0.15 kGy.

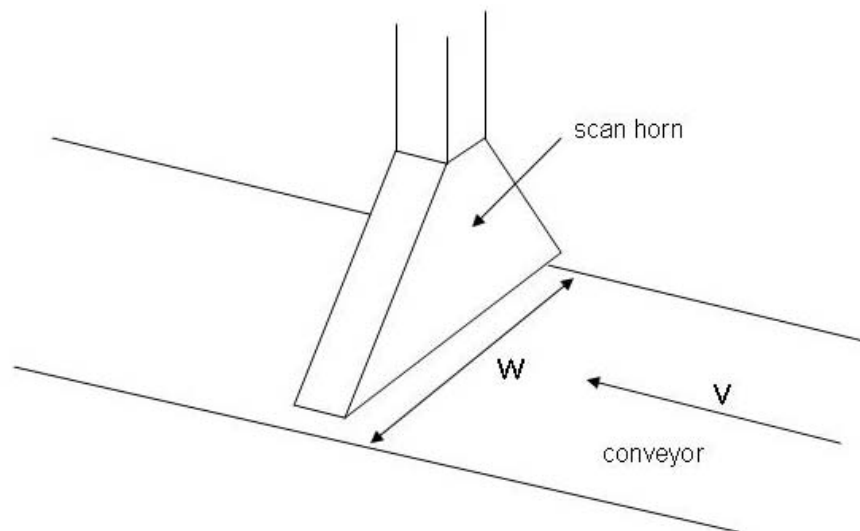


Fig. 3.9. Beam scanning configuration at 10 MeV linac.

### **3.2.3 MCNP Geometry**

#### **3.2.3.1 Lattice Structure**

Lattice structure feature is used to integrate CT data into the MCNP geometry scheme. The user defines one big bounding cell, with which one small lattice element (hexahedral or hexagonal) is filled, and the center of the bounding cell. The MCNP automatically fills the bounding cell with lattice element starting from the center.

The dimension of lattice element is determined by resolution of CT data and the slice thickness. For example, if the field of view and the slice thickness of CT are 12 and 0.5 cm, respectively, the dimension of the hexagonal lattice element is  $0.23 \times 0.23 \times 5$  mm. In addition, each lattice element can have its own material density, which enables to use element's various density data. Recently, a number of groups in radiation therapy have developed their own methods for converting CT scan data into MCNP geometry using lattice structure (Borisov, Franck, de Carlan, & Laval, 2002; Evans, Blue, & Gupta, 2001; Van Riper, 2005).

#### **3.2.3.2 Coordinate Transformation**

Coordinate transformation in MCNP is used to simplify the complicate geometrical description, such as a skewed cylinder and cluster of cells. This technique is required to determine food position and irradiation strategies for uniform dose distribution at electron beam treatment. Coordinate transform card consists of displacement vector and rotation matrix of the transformation.

A  $3 \times 3$  rotation matrix can be defined as a transformation matrix which operates on a position vector in a three dimensional Euclidean space, whose coordinates expressed in a rotated coordinate system  $OUVW$  (body-attached frame) to a reference coordinate system  $OXYZ$  (Fig. 3.10). The  $OXYZ$  coordinate system is fixed in the three dimensional space and is considered to be the reference frame. The  $OUVW$  coordinate frame is rotating with respect to the reference frame  $OXYZ$ .

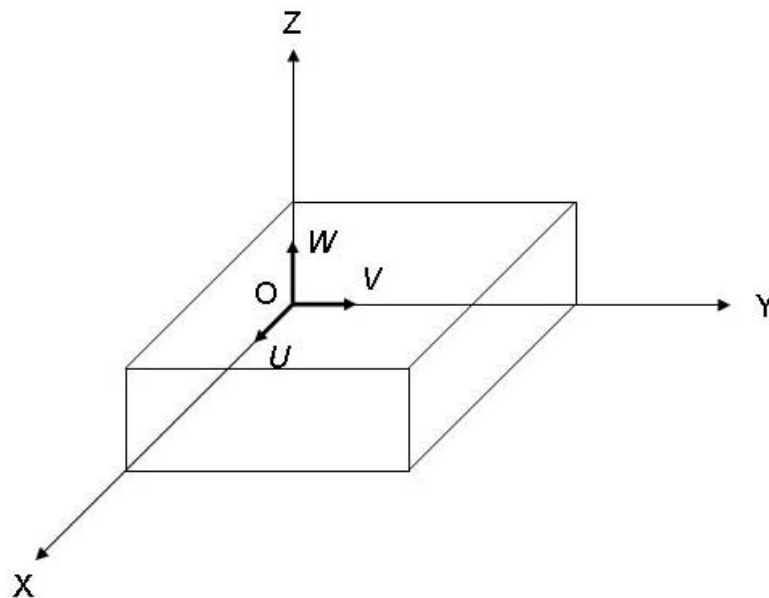


Fig. 3.10. Reference and body-attached coordinate system (Fu, Gonzales, & Lee, 1987).



The transformation matrix  $R_{x,\alpha}$ , rotating about  $OX$  axis with  $\alpha$  angle, is derived as,

$$R_{x,\alpha} = \begin{bmatrix} 1 & 0 & 0 \\ 0 & \cos \alpha & -\sin \alpha \\ 0 & \sin \alpha & \cos \alpha \end{bmatrix} \quad (3.30)$$

Similarly, the  $3 \times 3$  rotation matrices for rotation about the  $OY$  axis with  $\varphi$  angle and about the  $OZ$  axis with  $\theta$  angle area, respectively, are

$$R_{y,\varphi} = \begin{bmatrix} \cos \varphi & 0 & \sin \varphi \\ 0 & 1 & 0 \\ -\sin \varphi & 0 & \cos \varphi \end{bmatrix} \text{ and } R_{z,\theta} = \begin{bmatrix} \cos \theta & -\sin \theta & 0 \\ \sin \theta & \cos \theta & 0 \\ 0 & 0 & 1 \end{bmatrix} \quad (3.31)$$

Basic rotation matrices can be multiplied together to represent a sequence finite rotation about the principal axes of the  $OXYZ$  coordinate system. For example, a rotation matrix, representing a rotation of  $\varphi$  angle about  $OY$  axis followed by a rotation of  $\theta$  angle about  $OW$  axis followed by a rotation of  $\alpha$  angle about  $OU$  axis, is as bellow:

$$R = R_{y,\varphi} R_{w,\theta} R_{u,\alpha} \\ = \begin{bmatrix} \cos \varphi & 0 & \sin \varphi \\ 0 & 1 & 0 \\ -\sin \varphi & 0 & \cos \varphi \end{bmatrix} \begin{bmatrix} \cos \theta & -\sin \theta & 0 \\ \sin \theta & \cos \theta & 0 \\ 0 & 0 & 1 \end{bmatrix} \begin{bmatrix} 1 & 0 & 0 \\ 0 & \cos \alpha & -\sin \alpha \\ 0 & \sin \alpha & \cos \alpha \end{bmatrix} \quad (3.32)$$

If an apple phantom rotates 45 angle about  $OX$  axis followed by a rotation of 30 angle about  $OW$  axis (Fig. 3.11), the resultant rotation matrix is

$$\begin{aligned}
 R = R_{x,45}R_{w,30} &= \begin{bmatrix} 1 & 0 & 0 \\ 0 & \cos 45 & -\sin 45 \\ 0 & \sin 45 & \cos 45 \end{bmatrix} \begin{bmatrix} \cos 30 & -\sin 30 & 0 \\ \sin 30 & \cos 30 & 0 \\ 0 & 0 & 1 \end{bmatrix} \\
 &= \begin{bmatrix} \cos 30 & -\sin 30 & 0 \\ \cos 45 \sin 30 & \cos 45 \cos 30 & -\sin 45 \\ \sin 45 \sin 30 & \sin 45 \cos 30 & \cos 45 \end{bmatrix} \quad (3.33)
 \end{aligned}$$

A Matlab script file, generating a rotation matrix for MCNP geometry, is presented Appendix B.1.

### 3.2.4 MCNP Input File

The input file for MCNP simulation of a wax apple is attached at Appendix B.2. A MCNP input file consists of three parts: cell card, surface card, and data card. Each part is separated with a blank line.

Sample geometry is described with cell and surface cards. At the wax apple simulation, lattice structure feature is used to integrate CT data into the MCNP geometry. Cell 1, one big bounding cell, describes a hexahedral lattice cell, which dimension is 8 cm  $\times$  7.52 cm  $\times$  8.16 cm. This large cell is filled with small lattice elements (0.5 cm  $\times$  0.07 cm  $\times$  0.07 cm), which are assigned with their own material numbers and densities. The center of the bounding cell is (-0.25, 0, -0.04).

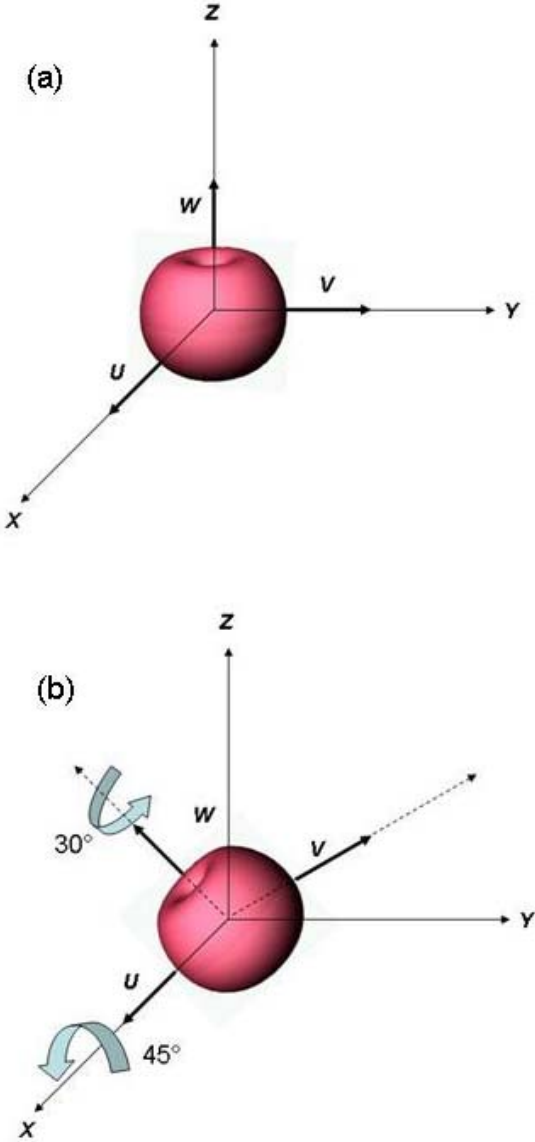


Fig. 3.11. Rotation of an apple phantom: (a) original position, and (b) rotation of 45 angle about  $Ox$  axis followed by rotation of 30 angle about  $Ow$  axis.

Since X-ray is the radiation source of the wax apple simulation, the MCNP must work in photon and electron transport mode (mode p e). SDEF defines general radiation source and X-ray energy spectra is used with source distribution functions, such as SI and SP. The numerical entries on the SP cards are the values of the probability density corresponding to the values on the SI cards. Material cards specify the isotropic composition of the materials (paraffin wax and air) in the cells. The tally card (\*f8:p,e) is used in the simulation to collect energy deposition within each cell. NPS defines the number of simulation histories to transport; MCNP will terminate after NPS histories, unless it has terminated earlier with some other reasons.

**CHAPTER IV**  
**DEVELOPMENT AND VALIDATION OF A METHODOLOGY FOR DOSE**  
**CALCULATION IN ELECTRON IRRADIATION OF COMPLEX-SHAPED**  
**FOODS\***

#### **4.1 Overview**

Obtaining a uniform dose in inherently irregularly shaped foods, such as an apple, is very difficult, and development of accurate dose calculation methodologies is needed. The specific objectives of this study were: (1) to obtain detailed, high resolution dose maps using CT scanning and Monte Carlo simulation techniques, and (2) to determine the accuracy of the dose calculation methodology by irradiating food phantoms with a Van de Graaff accelerator. Phantom apples were made using a mixture of chloroform, methyl yellow dye, and paraffin wax. Absorbed dose was determined by measuring the corresponding color changes of the dye in irradiated phantoms. 3-D dose distributions in the phantom and an actual apple were calculated using Monte Carlo methods. Both the measured and calculated dose distribution values in the phantom were very similar. Evaluation of food positioning strategies in front of the e-beam source demonstrated that tilting and axial rotation ensure uniform dose distribution of the entire

---

\* Reprinted with permission from “Development and validation of a methodology for dose calculation in electron beam irradiation of a complex-shaped foods” by Kim, J., Rivadeneira, R.G., Castell-Perez, M.E., & Moreira, R.G. (2006). *Journal of Food Engineering*, 74, 359-369. Copyright 2006 by Elsevier Ltd.  
Doi:10.1016/j.foodeng.2005.03.008

surface of the phantom, even reaching the critical regions of the apple stem and calyx ends.

## 4.2 Introduction

Contaminated raw vegetables, fruits, and fruit juices have all been vehicles for transmission of pathogens. These foods are often eaten raw without benefit of any pathogen killing step (Beuchat, 1996). Apples are one of the top five consumed fruits together with bananas, oranges, grapes, and grapefruits in the USA (USDA, 1999). Unpasteurized apple cider and juice have been associated with outbreaks of *Escherichia coli* O157:H7 infections that may be present on raw apples (CDC, 1996, 1997; Cody et al., 1999). The viability of pathogenic organisms on the surface of fresh fruits and vegetables can be significantly reduced by electron beam irradiation.

The use of electron beams for surface sterilization of foods, such as hamburger patties, which can be processed as relatively large uniform shaped blocks, is well established (Murano, 1995). The electron beam generated by accelerators has the ability to penetrate the product to a limited depth depending on the density and product characteristics and its direction can be pointed to a specific target. Hence, the dose at each point in an object exposed to electrons is affected by the shape and thickness of the object because electrons are easily attenuated and scattered by the material they pass through. For optimum results, it is important that the radiation dose (expressed in kiloGrays) be as uniform as possible throughout the food being treated. In this way, we can assure that all of the food receives the dose sufficient to produce adequate surface

sterilization and that none of it receives an excessive dose which might alter color, texture, flavor, or nutritional composition. Obtaining a uniform dose in inherently irregularly shaped foods is, however, much more difficult.

The correct procedure for food irradiation processing depends to a large extent on accurate and reproducible measurement of radiation quantities. When irradiation is done on a commercial scale, because of the large dose uniformity ratio, a vast majority of the food item will receive significantly greater than the minimum absorbed dose required for treatment efficacy, much of it two times or more (Hallman & Martinez, 2001).

Modeling and the measurement of dose distributions or three dimensional (3-D) dose mapping are an integral part of the qualification process for an irradiated product. Dose distributions are useful in determining positions of minimum and maximum dose inside the food and to guarantee that all the food products will attain the minimum required dose for sterilization. Current measurement methods have serious drawbacks, including geometry limitations, poor accuracy and precision and narrow energy ranges. When using conventional dosimetry techniques (alanine or radiochromic films), it is difficult to know exactly how much energy is absorbed in each element of the whole target (the food) (McLaughlin, Jarrett, & Olejuik, 1982). Additionally, in the case of surface sterilization, low energy electrons have a small penetration depth (for example, 0.5 cm in water for a 1 MeV source), thus making the placement of dosimeters into the product within this depth very problematic. Furthermore, food products have several locations where accurate positioning of a dosimeter is critical, such as the area around

the stem of an apple, or the convoluted surfaces of some type of leafy vegetables.

Consequently, developments of accurate dose calculation methodologies are needed.

Computer codes are readily available to calculate the dose distribution inside a product box and to “visualize” the effect of boundaries and interfaces between dissimilar materials in terms of their density, which are irradiated in the same box, as in the case of surgical blades (Hogstrom, Mills, & Almond, 1981; Loaharanu, 1995; Nahum, 1985). More recently, several radiation transport computer codes (RTCC) have been developed and/or adapted for dose distribution calculation in food irradiation processing (Mittendorfer, Colon, & Gratzel, 2004; Piña-Villalpando & Sloan, 1998; Rakhno & Roginets, 1998; Stenger, Halmavánszki, Falvi, Fehér, & Demirizen, 1998). However, these dose calculation methods do not adequately account for the complex 3-D structure of foods, inhomogeneity corrections (the targets were assumed to be composed of only water), and the lack of secondary electron equilibrium in and around the object.

The 3-D configuration of food products has been simulated by the juxtaposition of a number of regular geometries limited by well-defined quadric surfaces (Bielajew, 2001; Brescia, Moreira, Braby, & Castell-Perez, 2003; Salvat, Fernandez-Varea, Acosta, & Sempau, 2001). However, this approach does not provide an accurate description of the complex geometrical characteristics of most fruits and vegetables. The Monte Carlo technique is currently the most accurate method for dose calculation of electron beam interactions with matter (Andreo, 1991; Mackie, 1990). Among the Monte Carlo radiation transport codes available, the Monte Carlo N-Particle (MCNP) (Brown, 2003) along with the Electron Gamma Shower (EGS4) (Nelson, Hirayama, & Rogers, 1985)



have been used extensively in the area of medical physics for dosimetry applications. MCNP is able to handle complex geometries more easily than EGS4, using first and second degree surfaces and fourth degree application tori that are defined via Boolean operators.

The main difficulty in applying the conventional radiation transport codes for complex-shaped foods lies in obtaining the actual product geometry and density values. These values are critical factors in evaluation of electron/photon interactions.

Computed tomography (CT) scan is a diagnostic test that combines the use of X-ray with computer technology. Using multi-slice CT data, the geometrical and density information data obtained can be used to accurately calculate dose distribution in complex shaped products (DeMarco, Sloberg, & Smathers, 1998; Ito, 1987; Yoriyaz, Santos, Stabin, & Cabezas, 2000). More recently, Borsa, Chu, Sun, Linton, and Hunter (2002) successfully used CT scanning techniques to obtain dose maps in irradiated foods such as frozen whole chickens, cured hams, and boxed frozen chicken breasts. Therefore, the combination of CT scanning with Monte Carlo simulation could provide detailed and high resolution dose maps for complex-shaped fruits and vegetables.

Calculation and measurement of dose in the same object is required to determine the precision of isodose distributions calculated by mathematical models in situations involving irregular beam entry surfaces and heterogeneous objects such as foods. Since a real food object, such as an apple, would deteriorate during the dose measurements, it is vital that we do the validation with a dependable food-substitute material (plastic or wax) that mimics the geometric and chemical properties of the food that are relevant to

dosimetry. In radiation therapy, a phantom, i.e., a volume of a tissue substitute is used to simulate electron interactions. A chemical phantom dosimeter measures the dose by the quantitative determination of a chemical change; for example, color changes in proportion to the absorbed dose. The phantom can then be shaped into the desired 3-D geometries by using molding technology (Potsaid, 1963).

The specific objectives of this work were: (1) to obtain detailed, high resolution dose maps in an apple-phantom using CT scanning and Monte Carlo simulation techniques, and (2) to determine the accuracy of the calculations against the dose measured using a 2 MeV Van de Graaff accelerator.

## **4.3 Methodology**

### **4.3.1 Apple Phantom Dosimeter**

For analysis of dosimetry, phantom apples were used instead of actual apples. The phantoms were made using a mixture of a halogenated material (chloroform), a biological indicator (methyl yellow), and a polymer matrix (paraffin wax) to produce a relative density of approximately 1.0 similar to that of an average apple (Mohsenin, 1986). Future references to the phantom will mean the phantom apple.

Halogenated hydrocarbons, such as chloroform ( $\text{CHCl}_3$ ), release chlorine that is proportional to the radiation energy absorbed. This chlorine reacts with the nitrogen of methyl yellow dye (p-Dimethylaminoazobenzene,  $\text{C}_{14}\text{H}_{15}\text{N}_3$ ) to produce acid-salt, which is responsible for the color changes (Potsaid, 1963).

The practical advantages of paraffin wax are that it is readily available, easily worked, and freely mixed with halogenated hydrocarbons (Potsaid, 1963). Paraffin wax ( $C_{25}H_{52}$ ) not only provides rigidity to the dosimeter, but also has identical electron density and  $Z$  value (atomic number) to that of an actual apple. Although paraffin wax has been used as a common tissue substitute in radiation dosimetry and measurements (ICRU, 1989), it is important to determine how well this material matches the radiation interaction properties of an actual apple for e-beam treatment. Table 4.1 compares the calculated elemental compositions, density and  $Z$  values of the paraffin phantom with those of an actual apple. The phantom contained 70% of carbon (paraffin's hydrocarbon structure -  $C_{25}H_{52}$ ) and 18% of chlorine (from chloroform). No oxygen was present in the phantom. However, the carbon contained in tissue material substitutes the missing oxygen (ICRU, 1989); thus, in average, the phantom has identical electron density and  $Z$  value (atomic number) to that of an actual apple.

A mold was made by casting a medium size red delicious apple (7.5 cm diameter and 8.2 cm height) using a synthetic rubber (REPRORUBBER<sup>®</sup>, Flex Machine Corp, NY). Low-oil content (0.5%) paraffin wax with a melting point of 57 °C and microcrystalline wax (plasticizer) were obtained from a local store. The phantom composition was: 221.2 g paraffin wax (79.0% w/w), 56.0 g of chloroform (20.0% w/w), 2.8 g of microcrystalline wax (1.0% w/w), and  $25.2 \times 10^{-3}$  g ( $< 0.009\%$  w/w) of methyl yellow (p-Dimethylaminoazobenzene,  $C_{14}H_{15}N_3$ - Cross Organics, USA, Morris Plains, NJ). Chloroform concentration capable of producing useful radiation-induced color changes is between 4% and 40% by weight of solution (Porsaid, 1963).

Table 4.1  
The elemental composition and density of an actual apple and the phantom

Material	Elemental Composition [%/weight]					Density <sup>2</sup> [kg/m <sup>3</sup> ]	Z <sub>eff</sub> <sup>1</sup>
	H	C	N	O	Others		
Phantom	12.99 (± 0.12)	70.27 (± 0.21)	0.0168 (± 0.001)	---	17.72 Cl (± 0.15)	1008 (± 10)	7.43 (± 0.10)
Actual Apple (Red Delicious)	10.28 (± 0.15)	6.07 (± 0.08)	0.04 (± 0.003)	83.47 (± 0.78)	0.01 Mg, 0.01 Ca, 0.01P, 0.11K	1042 (± 10)	6.58 (± 0.09)

<sup>1</sup>effective atomic number; calculated as (Tsoufanidis, 1995):

$$Z_{eff} = \frac{\sum_i (W_i / A_i) Z_i^2}{\sum_i (W_i / A_i) Z_i}; \text{ where } A_i \text{ is the atomic mass, } Z_i \text{ the atomic number, and } W_i \text{ the}$$

weight fraction

<sup>2</sup> At room temperature. Mohsenin (1986).

Preliminary exposure tests, with gamma ray, showed that the range of color intensity was very narrow in the low and high concentration levels.

The paraffin wax was melted in a water bath at  $68 \pm 2$  °C and all the other ingredients added to the mixture. The mixture was then poured into the apple-shaped rubber mold and allowed to cool down slowly (at room temperature of  $22 \pm 2$  °C) to minimize shrinkage effects. The phantom was carefully removed from the mold and stored before and after irradiation in a dark room at a temperature of  $22 \pm 2$  °C and a relative humidity of 50%.

#### **4.3.2 Measurement of Dose Distribution**

The experimental part of this study was performed using a 2-MeV Van de Graaff accelerator (High Voltage Engineering Corp., Cambridge, MA) located at the Department of Biological & Agricultural Engineering at the Texas A&M University campus.

The electron beam leaving the accelerator tube goes along the beam line until it reaches the bending magnet where the beam is scanned (Fig. 4.1). The accelerator's circular scanning horn was directed  $22.5^\circ$  downward from the horizontal beam line (Fig. 4.2).

The phantom was placed in front of the accelerator in an over-head metal conveyor. The conveyor moved the phantom laterally at a controlled speed, stopped in front of the exit-beam window, and rotated the phantom by its axis, by means of a sprocket-belt rotating mechanism. To monitor the electron beams generated from the

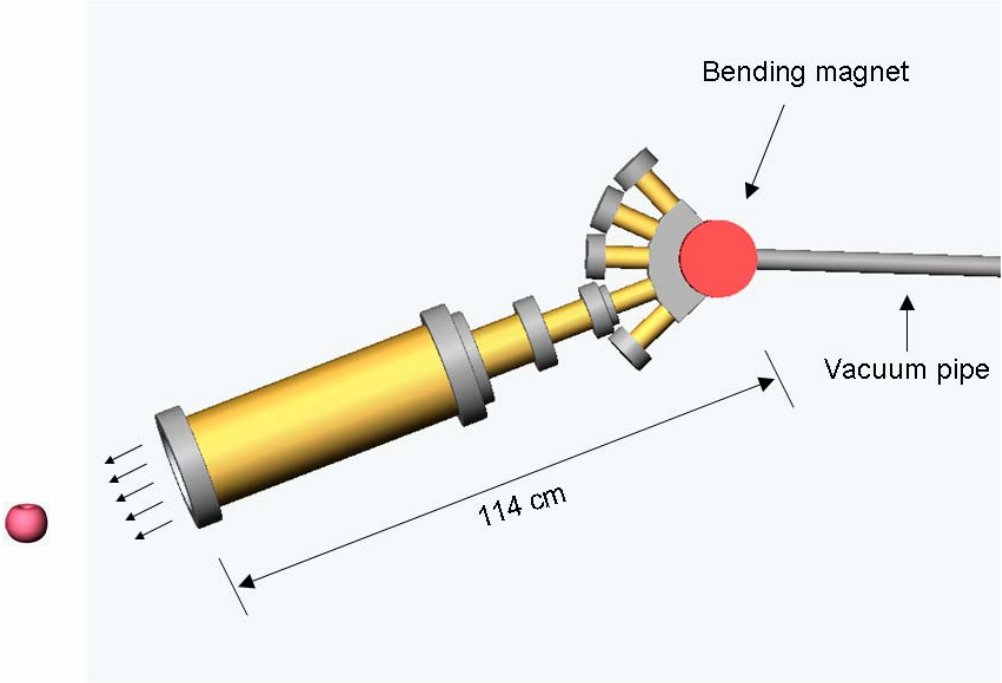


Fig. 4.1. Scanning electron beam.

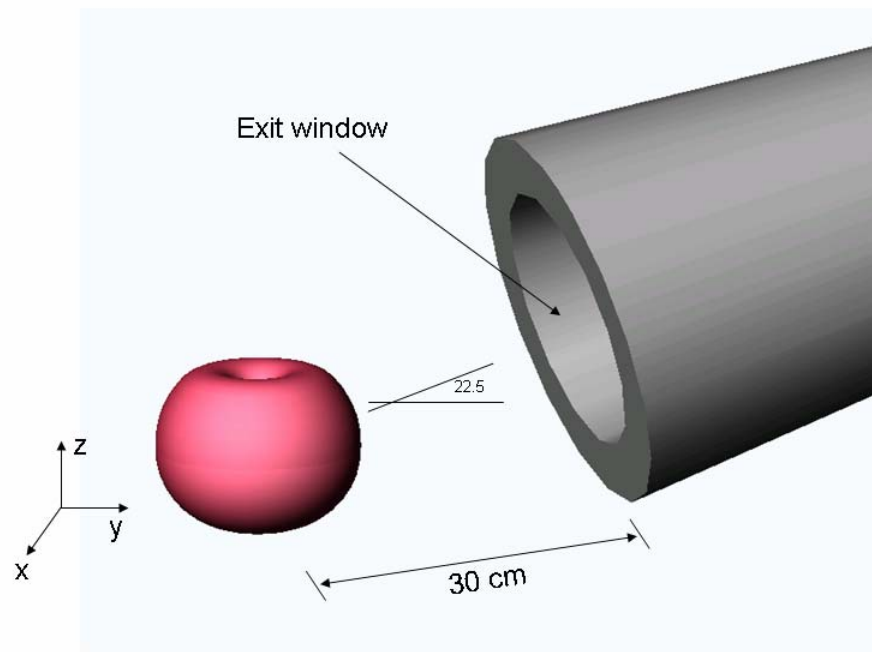


Fig. 4.2. Placement of the phantom dosimeter in front of the electron beam exit window.

accelerator, a parallel-plate transmission ion chamber with aluminum foil and Lucite was constructed and placed right ahead of the exit beam window.

The temperature and relative humidity during all irradiation experiments were  $22 \pm 2$  °C and 50%, respectively. The duration of time of the dose readings was 24 hour after irradiation. Preliminary observations showed that color intensity after irradiation significantly increased over the first few hours and became relatively stable after approximately 24-48 hour.

The phantom was cut in  $3.2 \pm 0.1$  mm-thick slices with a band saw before and after irradiation in order to measure the color distribution changes due to the response of the methyl yellow dye to irradiation dose. A flat bed scanner (Microtek<sup>®</sup> ScanMaker 8700, Carson, CA) was used to obtain the color images that consisted of three components (RGB): Red, Green, and Blue. Preliminary observations showed that the intensity of the green component varied the most with dose, as expected, due to the dosimeter's color change from yellow to red. The scanned images were analyzed using the Image Processing Toolbox of Matlab (MathWorks, Natick, MA) for mapping of the isodoses. A calibration procedure using a Farmer ionization chamber (Nuclear Enterprises, Reading, UK) allowed conversion of the green intensity data to dose values in kGy.



### **4.3.3 Dose Distribution Calculation**

#### **4.3.3.1 CT Scanning**

When samples are scanned using a CT scanner, multi-sliced CT data are obtained and each pixel on the slice image is assigned a numerical value (CT number), e.g. fat is about -200 to -5, and water is about -5 to 5, which is related to the densities of the scanned materials. A total of 16 slice images (5-mm thickness) were obtained from the phantom using a 12-cm field of view (pixel size = 0.23 mm) in a Universal HD350E X-ray CT scanner (Universal System, Dolon, OH). The CT slices were then transferred to a UNIX machine (Solaris OS, Sun Microsystems, Santa Clara, CA) for data analysis and storage. The CT data were later retrieved using the VoxelCalc Plus<sup>®</sup> (KehlCo, Inc., Houston, TX) software, and stored for further analysis.

#### **4.3.3.2 Reconstruction of CT-based Phantom Dosimeter**

Each slice of CT data (512 x 512 matrixes) was processed using the Image Processing Toolbox of Matlab (MathWorks, Natick, MA). The 2-D slice CT data were made into a 359 x 362 voxel array, in which the  $y$ ,  $z$  resolution was 0.23 mm per pixel and the slice thickness was 5 mm. To reconstruct the 3-D volume, all the CT data was placed into a 359 x 362 x 16 matrix where the voxel resolutions were 0.23 mm, 0.23 mm, and 5 mm on each side. This volume array was created by combining pixels in the  $y$ ,  $z$  plane and by duplicating the slices along the  $x$  direction.

#### 4.3.3.3 Monte Carlo Simulation

The MCNP-5 (Monte Carlo N-Particle- Version 5) used in this study was developed at the Los Alamos National Laboratory (Radiation Safety Information Computational Center (RSICC), Oak Ridge National Laboratory, Oak Ridge, TN). This code is capable of simulating coupled electron-photon problems using a three dimensional combinatory geometry system. The simulator was run in a parallel computer platform (Dell™ PowerEdge™ 6650, 4 CPU) located at the Department of Biological and Agricultural Engineering at Texas A&M University.

In this study, we simulated a surface pasteurization treatment of the actual apple and the phantom with the 2-MeV e-beam Van de Graaff linear accelerator. The information from Table 4.1 was used as input to the simulation. The e-beam source was described as a parallel plane large enough to cover the target, and the electrons were emitted in a plane and distributed evenly within the scan angle (Fig. 4.1). The phantom was positioned parallel to the source plane with its axis of rotation (90 - 270°) at 30 cm in front of the source (Fig. 4.2). The front of the phantom runs from the 90° through 180° to the 270° position. This region is defined as the front face (Fig. 4.3).

Generally, Monte Carlo simulation results represent an average of the contribution from many histories sampled during the course of the problem (Brown, 2003). Therefore, a total of  $10^6 - 10^7$  histories were used in our simulation to reduce the statistical uncertainty to about 5% or less.

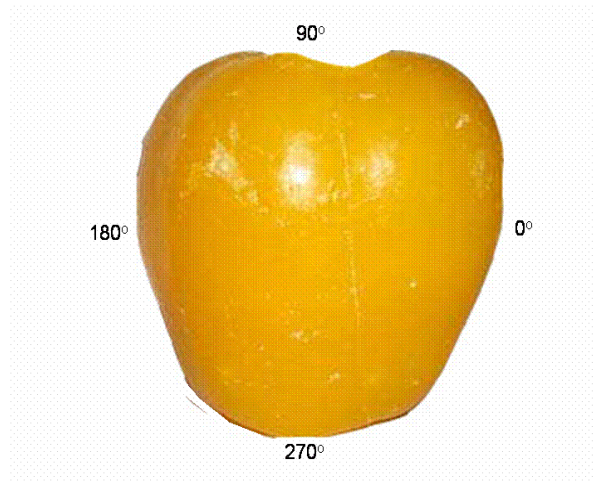


Fig. 4.3. The phantom and its regions:  $0^\circ$  and  $180^\circ$  correspond to the right and left position, and  $90^\circ$  and  $270^\circ$  correspond to the top and bottom position, respectively.

## 4.4 Results

### 4.4.1 Dose Calculation Comparison Between the Phantom and an Actual Apple

For the phantom and the actual apple to absorb and scatter electrons to the same extent, both total linear stopping powers (TSP) must be identical over the operating energy range used in the radiation treatment. The stopping power is defined as the rate of energy loss suffered by a charged particle in traversing a unit path length of a medium and it is related to the charge and velocity of the incident particle, and physical property of the medium.

The total linear stopping power,  $S$ , for electrons includes the total energy loss,  $dE$ , by collision and bremsstrahlung production for a path length  $dx$  in the medium as,

$$S = \frac{dE}{dx} = \left( \left( \frac{dE}{\rho \cdot dx} \right)_{col} + \left( \frac{dE}{\rho \cdot dx} \right)_{rad} \right) \cdot \rho \quad (4.1)$$

where  $\rho$  is the density of the medium,  $(dE/\rho dx)_{col}$  is the mass collision stopping power which includes all energy losses in particle collisions that directly produces secondary electrons (delta rays) and atomic excitations and,  $(dE/\rho dx)_{rad}$  is the mass radiative stopping power which includes all energy losses of the primary electron which lead to bremsstrahlung production (ICRU, 1984).

Fig. 4.4 shows that the TSP values for both the phantom and the actual apple overlap throughout the entire range of energy. Therefore, the developed phantom can be

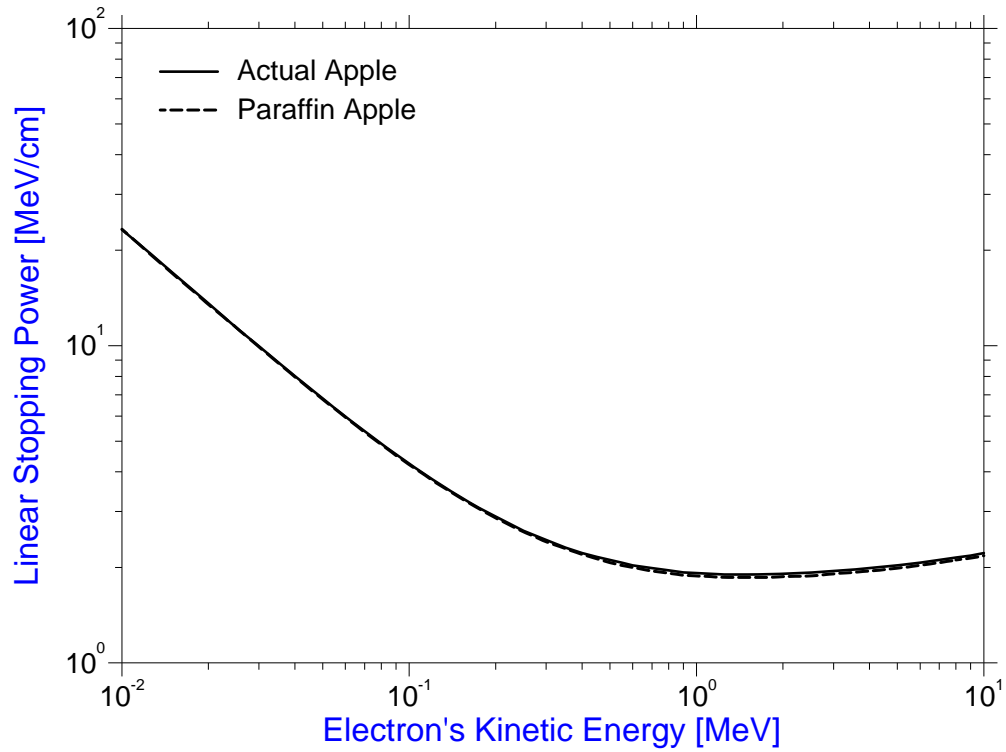


Fig. 4.4. Total stopping power (TSP) of an actual apple and the phantom (paraffin apple) with corresponding electron energy.

used for simulation studies of e-beam irradiation of an actual apple for an energy source range of 0.01 – 10 MeV.

Fig. 4.5 presents the calculated dose distribution at the vertical plane ( $z$ ) in both “apples” for an e-beam source of 1.35 MeV (midrange capacity of the accelerator). The simulated dose distributions for both targets were very similar. The maximum dose contours were at the region between  $20^\circ$  and  $40^\circ$  and below the right shoulder, for both targets.

As the electrons enter the phantom (Fig. 4.5-top), all the energy is deposited within 0.7 cm from the incident surface (maximum depth for a 1.35 MeV e-beam source). The doses along the beam direction ( $22.5^\circ$ ) showed a depth-dose profile typical of a homogeneous material (Fig. 4.6). The dose value tends to rise with increasing depth within the material to about the midpoint of the electron penetration range and then it rapidly falls to low values. This reduction in dose is due to two factors: (1) low kinetic energy electrons scatter easily as the electron’s incident angle decreases, and (2) the number of knock-on electrons escaping from the target’s surface increases.

As the electron’s entrance angle decreased towards the bottom of the phantom, the dose distribution showed a faster increase up to their peak value ( $4.5 \times 10^{-10}$  Gy  $\text{cm}^2/\text{electron}$ ) before tailing off (Fig. 4.6). Fig. 4.6 shows the calculated depth-dose curves for both targets for a 1.35 MeV e-beam source. From 0 to 0.28 cm from the surface, the absorbed energy values of the phantom (paraffin apple) were slightly lower than those of the actual apple; however, from 0.28 to 1.13 cm both targets showed almost the same dose value and same penetration depth (0.7 cm.).

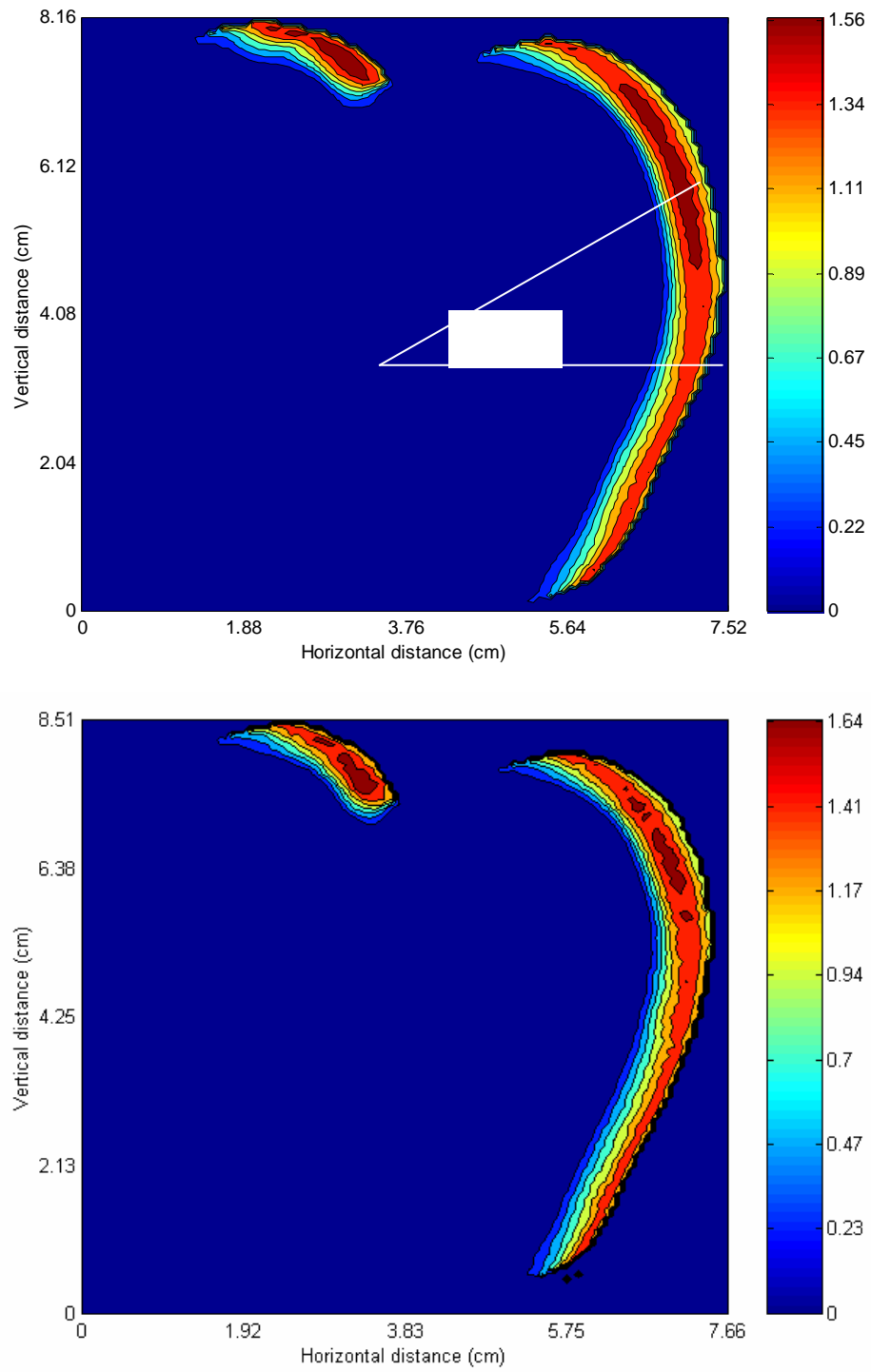


Fig. 4.5. Simulated dose distribution for a 1.35 MeV e-beam source in the phantom (top) and an actual apple (bottom).

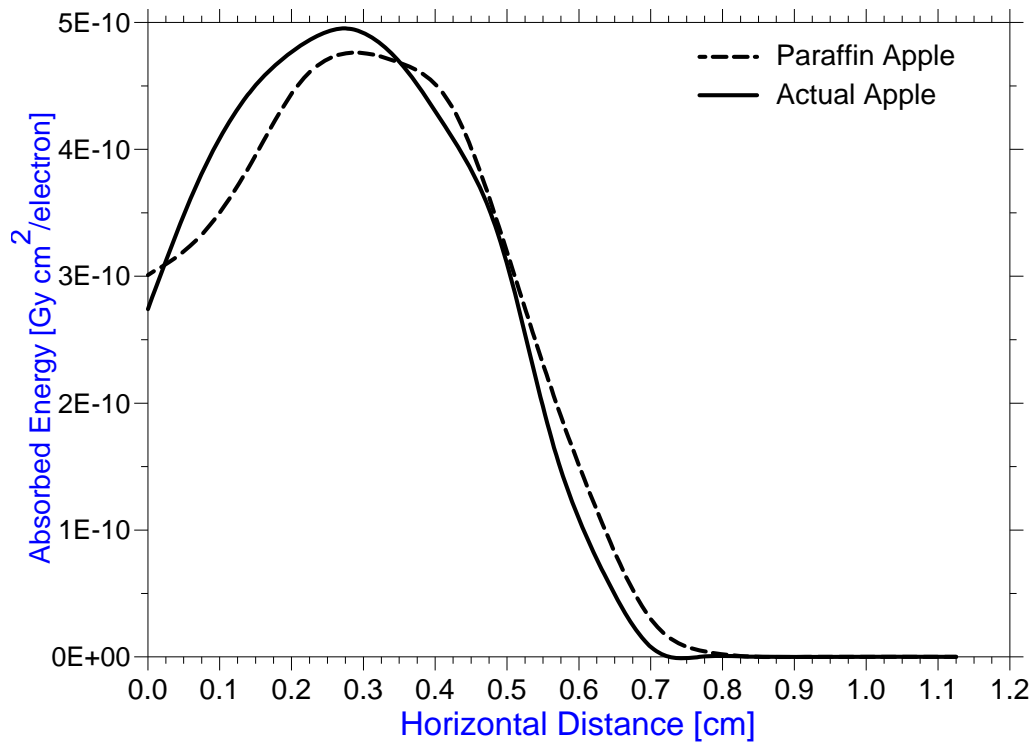


Fig. 4.6. Depth-dose curves in the phantom (paraffin apple) and the actual apple for a 1.35 MeV e-beam source.



We should note that the maximum dose received by the actual apple is slightly higher than that for the phantom. However, the calculated relative errors between the two simulations at the maximum value are only 2%. As shown in Fig. 4.6, the maximum dose of the actual apple is also slightly higher ( $4.9 \times 10^{-10}$  Gy cm<sup>2</sup>/electron) than in the phantom ( $4.5 \times 10^{-10}$  Gy cm<sup>2</sup>/electron), even though their linear stopping power curves are identical (Fig. 4.4). These differences are attributed to the fact that the phantom has a uniform density (Fig. 4.7b-top) while the actual apple shows some variation in density (Fig. 4.7a-top). Since dose is calculated by dividing the absorbed energy (the stopping power) by the target mass, the dose for a lower density material will be larger than for a material with higher density, as long as their stopping powers are similar.

All these results (TSP, dose contour, and depth-dose curve) confirm that the developed paraffin-based phantom is suitable for use in radiation simulation studies of electron interactions in complex-shaped products.

#### **4.4.2 Dose Measurement Using the Phantom Dosimeter**

When the phantom dosimeter was exposed to e-beam energy sources, its color changed from yellow to red with the intensity of color proportional to the absorbed dose (Fig. 4.7).

Fig. 4.8 shows the good agreement between the measured dose contour (Fig. 4.8-bottom) and the simulated results (calculated dose) (Fig. 4.8 - top) using the phantom. Both dose maps indicate that the maximum dose values were located between 20° and

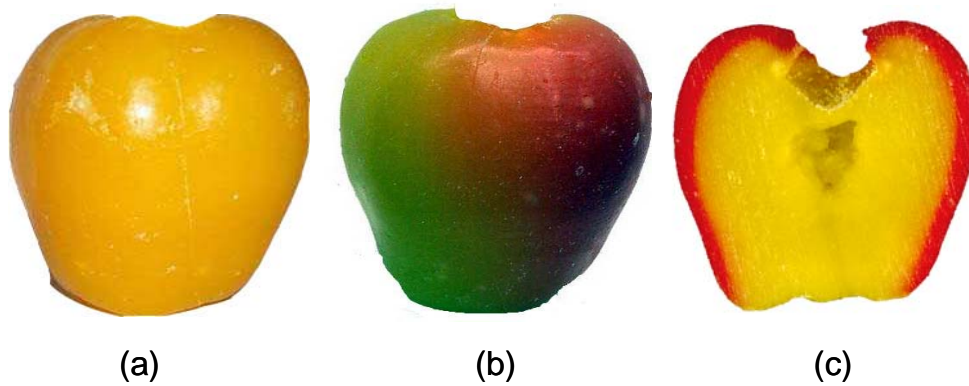
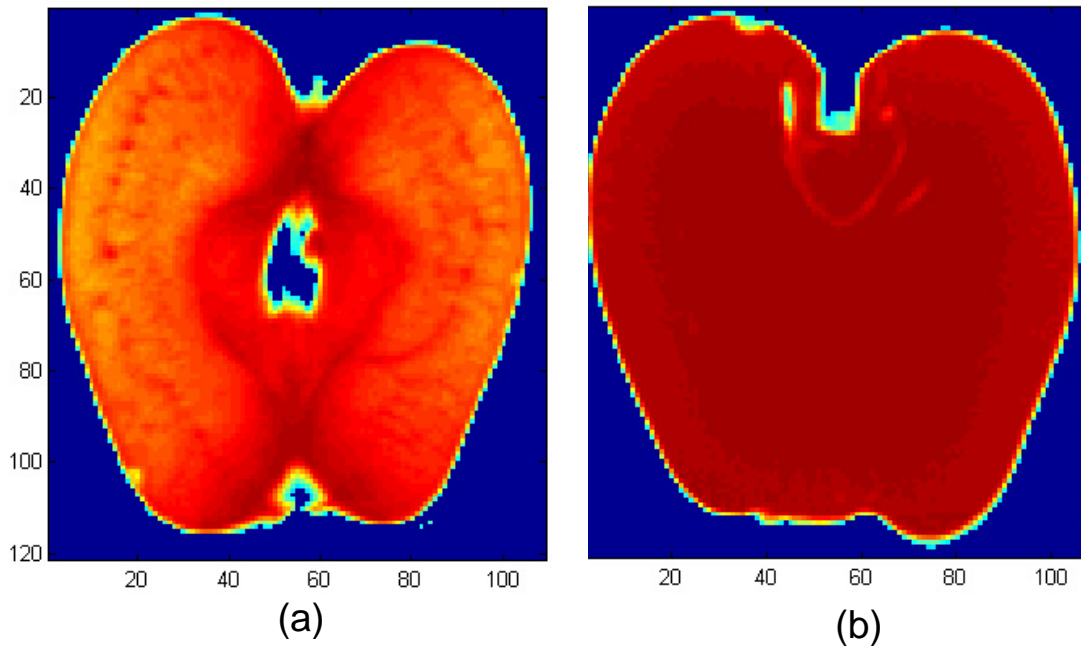


Fig. 4.7. *Top*: Density distribution in (a) actual apple; and (b) phantom. *Bottom*: Phantoms: (a) before irradiation; (b) after irradiation; (c) vertical (y-z) plan view after irradiation.

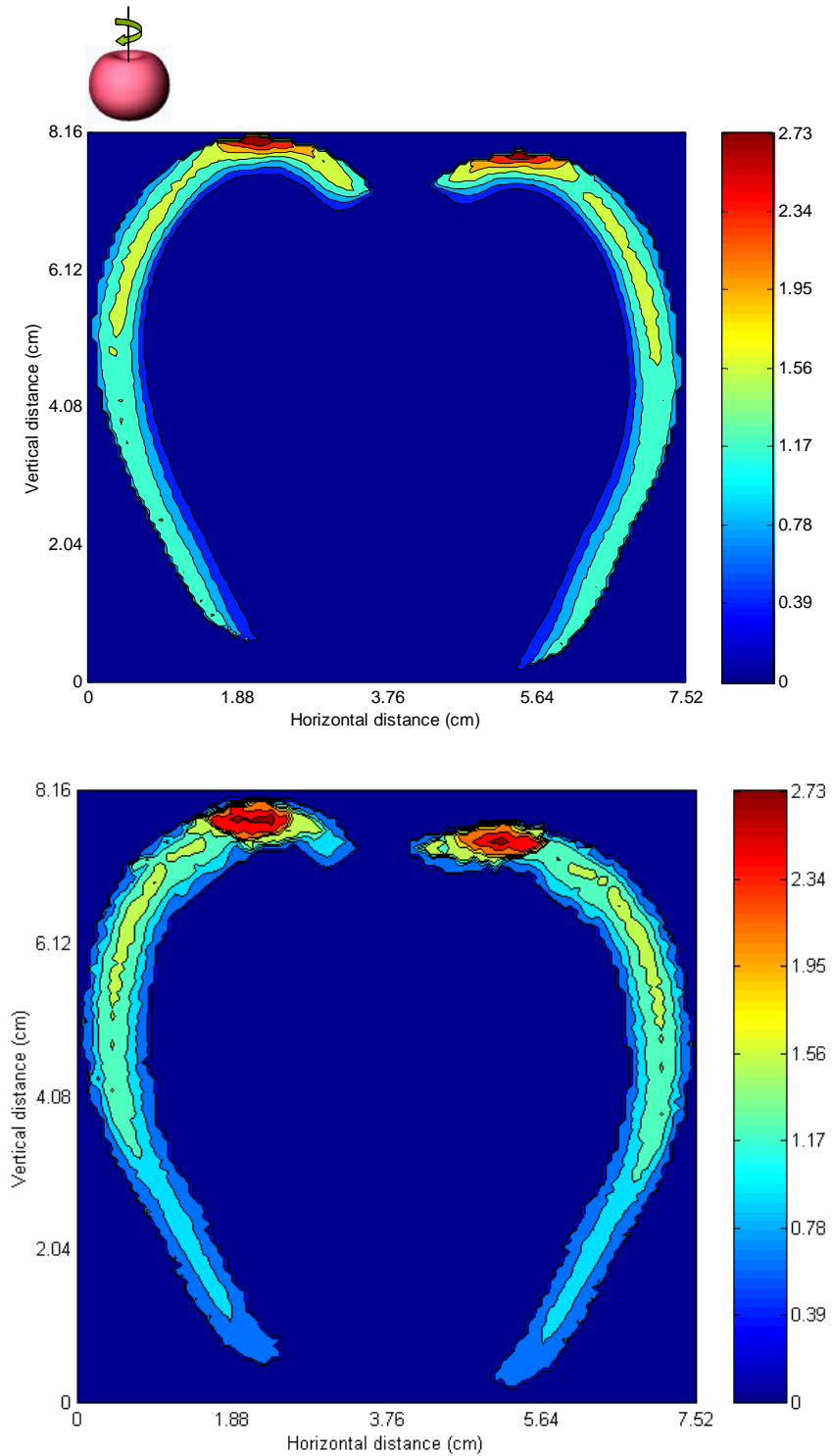


Fig. 4.8. Simulated (top) and measured (bottom) dose contour maps in the phantom for a 1.35 MeV e-beam source. The target was rotated by its axis around the e-beam source.

60°, and the dose distribution tapered towards the right and left lower part of the phantom. Thus, the distribution is not uniform for proper pasteurization of the target.

#### **4.4.3 Rotation Strategies for Uniform Dose Distribution in Target**

Based on the results above, we used the phantom to determine how to obtain the desired uniform dose distribution at the surface of the sample. We evaluated different sample rotation strategies, both against and toward the e-beam source. The results are presented in the following sections.

#### **4.4.4 Simulated Dose Distribution in the Phantom**

All surfaces of the phantom exposed to the incident electron beam absorbed more dose (Fig. 4.5 - top) with the exception of the right side of the stem cavity (around the 90° position – see Fig. 4.3). This is due to the fact that the electron's incident angle is zero at that location and none of the electrons could enter into the surface. The cavity of the stem, just like the surface opposed to the electron beam (the region covered by 115° through 290° positions – see Fig. 4.3), did not show any energy absorption.

The depths at maximum dose values varied with position within the phantom. From 0° through 45° regions (Fig. 4.3), the maximum dose value was determined at a depth of 0.3 – 0.4 cm from the surface, i.e., about half of the maximum penetration depth (0.7 cm). At the right lower region (270 - 360°), the maximum dose value was located at only 0.07 cm from the surface. As a result, in the application of e-beam irradiation treatment of complex-shaped fruits and vegetables, the products must be positioned as

tilted in an angle against the e-beam source to minimize the non-uniformity of dose distribution throughout the product's surface (Brescia et al., 2003). Consequently, if microorganisms are distributed in very shallow depths from the product's surface, the incident electrons would effectively kill the microorganisms while maintaining the quality of the product.

By rotating the phantom one revolution in front of the e-beam source, the whole surface of the phantom was exposed to the radiation energy (Fig. 4.8 - top). Unlike the one-sided irradiation scenario, the maximum dose regions were located on both top surfaces of the phantom, since both regions were continuously exposed to the electron beam during rotation. Even though irradiation exposure of the stem cavity improved after rotation of the phantom, there were still some unirradiated areas around the stem and the basin of the sample. By rotating the phantom at its normal standing position (i.e., its vertical axis positioned at  $67.7^\circ$  against the source), some regions did not receive any dose at all.

The next scenario was to simulate the phantom as being initially in an upside down position and then as rotating against the e-beam source so that the bottom surface would be exposed to irradiation. The combination of these two rotations (up and down positions around the  $z$ -axis) significantly increased the surface area exposed to the electron beam (Fig. 4.9 - top). However, the dose distribution was different from that shown in Fig. 4.8 - top; i.e., the maximum dose values were now located around the regions around the larger diameter of the apple. Still, the recesses of the stem were not irradiated, and the right and left top surfaces of the phantom also received higher doses

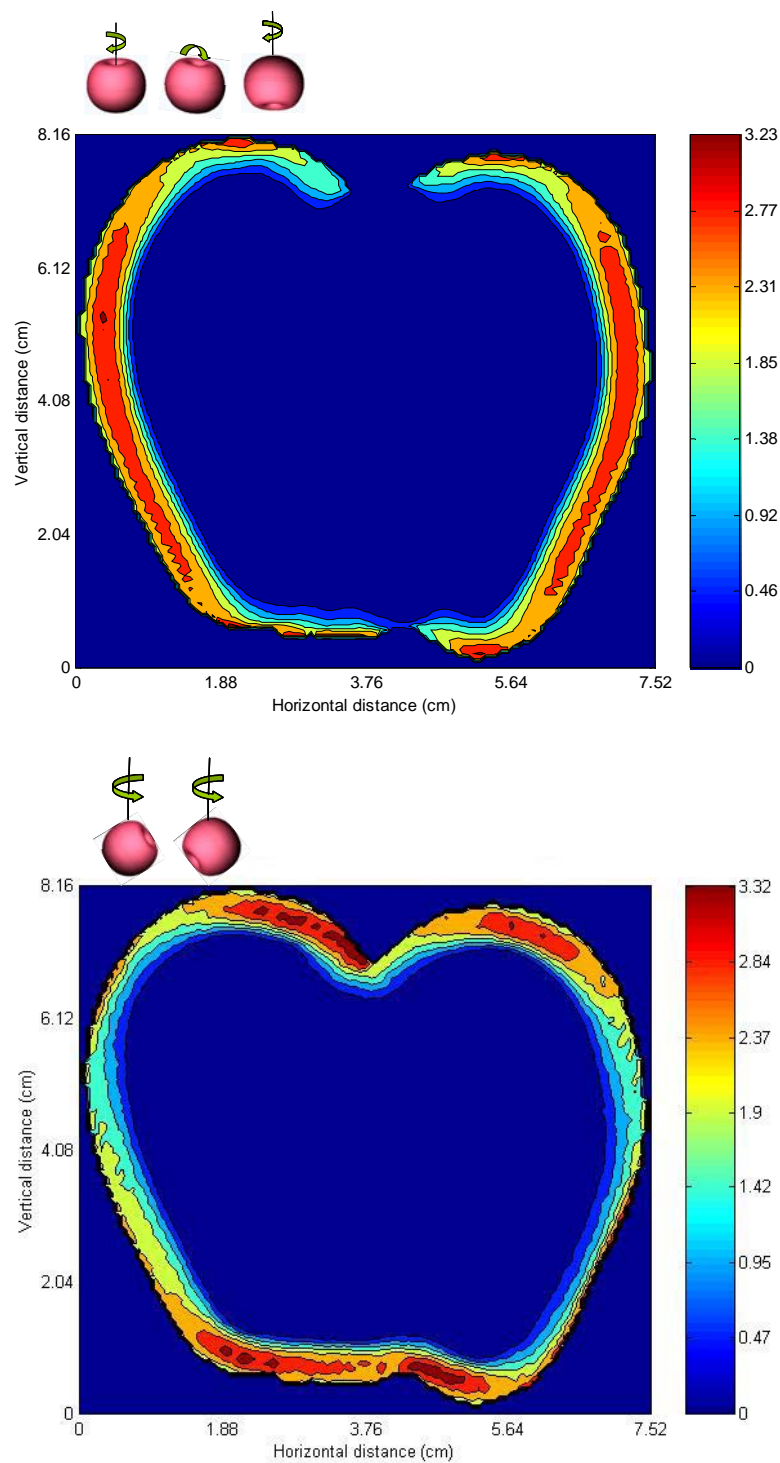


Fig. 4.9. Simulated dose distribution in the phantom dosimeter for a 1.35 MeV e-beam source. Target rotated twice: (Top) first round the axis (up and down positions); (Bottom) second at an angle in front of the source, 0 and 180°

(about 3.23 kGy). At the bottom region of the phantom, the dose values were also higher (3.23 kGy) and the energy penetration depth was shorter (about 4 cm) than the value obtained at the larger diameter surfaces. In conclusion, these rotation combinations will likely not be enough to uniformly irradiate the whole surface of the sample, especially the regions around the recesses of the stem. This is critical because, in general, the calyx end of an apple is an area of great concern with regard to the infiltration of bacteria (Burnett, Chen, & Beuchat, 2000). The infiltration occurs through the blossom of the calyx and progresses up to the floral tube into the core region. The stem of the apple is also hard to contact with chemical sanitizers in conventional decontamination processes.

The next scenario we considered was to evaluate whether we would be able to irradiate the whole surface of an apple (i.e., the phantom) by tilting the target at a certain angle in front of the source. The  $z$ -axis of the phantom was tilted about  $67.5^\circ$  so that it coincided with the e-beam exit window angle. The phantom was then first rotated with its  $0^\circ$  region parallel to the beam source with a second rotation with the  $180^\circ$  region parallel to the same source (Fig. 4.9-bottom). This rotation strategy ( $0^\circ$  and  $180^\circ$  region), made it possible to expose the entire surface of the phantom to the irradiation source which resulted in larger dose accumulation at the top and bottom regions. Thus, low energy electrons can penetrate these critical points in the sample and effectively remove pathogens from complex-shaped food such as apples.

#### **4.5 Conclusions**

In this study, 3-D dose maps were obtained in phantoms of shape like an apple using CT scanning and Monte Carlo simulation. The phantom showed electron interaction characteristics very similar to an actual apple. The measured and calculated dose distributions in the phantom showed good agreement, thus supporting the validity of using simulation methods and chemical phantom techniques for accurate planning of food irradiation treatments.

The developed methodology can provide 3-D dose distributions in complex-shaped food products with great accuracy. It is expected that this new approach will greatly reduce the risk of foodborne illnesses. Through a good irradiation-planning based on the developed methodology, the increased shelf life and improved quality of the food products would significantly reduce the economical losses from spoilage and would even allow for overseas marketing. In addition, consumers may be convinced of the safety of irradiated food through accurate dose distribution.



## CHAPTER V

### MONTE CARLO-BASED FOOD IRRADIATION SIMULATOR\*

#### 5.1 Overview

The Monte Carlo electron-transport simulation (MCNP-5) and computer axial tomography (CT) scan technology were used to predict the dose distribution in an irregular-shaped food product, an apple-phantom composed of paraffin wax, chloroform, and methyl yellow. The Monte Carlo code used was successfully tested against the experimental data, resulting in less than 5% discrepancy between the simulation and measured data.

The geometry and composition CT data of a real apple (Red Delicious) was then used to simulate the dose distribution in an apple irradiated by 1 and 5 MeV photon beams. For the 5 MeV photon simulations, a lesser amount of energy was deposited closer to the surface (at the right-side surface) of the apple. It also show more uniform in the forward direction. For a 1 MeV simulation, higher energy was distributed at the right half of the apple, and there was not a warming-up region as shown in the 5 MeV simulation.

---

\* Reprinted with permission from “Monte Carlo-based food irradiation simulator” by Kim, J., Moreira, R.G., Rivadeneira, R. & Castell-Perez, M.E. (2006). *Journal of Food Process Engineering*, 29(1), 72-88. Copyright 2006 by Blackwell Publishing.

## 5.2 Introduction

The electron beam (e-beam) generated by accelerators has the ability to penetrate the product to a limited depth depending on its density and characteristics, and the beam direction can be pointed to a specific target. Obtaining the detailed 3-D dose maps required to validate the suitability of irradiating complex food items using e-beams can be very difficult, because the density inhomogeneities tend to be randomly distributed and of variable geometry and magnitude. This is even more difficult in the case of high energy electrons (10 MeV) because their dose distributions can have very steep gradients, giving rise to large variations in absorbed dose over relatively short distances (Braby, 2004).

A very large field of e-beam would be required to irradiate a whole food sample. For optimum results, it is important that the radiation dose be as uniform as possible throughout the material being treated. In this way, we can assure that all of the material receives the dose sufficient to produce adequate pasteurization and no part receives an excessive dose, which might alter color, texture, or flavor.

Conventional dose calculation methods do not adequately account for the complex 3-D structure of foods, inhomogeneity corrections, and the lack of secondary electron equilibrium in and around the object. The Monte Carlo electron transport simulates the behavior of irradiation particles as they interact with atoms in the food during a typical radiation treatment. By combining the advanced concepts of irradiation physics with the explosive growth in computer technology, the accuracy of Monte Carlo-

based calculations can be brought to the food industry (Kim, Rivadeneira, Castell-Perez, & Moreira, 2006b).

When electrons are shot into matter, they interact with one or more electrons or with the nucleus of practically every atom they pass. Most of these interactions individually transfer only minute fractions of the incident particle's kinetic energy such that they lose their energy gradually in a friction like process. All 1 MeV electrons generally would undergo almost  $10^5$  interactions before losing all of their kinetic energy.

There are some currently available analytical methods to simulate the transport of electrons through the material; however, they show large uncertainties, especially in irradiated volumes that contain inhomogeneities (Hogstrom et al., 1981; Nahum, 1985). The Monte Carlo method is currently the most accurate method for dose calculation in e-beams transport (Andreo, 1991; Mackie, 1990).

Geometrical and density information for accurate dose calculation can be obtained by using multi-slice computer axial tomography (CT) scan data (Ito, 1987). These data have been used in 3-D dose distribution inpatient (DeMarco et al., 1998; Pawlicki & Ma, 2000). X-ray has been explored for inspecting the interior of agricultural commodities (Keagy, Parvin, & Schatzki, 1996; Lammertyn et al., 2001; Tollner et al., 1992). Brecht et al. (1991) used CT scan to determine maturity of green tomatoes. However, there is no literature on use of CT data for radiation simulation of foods.

The objectives of this work were: (1) to accurately predict dose distribution in irregularly shaped food products using the Monte Carlo electron transport theory together with CT scan technology; (2) compare simulated and measured dose

distributions in an apple-phantom; and (3) to simulate energy deposition in an actual apple based upon a 1 and 5 MeV X-ray source.

### **5.3 Materials and Methods**

#### **5.3.1 Paraffin Apple Phantom**

For dosimetry analysis, apple phantoms were used instead of actual apples. The phantoms were made using a mixture of a halogenated material (chloroform), a biological indicator (methyl yellow), and a polymer matrix (paraffin wax) to produce a specific density of approximately 0.83 similar to that of an average apple (Mohsenin, 1986). Development of the phantom is described in detail in Rivadeneira (2004).

For the phantom and the actual apple to absorb and scatter electrons to the same extent, both total linear stopping powers (TSP) must be identical over the operating energy range used in the radiation treatment. The stopping power is defined as the rate of energy loss suffered by a charged particle in traversing a unit path length of a medium and it is related to the charge and velocity of the incident particle, and physical properties of the medium. Kim et al. (2006b) showed that the TSP values for both phantom and actual apple were identical, so the developed phantom can be used for practical studies of e-beam irradiation of an actual apple for an energy source range of 0.01 – 10.00 MeV.

## **5.3.2 3-D Image Reconstruction**

### **5.3.2.1 CT Scanning**

When food samples are scanned by a CT scanner, multi-sliced CT data are obtained and every pixel on the slice image is assigned a numerical value (CT number), e.g., fat is about -200 to -5, or water is about -5 to 5, which is related to the densities of the scanned materials. A total of 16 slice images were acquired from the sample with a 5 mm slice thickness using a 12 cm field of view (pixel size = 0.23 mm) (Universal HD350E X-ray CT scanner; Universal System, Dolon, OH). The CT slices were transferred to a UNIX machine (Solaris OS, Sun Microsystems, Santa Clara, CA) to read and archive the CT data, then retrieved using the VoxelCalc Plus<sup>®</sup> (KehlCo, Inc., Houston, TX) software and finally saved for further analysis (Kim et al., 2006b).

### **5.3.2.2 Reconstruction of CT-based Phantom**

Each slice of CT data (512 x 512 matrixes) was processed using the Image Processing Toolbox of Matlab (MathWorks, Natick, MA). The 2-D slice CT data were made into a 359 by 362 voxel array, in which the  $y$  and  $z$  resolution was 0.23 mm per pixel with a slice thickness of 5 mm. To reconstruct the 3-D volume, all the CT data was placed into a 359 x 362 x 16 matrix where the voxel resolutions were 0.23, 0.23, and 5 mm on each side. This volume array was created by combining pixels in the  $y$  and  $z$  planes and duplicating the slices along the  $x$  direction (Kim et al., 2006b). Fig. 5.1 illustrates the steps for the apple 3-D image reconstruction based on CT data.

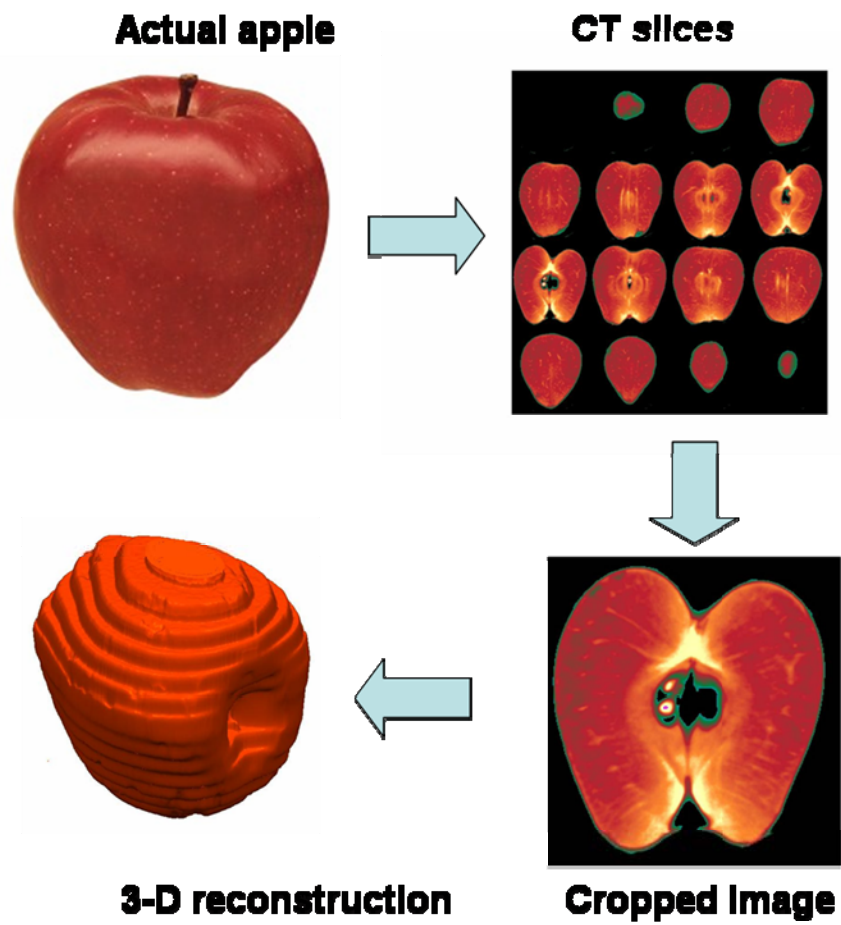


Fig. 5.1. The steps required for the development of the 3-D image of a Red Delicious apple.

### 5.3.3 Monte Carlo Simulation

The Monte Carlo N-Particle, Version 5 software (MCNP-5) used in this study was developed at the Los Alamos National Laboratory (Radiation Safety Information Computational Center (RSICC), Oak Ridge National Laboratory, Oak Ridge, TN). This code is capable of simulating coupled electron-photon problems using a 3-D combinatory geometry system. The simulator was run in a parallel computer platform (Dell™ PowerEdge™ 6650, 4 CPU) located at the Department of Biological and Agricultural Engineering at the Texas A&M University.

We simulated irradiation treatment of an apple phantom with a 10 MeV electron beam linear accelerator (LINAC) and with a 5 MeV X-ray linear accelerator (LINAC). The e-beam and X-ray source (photons) were described as a parallel plane large enough to cover the target. In the LINAC, the electrons and photons were emitted in a plane and distributed evenly within the scan area (Fig. 5.2).

For the e-beam study, z-axis of the apple phantom was positioned parallel to the source plane between the sources, i.e., the accelerator was run in dual beam mode (Fig. 5.2a). A uniform parallel source containing 10 MeV electrons was used (a LINAC with an exit window dimension of 7.4 x 61.0 cm). In this simulation, we only used the area covered by the phantom (8.0 x 7.4 cm<sup>2</sup>).

For the X-ray study, the simulation studies were based on the image developed from the CT data of an actual apple (Red Delicious). The photon beams (10 cm long and 1 cm wide plane) were defined to be directly in front of the right side of the apple as illustrated in Fig. 5.2b.

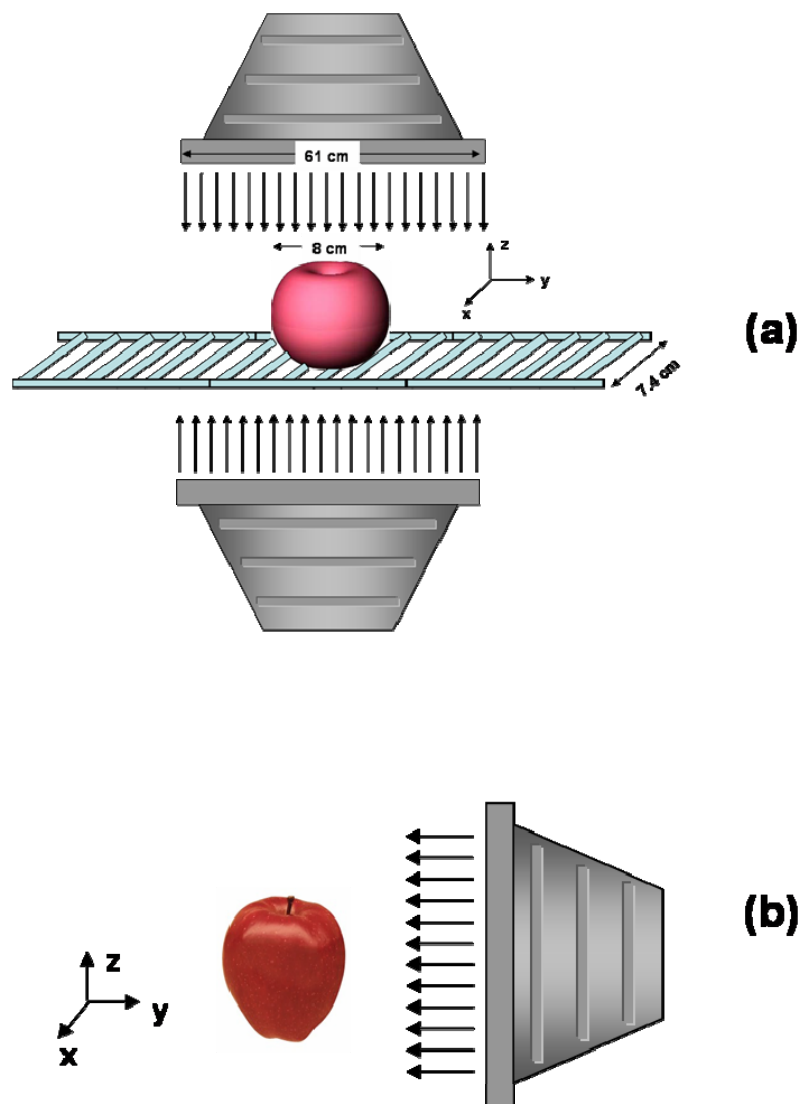


Fig. 5.2. Schematic representation of the experimental setup for irradiation of the apple using (a) 10 MeV LINAC in dual e-beam mode and (b) schematic of simulation setup of a broad parallel photon beams incident in an apple (1-5 MeV X-ray LINAC).



Generally, Monte Carlo simulation results represent an average of the contribution from many histories sampled during the course of the problem. A total of  $10^8$  histories were used to reduce the statistical uncertainty to about 5% or less (Brown, 2003).

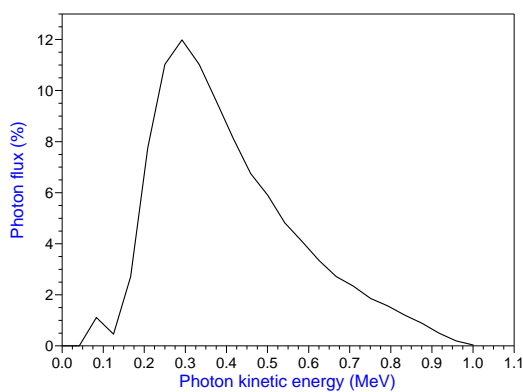
Table 5.1 shows the input parameters used for the Monte Carlo dose distribution simulation in the apple phantom and the real apple irradiated using e-beam and X-rays, respectively. The 1 and 5 MeV X-ray simulations were separated into two independent steps. First, the X-ray spectral distributions were generated by simulating the converter; all components in the converter were modeled using the dimensions and materials provided by the manufacturer. Second, the generated X-ray spectra (Figures (a) and (b) of Table 5.1) were used to generate X-ray photons and the absorbed energy in a food sample. This method reduces the calculation time with respect to a one step process of electron-photon tracking.

#### **5.3.4 Dose Distribution Measurement**

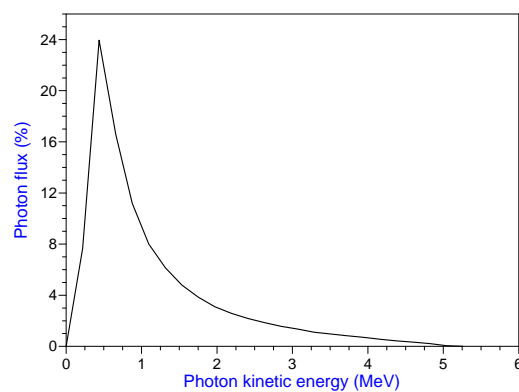
E-beam irradiation experiments were performed using a vertically mounted 10 MeV 18 kW LINAC located at the Texas A&M National Center for Electron Beam Food Research facility. The phantoms were placed on the carrier with the z axis parallel relative to the beam, and the carrier moved under the source at a constant rate (0.3 m/s) to obtain a dose distribution within the target of approximately 1 kGy.

Table 5.1  
Input parameter for the apple simulation

Sample	Radiation source (MeV)	Source description	Voxel dimension (cm)
Wax apple (electron)			
Without Lucite	1.35	Parallel plane source	$0.5 \times 0.07 \times 0.07$
With Lucite	10	Parallel plane source	$0.5 \times 0.07 \times 0.07$
Real apple (X-ray)			
	1	Distributed source*	$0.5 \times 0.07 \times 0.07$
	5	Distributed source*	$0.5 \times 0.07 \times 0.07$



(a)



(b)

\*Calculated photon energy spectrum from the: (a) 1 MeV X-ray converter; (b) 5 MeV X-ray converter.

To measure the dose distribution throughout the whole phantom, we used sheets of GafChromic Dosimetry Media, Type HD-810 (ISP Technologies Inc. of International Specialty Products, Wayne, IL). This radiochromic film (RCF) can be used for dose values below 1 kGy. The apple phantom was cut in half (parallel to  $z$  axis), and the RCF sheets also cut to the same cross-sectional shape (contour) of the half cut plane view of the phantom. The RCF contour was then placed between the two phantom halves. The two halves were then held together by vacuum-packing whole phantom before the irradiation experiment (Kim et al., 2006b).

The GafChromic sheets contain substituted polydiacetylene in gelatin coated on polyester base. The clear film changes to different shades of blue when irradiated. The color change provides a visual indication of dose distribution when irradiated to doses of approximately 1 kGy. To obtain high resolution dose mapping, quantitative measurements of the color change were performed using a flat bed scanner (Microtek® ScanMaker 8700, Carson, CA). The scanner generated the color images that consisted of three components: red, green, and blue (RGB). The scanned images were analyzed using the Image Processing Toolbox of Matlab (MathWorks, Natick, MA) for mapping of the isodoses. A calibration procedure using a Farmer ionization chamber (Nuclear Enterprises, Reading, UK) allowed conversion of the green intensity data to dose values in kGy. Imaging processing was used to convert the digital output to dose profiles (Rivadeneira, 2004).

To reduce the dose distribution within the phantom to below 1.5 kGy, Lucite plastic was used as an attenuation material (Rivadeneira, 2004). The objective of this

experiment was to irradiate the apple phantom to a maximum dose range that was suitable to the RCF and the chemical dosimeter limits. Fig. 5.3 shows the experimental setup where the apple phantoms were placed inside polystyrene boxes between Lucite blocks. The thickness of the Lucite block was 3 cm to produce a target dose of 1 kGy (Rivadeneira, 2004).



Fig. 5.3. Experimental setup for the apple phantom with 3 cm thick Lucite as attenuation material (target dose of 1 kGy). The Lucite material was placed on the top and bottom of the boxes and the phantom between the Lucite blocks.

## 5.4 Results and Discussion

### 5.4.1 Dose Distributions of an Apple Phantom at 10 MeV Electron

Fig. 5.4a illustrates the simulate results of dose distribution in the irradiated phantom using 10 MeV e-beam sources. Note that the dose distribution in the phantom ranged from 1.0 to about 2.8 kGy (Fig. 5.4b). The dose uniformity ratio ( $D_{max}/D_{min}$ ) obtained was 2.8. The high dose at the center of the phantom was a result of energy accumulation because of the dual beam penetration range (larger than the apple vertical length of about 8 cm). Also, electron scattering is absorbed at the right and left side regions at the center resulting in high dose values. At the left and right (Fig. 5.4b), the dose distribution curves overlap each other, showing the same distribution along the  $x$  axis.

In tissue equivalent material, the electron range of 10 MeV electrons is about 5 cm. In the paraffin wax apple, the electrons hit its round-shaped surface, resulting in different depth dose curves with broader and wider dose distribution (Fig. 5.4c).

Fig. 5.5 shows the dose distribution measured with the RCF sheets and simulated with the MCNP5. The RCF contour shows the typical qualitative blue color changes after irradiation (Fig. 5.6a). The high resolution measured dose mapping was obtained by imaging process together with a flat scanner (Fig. 5.6b). The calculated dose distribution in the phantom (Fig. 5.6c) shows good agreement between the experimental and calculated values.

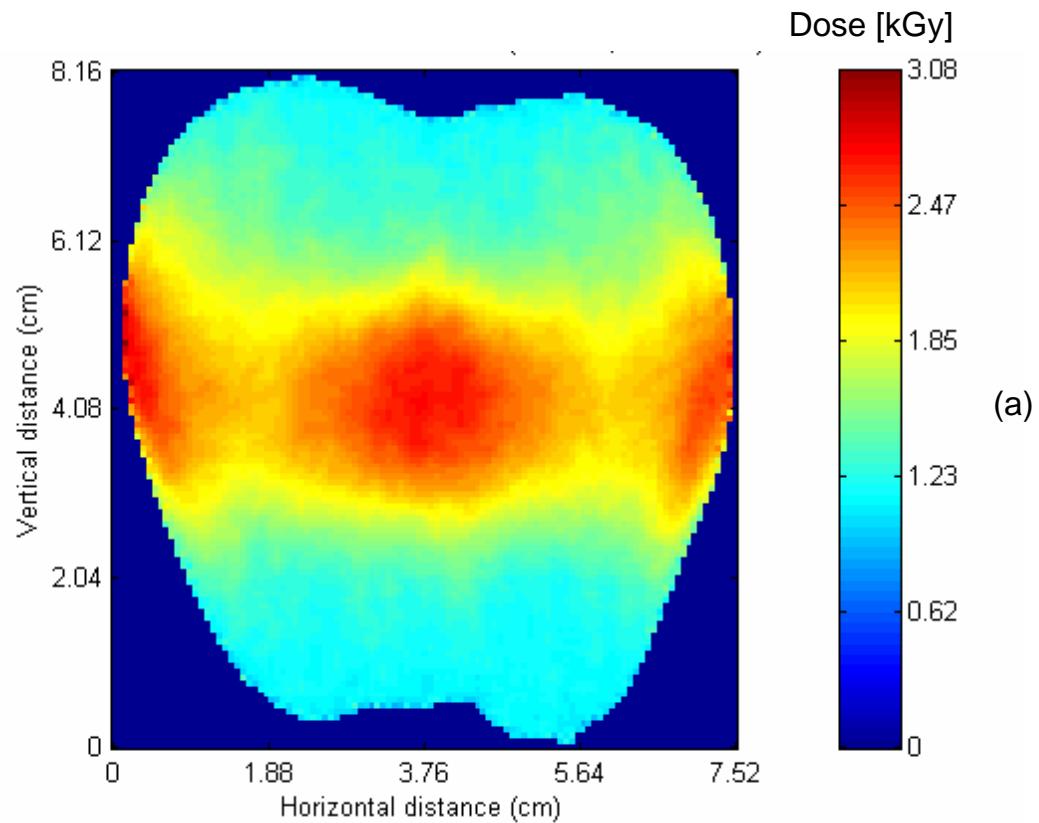


Fig. 5.4. Simulated results of apple phantom with a 10 MeV e-beam source operating in dual mode for a conveyor speed of 0.3 m/s: (a) dose distribution (kGy) over the whole phantom, (b) dose distribution versus penetration depth (at different vertical planes of the phantom); (c) dose distribution versus penetration depth at different horizontal planes (beam source operating in single beam mode -top beam with conveyor speed of 0.3 m/s).

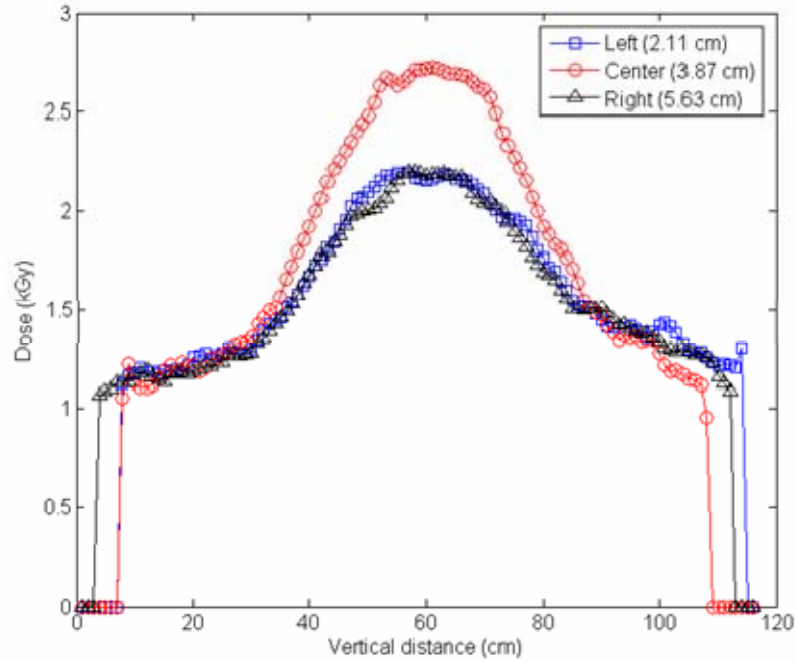
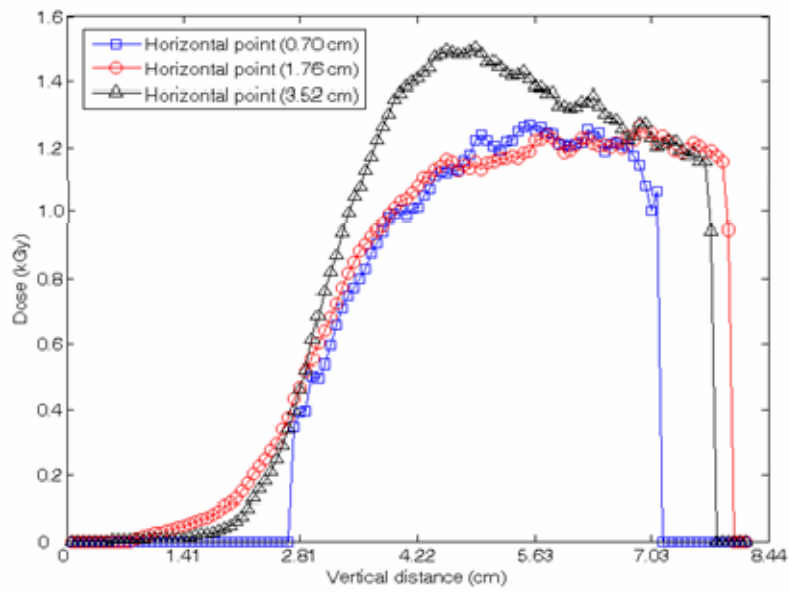
**(b)****(c)**

Fig. 5.4. Continued.

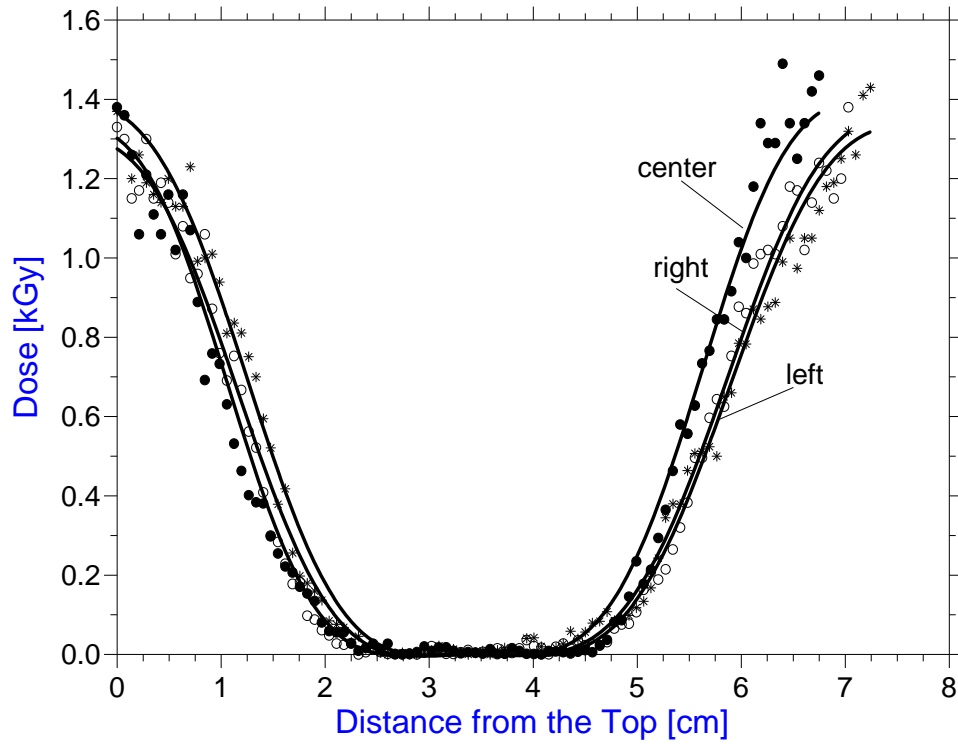


Fig. 5.5. Dose distribution versus penetration depth (at different vertical planes of the phantom) for the phantom apples irradiated with a 10 MeV e-beam source using a 3 cm Lucite shielding material. Continuous lines indicate dose measured (RCF) and dots indicate dose calculated using MCNP5.



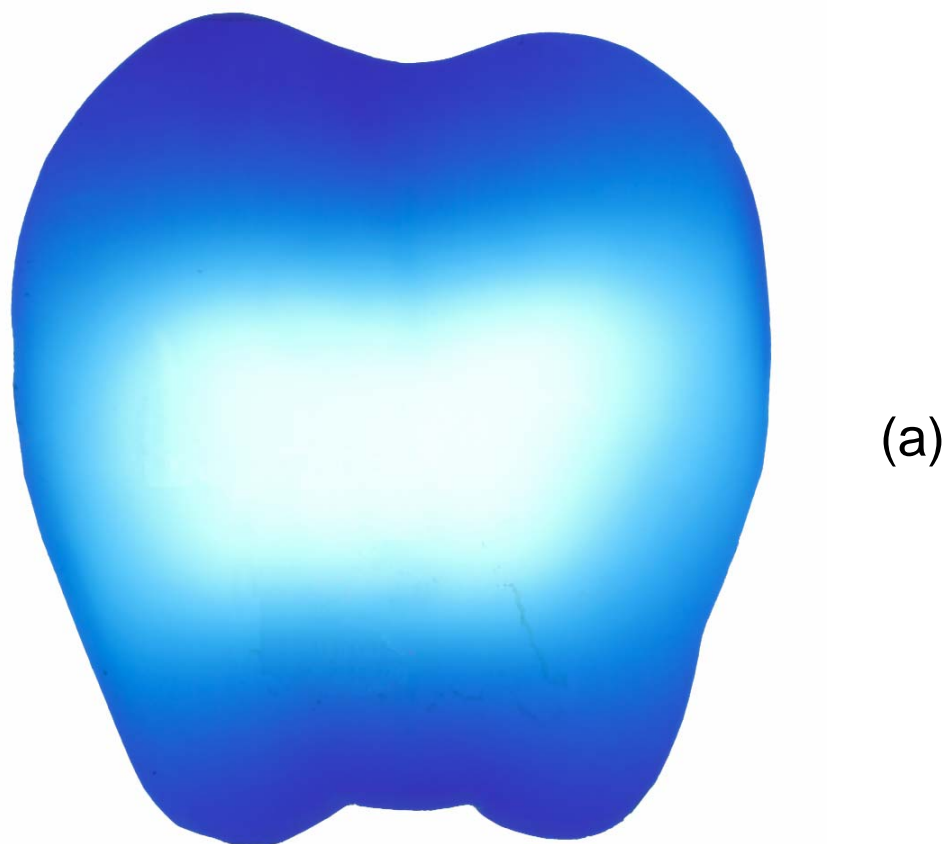


Fig. 5.6. Experimental versus simulated results for the phantom apples irradiated with a 10 MeV e-beam using a 3 cm Lucite shielding material: (a) RCF after irradiation, (b) dose distribution calculation in the RCF using a flat scanner; and (c) simulation dose distribution using MCNP5.

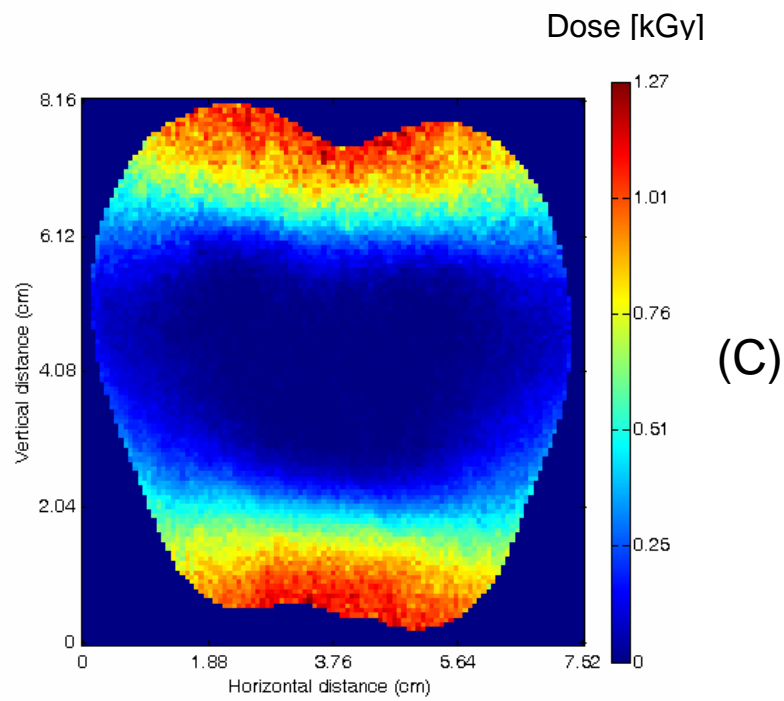
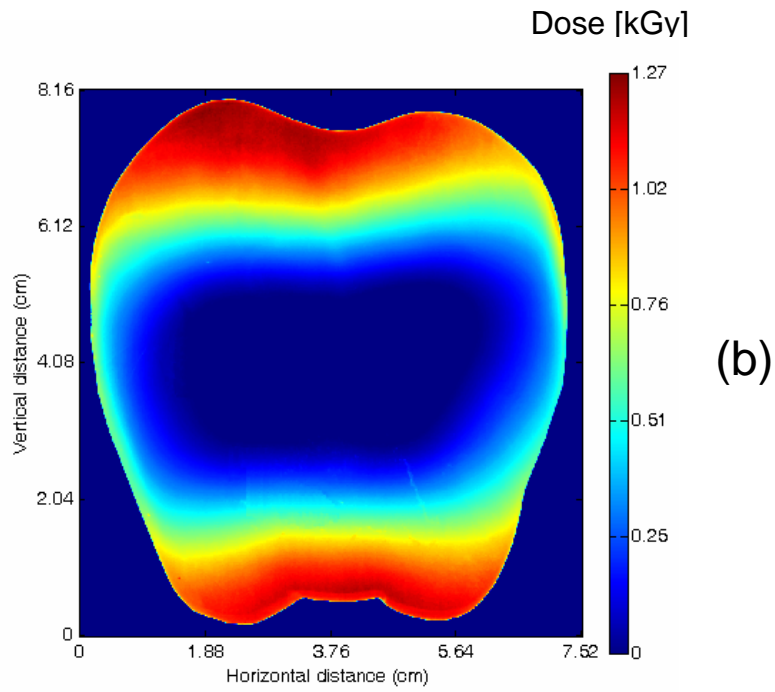


Fig. 5.6. Continued.

Notice that the electrons penetrated quite uniformly from the bottom and the top until they lost all their energy at the center of the apple. The penetration depth in the phantom was about 1.5 cm with the 3-cm Lucite. The top entrance dose at the left and central planes were very close, showing the e-beam uniformity (Fig. 5.6b). The right side ( $x = 6.4$  mm) showed less irradiation (Fig. 5.6b), caused may be by the position of the apple phantom inside the box.

At the bottom of the apple (Fig. 5.6b), the film agrees with the target dose (1 kGy). High dose regions were obtained at the top left and right regions of the apple-phantom. These differences may be due to the positioning of the apple phantom in the box and apple's complex shape. The top left side of the apple-phantom that shows the highest absorbed dose is closer to the Lucite absorber compared to its top right side. As a result, the electrons traveled less before reaching the top left part of the sample, hence depositing more energy. The dose uniformity ratio obtained was about 5.

Fig. 5.6 shows the comparison between simulated and experimental data. The results show a discrepancy of less than 5% between simulation and the measured data. The Monte Carlo code used may be stated to be successfully tested against the experimental data, in terms of its ability to simulate dose distribution from mono-energetic e-beams in a complex shaped, homogeneous apple phantom.

#### **5.4.2 Dose Distribution Simulation of a Real Apple at 1 and 5 MeV X-rays**

The following results illustrate a photon beam interaction simulation in a real apple. At the 5 MeV photon spectra, the average photon energy is 0.7 MeV (Fig. b in

Table 5.1). The same X-ray converter was used to generate 1 MeV photon spectra (Fig. a in Table 5.1). Even though the average energy of 1 MeV photon spectra is 0.3 MeV, its total fluence (particles/area) is as few as 1% of the 5 MeV photon's total fluence.

Assuming the fluencies of both incident charge particles are the same, the maximum doses in the real apple are then 600 and 4 Gy for 5 and 1 MeV photons, respectively.

Fig. 5.7a shows the energy distribution in the apple for 1 MeV photons source. The output results are shown in Table 5.2. The energy was distributed uniformly over the whole apple. The mass attenuation coefficient and mass energy absorption coefficient for 1 MeV photons in an apple are 0.0703 and 0.0308 cm<sup>2</sup>/g, respectively. The average density and horizontal length of the apple were calculated as 0.801 g/cm<sup>3</sup> and 7.90 cm, respectively, from the CT data. Based on the simulation results, the fraction of photons that penetrate the apple without interacting was 64%. The fraction of the incident photon energy (1 MeV) that was transmitted through the apple was 82%, indicating that most of the incident energy escaped from the apple.

The major energy interaction by the 1 MeV photon with an apple is by the Compton effect (i.e., incident photons interacts with loosely bound outer shell electrons) (Attix, 1986). Scattering photons may move in any direction in the apple, including 180° to the direction to the direction of the incident photon (backscattering). In general, low incident photon energy may produce scattering photons in backward directions. The average recoil electron energy was 0.44 MeV for 1 MeV photons incident in the apple (Table 5.2). The average scattering angle of the photon was 85°, shown that the photon almost spread in the radial direction. Note that the energy deposition is shown rising

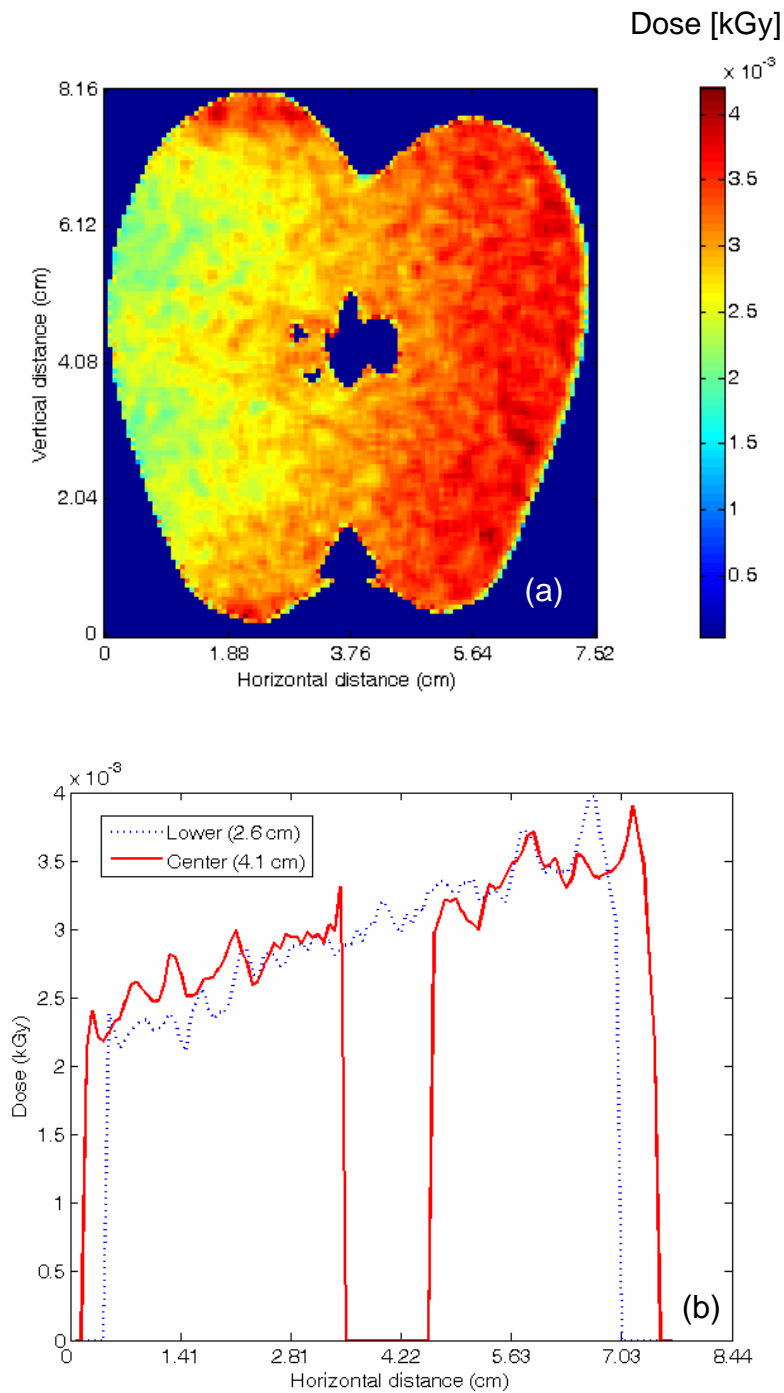


Fig. 5.7. Dose distribution (kGy) in an actual apple using: (a) 1 MeV photons and (b) at the vertical planes (2.6 cm and 4.1 cm); (c) 5 MeV photons and (d) at the vertical planes (2.6 cm and 4.1 cm).

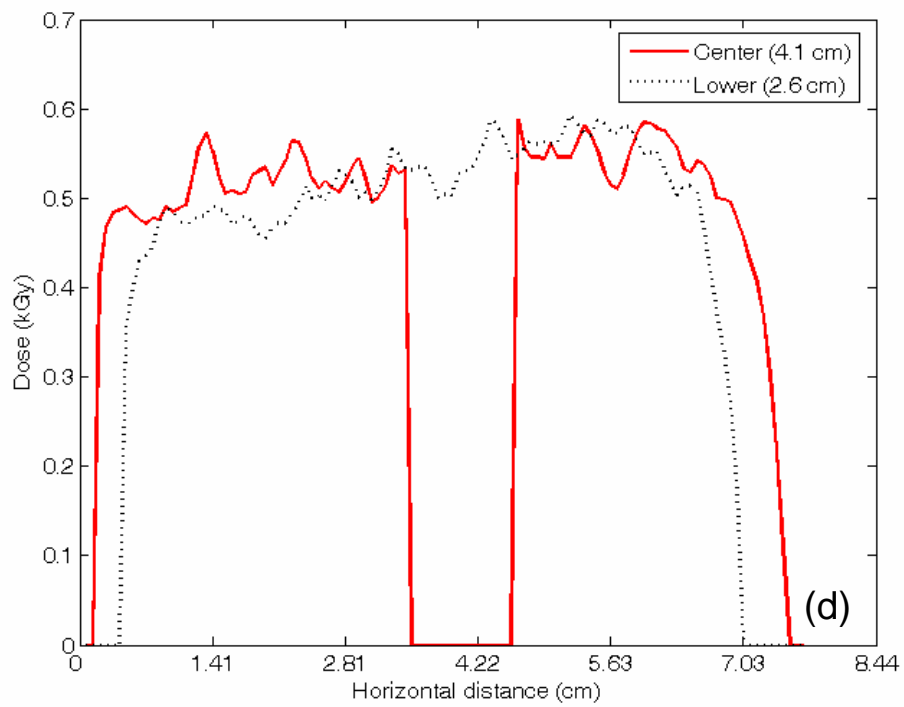
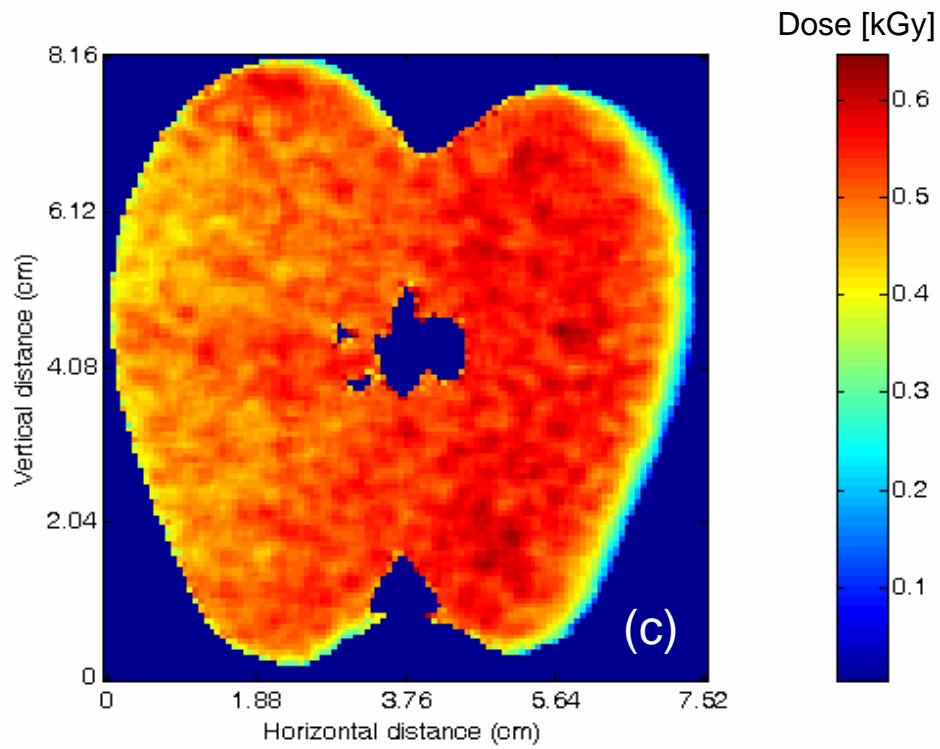


Fig. 5.7. Continued.

Table 5.2  
Output properties obtained by simulation of a real apple irradiated by 1 and 5 MeV X-rays

Output properties	Photon energy (MeV)	
	1	5
Mass attenuation coefficient (cm <sup>2</sup> /g)	0.0703	0.0302
Mass energy-absorption coefficient (cm <sup>2</sup> /g)	0.0308	0.0191
Fraction of photons penetrated & not interacted (%)	64	79
Fraction of energy transmitted through (%)	82	88
Average recoil-electron energy (MeV)	0.44	3
Average scattering angle of photon (deg)	85	34
D <sub>max</sub> /D <sub>min</sub> *	2	1.5

\* Dose uniformity ratio

with increasing depth, and the energy distribution is scattered more uniformly (Fig. 5.7a). The dose uniformity ratio obtained in this case was 2.

Fig. 5.7c shows the energy deposition with an apple when a higher energy source is used (5 MeV photons). As for 1 MeV source, the photon energy was deposited over the whole apple. In general, how far a given photon will penetrate depends on the specific medium traversed and on the photon energy. Note the dose buildup effect at the surface of the apple. This phenomenon results from the combination of the density change at the interface and geometric factors, involving both photon beam dimensions and electron scattering (Attix, 1986). The mass attenuation coefficient and mass energy absorption coefficient for 5 MeV photons in the apple were 0.0302 and 0.0191 cm<sup>2</sup>/g, respectively (Table 5.2). The fraction of photons that penetrate the apple without interacting was 79% (higher than that for 1 MeV photons). The fraction of the incident photon energy that was transmitted by the apple was 88%, showing that most of the incident energy escaped from the apple just like the results obtained for the 5 MeV photons. However, the 1 MeV source produced more interactions and gave up more energy to the apple than the 5 MeV source. The dose uniformity ratio for the 5 MeV source was 1.5, i.e., the dose was more uniformly distributed in comparison with the 1 MeV source.

As for the case of 1 MeV energy source, the major interaction of energy deposition for the 5 MeV photons in an apple is also by the Compton effect. The average recoil electron energy was 3 MeV for 5 MeV photons in an apple (Table 5.2). The scattering angle of the photon was 34°, indicating that the photon tended to move



forward. Fig. 5.7c shows that the energy deposition rises with increasing depth near the surface as the population of charged particles flowing toward the left is increased by more photon interactions.

Fig. 5.7b shows the dose distributions in an apple, irradiated with a 1 MeV X-ray source, between the vertical points 2.6 and 4.1 cm along the horizontal direction. The absorbed energy increases rapidly until a maximum energy is reached, and then it decreased because of attenuation characteristic of the ionization irradiation. The vertical center of the apple (4.1 cm) shows very low energy located between the horizontal points of 3.5 and 4.6 cm (air space). The density of air is so low that almost no energy is lost as the X-ray photons traverse that region.

Similar results are shown for the dose distribution in the apple for 5 MeV X-ray sources (Fig. 5.7d). The ratios of the exit dose to the entrance dose are 0.64 and 0.85 for 1 and 5 MeV X-ray sources, respectively. At the apple phantom irradiation experiment with 5 MeV X-ray (vertical beam direction), the ratio of the exit dose to the entrance dose was 0.65 (Rivadeneira, 2004). This ratio is lower than the value (0.85) at a real apple simulation with 5 MeV X-ray, because the penetration depth of the former (apple's height) is longer than the latter (apple's diameter); Golden Delicious apple is conic shape, which is tapered to the apex. It showed, at X-ray treatment of an apple, that the lateral beam direction is better for uniform dose distribution.

## 5.5 Conclusion

In this study, we used Monte Carlo simulation with CT scan technology to predict dose distribution in an irregular shaped food product, an apple.

For a Lucite thickness of 3 cm (target dose of 1.0 kGy), the RCF film confirmed a very uniform irradiation treatment at the top and bottom regions with a maximum dose of 1.3 kGy located at the top left region of the apple. This simulated results predicted very well that dose distribution (5% discrepancy) measure in the apple phantom. The Monte Carlo code used was successfully tested against the experimental data, in terms of its ability to simulate dose distribution from mono-energetic e-beams in a complex shaped, homogeneous apple phantom.

The geometric and composition CT data of a real apple was generated then, by using the Monte Carlo code to simulate the dose distribution in an apple irradiated by 1 and 5 MeV photon beams. The energy was distributed over the whole apple for both energy levels. For the 5 MeV photon simulations, a lesser amount of energy was deposited closer to the surface (at the right side surface) of the apple. This was because of the scattered photon's forward direction and high energy of recoil electrons. It also shows a more uniform in the forward direction.

For 1 MeV simulation, a higher energy was distributed at the right half of the apple, and there was no warming-up region as shown in the 5 MeV simulation. These results reflected the fact of the higher scattering angle of the photons and the lower energy of the recoil electrons.

## CHAPTER VI

### 3-D DOSE DISTRIBUTIONS FOR OPTIMUM RADIATION TREATMENT

#### PLANNING OF COMPLEX FOODS\*

##### 6.1 Overview

To obtain satisfactory e-beam irradiation of fresh products a strict process control is required to ensure that the dose delivered to all parts of the treated product falls within some specified range. As a basis of a dosimetry technique, assessment of the exact geometry of fresh products in a 3-D configuration is needed. Obtaining a uniform dose in inherently complex foods such as a chicken carcass is, however, difficult. The objective of this study was to obtain detailed, high-resolution dose distributions of a chicken carcass exposed to e-beam or X-ray irradiation using Monte Carlo simulation and Computer Tomography (CT) techniques.

We obtained multi-sliced CT data of a frozen chicken carcass to extract exact product geometry and densities using image-processing methods. The type of source energy input spectrum and source size were entered into the Monte Carlo N-Particle radiation transport code (MNCP5) to obtain dose distributions in the product. For low energy treatment (1.35 MeV electrons, Van de Graaff accelerator), dose absorption occurred up to 5-7 mm deep, resulting in surface irradiation of the carcass. For high

---

\* Reprinted with permission from “3-D dose distributions for optimum radiation treatment planning of complex foods” by Kim, J., Moreira, R. G., Huang, Y., & Castell-Perez, M. E. (2007). *Journal of Food Engineering*, 79, 312-321. Copyright 2006 by Elsevier Ltd. doi:10.1016/j.jfoodeng.2006.01.061

energy treatment (10 MeV, LINAC, bottom only), the doses within the carcass rose up to 1.2 times the incident dose with increasing depth and rapidly fell to low values. Two-sided (top and bottom) irradiation resulted in a dose uniformity ratio ( $D_{max}/D_{min}$ ) of about 1.6. Two-sided X-ray irradiation significantly improved the uniformity ratio from 2.5 to 1.8.

## 6.2 Introduction

Food irradiation is an important technique for the treatment of foods that may be contaminated with pathogenic microorganisms. If applied properly, irradiation can be an effective way to reduce the incidence of foodborne disease and treat a variety of potential problems in our food supply, including bioterrorism (Morehouse, 2002).

The use and importance of precise irradiation in food safety have increased greatly over recent decades. A key advance had been the development of more efficient e-beam linear accelerators whose goal is to deliver dose distributions that are uniform all over the material using high dose rates. These techniques include 5, 7.5, and 10 MeV e-beam sources and 5 MeV X-ray machines, which have high penetration capabilities.

However, there is a multitude of product and package configurations whose suitability for processing using irradiation requires evaluation. Many of these are highly non-homogeneous with respect to their three-dimensional (3-D) mass distribution, as for example poultry carcasses, a packaged ready-to-eat meal, a head of broccoli, leafy vegetables such as lettuce and vegetable sprout (alfalfa, clover, and radish). Satisfactory irradiation of these food items requires strict process control to ensure that the dose

delivered to all parts of the treated product falls within some specified range. Hence it is necessary to assess the ability of a given irradiation system to deliver the required dose to the products and packages intended for treatment. This requires a more stringent quality assurance (QA) of the treatment planning and delivery.

A combination of the 3-D geometries with Monte Carlo technique can be used to simulate (Andreo, 1991) electron beam irradiation of food products (Brescia et al., 2003). Based on the simulation accurate dose maps for any product can be generated (Kim et al., 2006b).

The objectives of this study were: (1) to develop a methodology to build a 3-D geometric models of complex shaped food products, such as an apple using Computed Tomography (CT) techniques; (2) use the technique developed in (1) to obtain detailed, high resolution dose distributions of a frozen chicken carcass (a complex shaped and heterogeneous product) exposed to e-beam or X-ray irradiation using Monte Carlo simulation.

### **6.3 Materials and Methods**

First, we developed a methodology to build 3-D geometric models using multi-sliced CT data of complex shaped food products, like an apple. Then, we used the developed methodology to extract product geometry and densities using image-processing methods of a frozen chicken carcass (Tyson- Premium Rock Cornish Game Hen – 0.624 kg), which besides being complex shaped its composition is heterogeneous.

The source energy input spectrum and source size were entered into the Monte Carlo N-Particle radiation transport code (MCNP5) to obtain dose distributions in the product.

### 6.3.1 CT Data Acquisition

A HD-350E X-Ray CT Scanner (Universal Systems, Solon, Ohio) located at the Department of Petroleum Engineering of Texas A&M University was used to scan food products. CT scan is a diagnostic test that combines the X-ray with computed technology. A series of X-ray beams from different angles are used to create cross sectional images of the target. This technique has been widely used in the medical field for dosimetry planning and analysis in radiotherapy (DeMarco et al., 1998; Yoriyaz et al., 2000). When food samples are scanned by a CT scanner, multi-sliced CT data are obtained and each pixel on the slice image is assigned a numerical value, e.g., fat ranges from  $-200$  to  $-5$ , water from  $-5$  to  $5$ , which is related to the densities of scanned materials (food composition). In general, the values of each pixel in the CT slices are related to density as:

$$\rho = 1 + \frac{CT}{1000} \quad (6.1)$$

where  $\rho$  = density [g/ml] and CT = CT values (Fig. 6.1).

Based on the CT data, geometries of food samples can be constructed through image processing algorithms.

### 6.3.2 CT Data Visualization

The VoxelCalc Plus (KehlCo, Inc., Houston, Texas) software was used to visualize the CT slices and convert them into 24-bit 3-band (RGB) bitmap images.

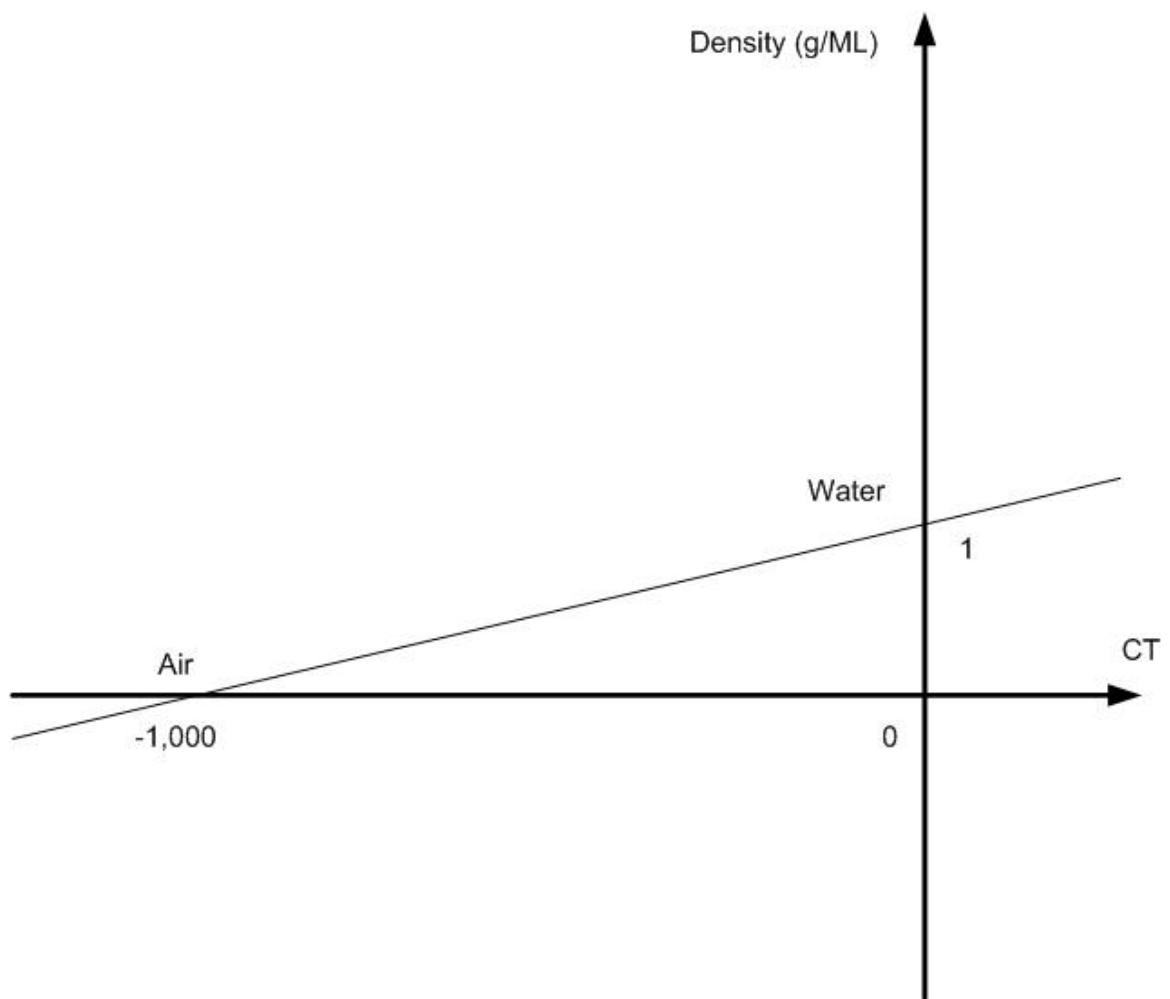


Fig. 6.1. Relationship between CT values and material densities.

### 6.3.3 CT Data Processing

Matlab Image Processing Toolbox (MathWorks, Natick, Massachusetts) was used to make the image deck of the original and processed CT slices. The artifacts on the original CT slices, such as sample holder, was removed and cropped to fit the region of interest (ROI). Inside the ROI, the target product was then segmented out from the background.

In Matlab, loading the CT data constitutes two variables to the workspace:  $X$  ( $r$ -by- $c$ -by- $n$ , class unit 8) and a grayscale colormap,  $map$  ( $N$ -by-3, class double). The variable  $r$  is the number of rows of each slice,  $c$  is the number of columns of each slice,  $n$  is the number of slices, and  $N$  is the quantization of index scales of each slice. For example, an apple scanned by the CT machine produced fourteen 512 by 512 slices with a  $256 \times 3$  colormap. With Matlab, these slices can be loaded into a four-dimensional ( $512 \times 512 \times 1 \times 14$ ) array  $X$ , where the third dimension represents the index channel which works together with colormap to generate color images.

The image decks were generated by the Matlab command *montage*( $X, map$ ) to show the CT slices in one sheet. Fig. 6.2a shows the original image deck of CT slices of an apple.

Artifacts on the slices have to be removed to have clean images. As shown in Fig. 6.2b, the major artifacts are the half circle sample holder, paper towels, and adhesive tapes around the samples. The artifacts can be removed with masked filtering in Matlab. It is easy to remove the signatures of the paper and the tapes because their



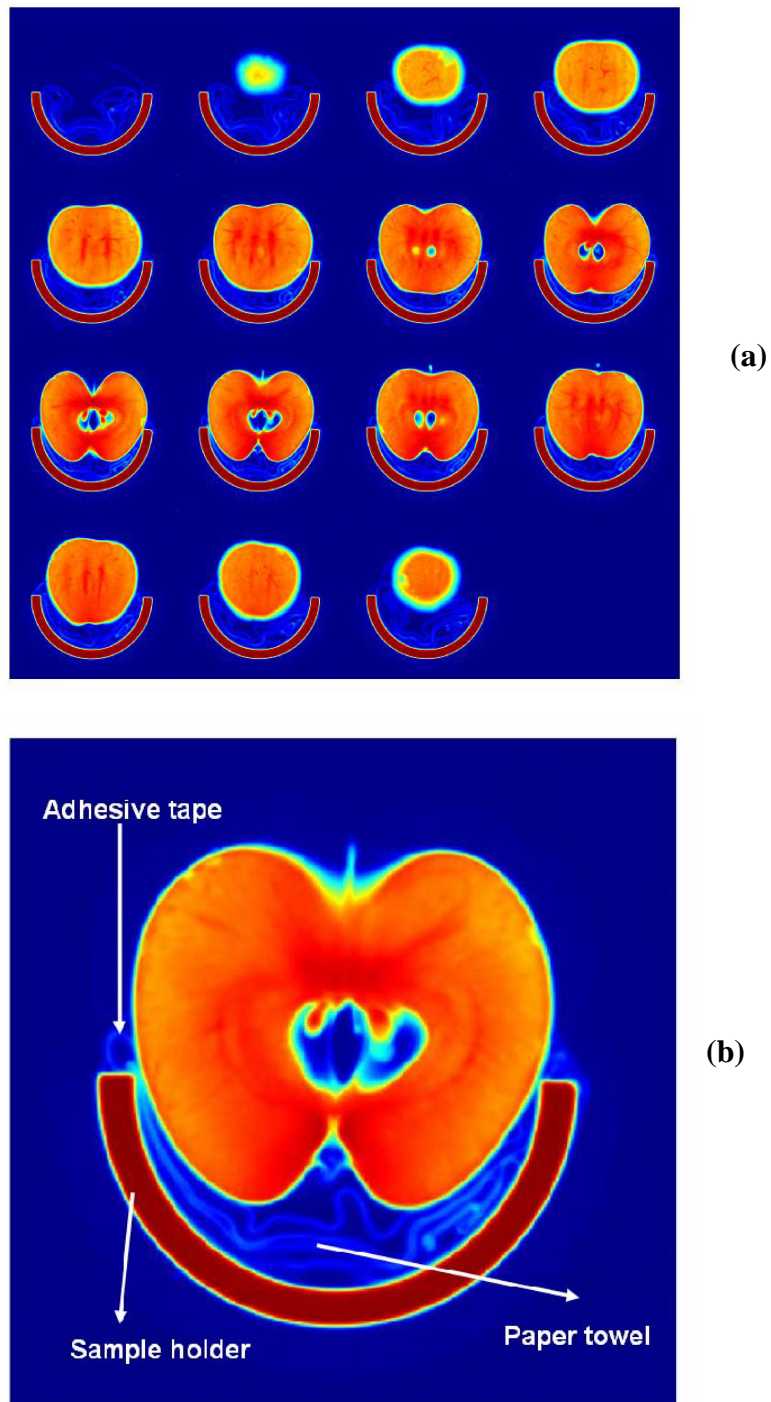


Fig. 6.2. (a) Original CT slice deck of an apple: (b) Artifacts (paper towel, adhesive tape, and sample holder) showing in one of the CT slices of apple.

index values are relatively low. The mask image can be generated by the Matlab command  $mask = (X(:,:,1,k) < Z)$  where  $k = 1$  and  $Z = 80$  for example. Then, the paper towel and tape adhesive artifacts can be removed from all of the slices with Matlab as

```

...
if mask (i,j) == 0
    X(i,j,1,k) = 0;
End
...

```

It is more difficult to remove the sample holder from the slices. To remove it, its position on the slices has to be determined. There are two ways to perform this task in Matlab. One way is to generate a mask in the opposite direction assuming the holder has significantly high index values with high density. So, we selected a slice in which the holder is much brighter than the target product. The mask can be generated by the Matlab command  $mask = (X(:,:,1,k) > Z)$  where  $k = 1$  and  $Z = 200$  for example. Next, the sample holder can be removed from all of the slices with the Matlab if-end code.

Another way is to generate a mask by defining a polygon that encloses the holder.

Next, image cropping is required to eliminate the blank areas remaining after removal of the artifacts. A region of interest (ROI) is then defined so that the images are focused on the target. This operation will reduce the size of the image slices and make further manipulation easier. The operation of cropping can be done on the slices by the

Matlab command *imcrop(X(:,:,l,k),[x,y,dx,dy])* where  $(x,y)$  is the cropped image origin at the upper-left corner and  $dx$  and  $dy$  are the width and height of the cropped images, respectively.

Fig. 6.3a shows the ROI of the CT image of the apple after artifact removal and image cropping have been performed. Fig. 6.3b shows the image deck of all CT slices of the apple with artifact removal and image cropping. With Matlab, the artifact removal and image cropping can be implemented simultaneously and automatically.

Image segmentation is a useful operation in image processing to separate the desired features from the background. As shown in Fig. 6.3a and b, the shape of the apple and its components (skin, flesh, and core) have been separated from the artifacts and blank background on the ROIs of the CT slices. The apple has been segmented out slice by slice.

#### 6.3.4 3-D Geometric Reconstruction

With the processed CT slices the 3-D geometrical shape of the imaged subject can be reconstructed using the following code:

```
D = squeeze(X);
Ds = smooth3(D);
Hiso = patch(isosurface(Ds), 'FaceColor', [1,0.25,0.25], 'EdgeColor', 'none');
Hcap = patch(isocaps(D,3), 'FaceColor', 'interp', 'EdgeColor', 'none');
colormap(map);
```

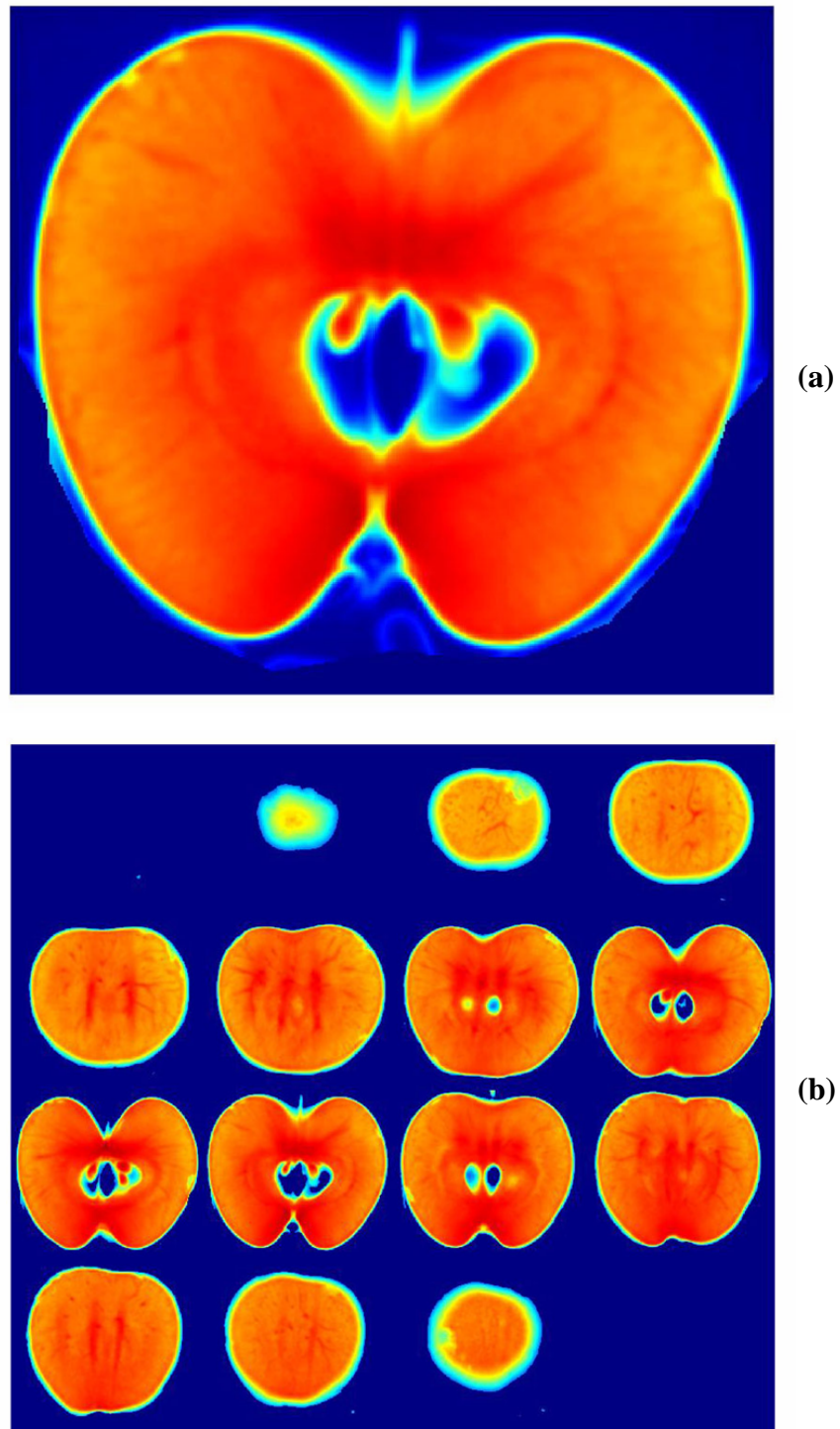


Fig. 6.3. (a) The ROI of the CT slice of apple; (b) Processed CT slice deck of the apple.

Fig. 6.4a shows the reconstructed apple with the CT slices using the above Matlab code. This 3-D reconstruction can be rotated to allow viewing of the reconstruction from all different angles.

With the processed CT slices the 3-D subsets of the geometrical shape can also be reconstructed. This subvolume reconstruction can be performed with the following Matlab code (Fig. 6.4b).

```
D = squeeze(X);
[x y z Dq] = subvolume(D, [150 250 nan 200 nan nan]);
p = patch(isosurface(x,y,z,Dq), 'FaceColor', [1,0.25,0.25], 'EdgeColor',
'none');
p2 = patch(isocaps(x,y,z,Dq,3), 'FaceColor', 'interp', 'EdgeColor', 'none');
colormap(map);
```

### 6.3.5 Monte Carlo Simulation

The MCNP-5 (Monte Carlo N-Particle- Version 5) used in this study was developed at the Los Alamos National Laboratory (Radiation Safety Information Computational Center (RSICC), Oak Ridge National Laboratory, Oak Ridge, TN). This code is capable of simulating coupled electron-photon problems using a three-dimensional combinatory geometry system. The simulator was run in a parallel computer platform (Dell™ PowerEdge™ 6650, 4 CPU) located at the Department of Biological and Agricultural Engineering at Texas A&M University.

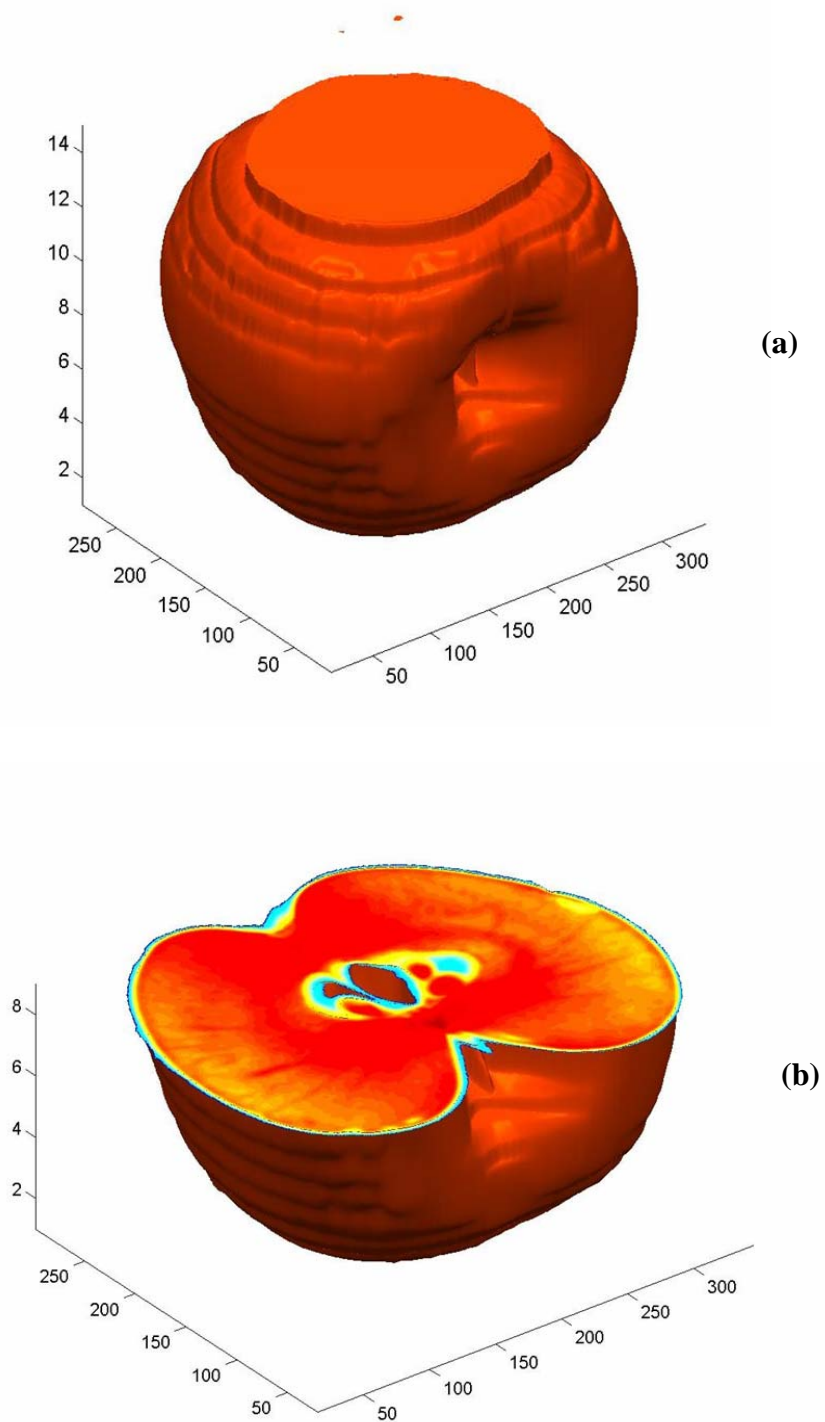


Fig. 6.4. (a) 3-D reconstruction of the apple with the CT slices; (b) 3-D subvolume reconstruction of the apple with the CT slices.

In this study, we simulated the pasteurization treatment of a frozen chicken carcass with a 1.35-MeV e-beam Van de Graaff accelerator (low-energy) and a 10-MeV (high-energy) e-beam linear accelerator (LINAC) (Fig. 6.5). The e-beam source was described as a parallel plane large enough to cover the target, and the electrons were emitted in a plane and distributed evenly within the scan.

For electron irradiations, two vertically mounted and opposing 10 MeV, 18 kW LINAC are used to accelerate electrons to near the speed of light using microwaves so they can be targeted into a food product. The electron LINAC can operate in single or dual beam mode so food products receive radiant energy from one or both the upper and lower accelerators so that product flipping is not required. For X-ray irradiation, a single horizontally mounted 5 MeV, 15 kW X-ray Linear Accelerator produces electrons traveling near the speed of light hitting a dense metal target so X-rays are produced.

The 5 MeV X-ray simulations were separated into two independent steps. First, the X-ray spectral distributions were generated by simulating the converter; all components in the converter were modeled using the dimensions and materials provided by the manufacturer. Second, the generated X-ray spectra (Fig. 6.6) were used to generate X-ray photons and the absorbed energy in a food sample. This method reduces the calculation time with respect to a one-step process of electron-photon tracking. The entrance dose at all simulations was 1 kGy.

Generally, Monte Carlo simulation results represent an average of the contribution from many histories sampled during the course of the problem (Brown,

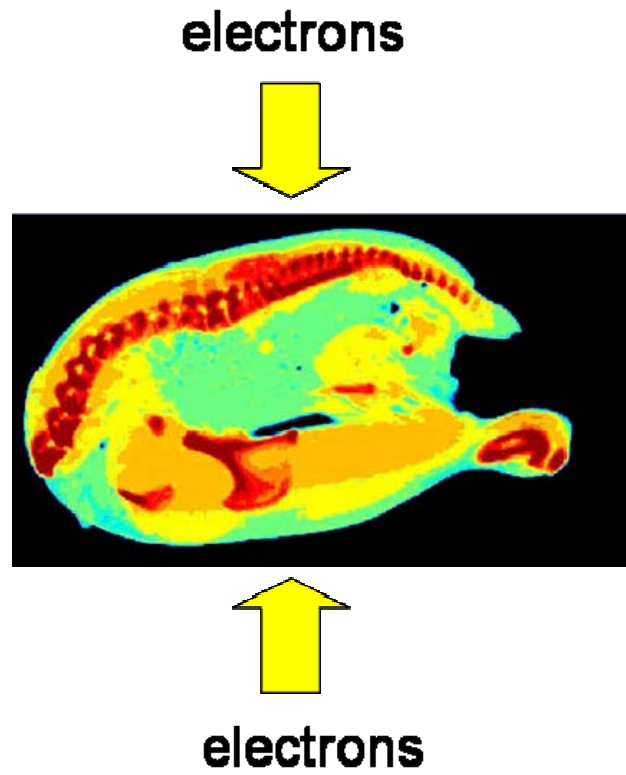


Fig. 6.5. Electron beam directions in a chicken carcass for simulation of dose distribution using low (1.35 MeV) and high (10 MeV) energy e-beam source.



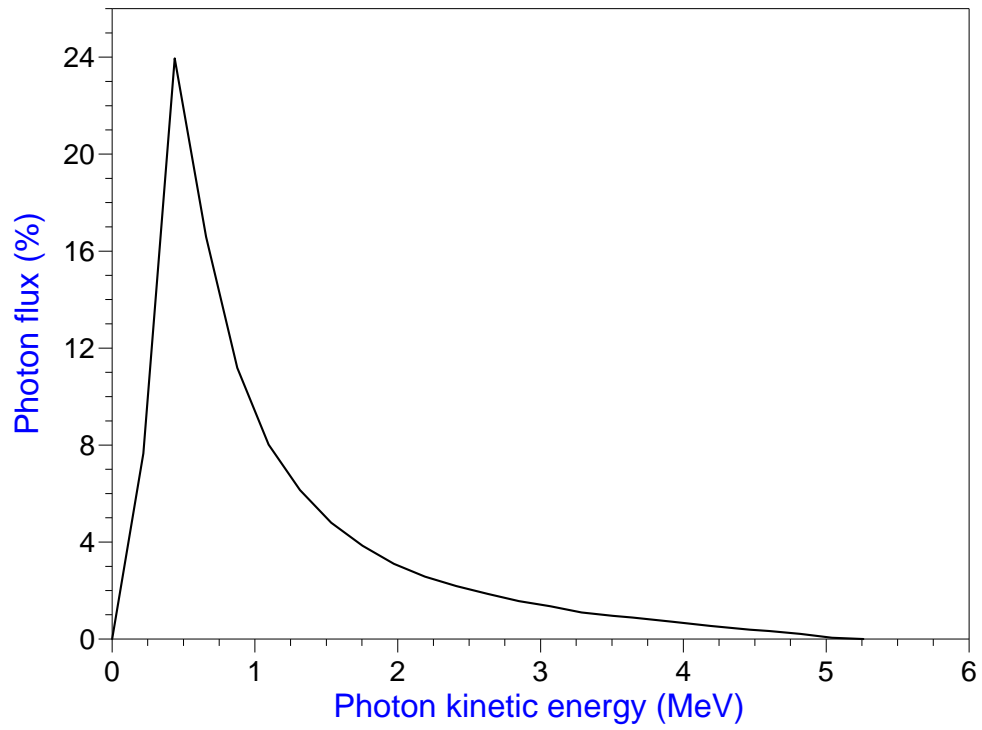


Fig. 6.6. Calculated X-ray spectra from the 5 MeV X-ray converter.

2003). Therefore, a total of  $10^6 - 10^7$  histories were used in our simulation to reduce the statistical uncertainty to about 5% or less.

Tables 6.1 and 6.2 show the input parameters and the product compositions used to simulate the dose distribution in the chicken carcass irradiated using e-beam and X-rays.

### **6.3.6 Dose Distribution Measurement**

Electron-beam irradiation experiments were performed using a vertically mounted 10-MeV 19 kW linear accelerator located at the Texas A&M National Center for Electron Beam Food Research facility. The whole frozen chicken samples were placed inside open cardboard boxes ( $0.508 \text{ m} \times 0.609 \text{ m} \times 0.102 \text{ m}$ ) and then on a carrier moving under the e-beam source at a constant rate (0.2 m/s) to obtain a dose distribution at the surface of the target of approximately 1 kGy.

To determine the applied dose, 10 dosimeters (B3WIN Radiochromic Films, Gex Corporation, Centennial, CO, USA) were placed evenly at the surface of the chicken: five on the top (T) and five in the back (B) of the product. In addition, six more dosimeters were placed inside of the chicken.

## **6.4 Results**

### **6.4.1 3-D Reconstruction of Food Products Using CT Scan Data**

The purpose of CT scans of food product is to capture feature of components and geometric shape. Through the investigation of 3-D reconstruction procedure, we found

Table 6.1  
Input parameters for chicken carcass simulation

<b>Radiation source</b>	<b>Source description</b>	<b>Voxel dimension</b>
1.35 MeV electron	parallel plane source	0.5 cm x 0.14 cm x 0.14 cm
10 MeV electron	parallel plane source	0.5 cm x 0.14 cm x 0.14 cm
5 MeV X-ray	distributed source	0.5 cm x 0.14 cm x 0.14 cm

Table 6.2  
Material composition (%/weight)

	<b>C</b>	<b>H</b>	<b>O</b>	<b>N</b>	<b>Others</b>
Meat and skin <sup>a</sup>	21.18	10.32	64.70	2.96	0.03Ca, 0.05Mg, 0.33P, 0.43K
Bone <sup>b</sup>	27.80	6.40	41.00	2.70	0.20Mg, 7.00P, 0.20S, 14.70Ca

<sup>a</sup> source: USDA National Nutrient Database for Standard Reference (Chicken, broilers or fryers, meat and skin, raw; NDB NO: 05006).

<sup>b</sup> source: NIST ESTAR Database Program  
(<http://physics.nist.gov/PhysRefData/Star/Text/ESTAR.html>)

that feature capturing is sensitive to the direction of CT scan, especially for those irregularly shaped products. Basically, 3-D reconstruction was performed along the transverse CT slices. However it has limitation; the reconstructed image along the transverse direction is very rough, because CT slice spacing is much larger than the resolution of the slice images ( $r \times c$ ). A complex mathematical method is needed to make that smooth. Therefore, a well-planned scan direction is a crucial factor in capturing content and geometric features of a food product. Fig. 6.7 shows the 3-D reconstruction of a broccoli (a) and a chicken carcass (b) using the developed procedure. It also shows that our methodology is an effective tool in capturing the shape of those complex-shaped products. Based on the density data, the internal composition of those two products can be visualized as shown in Fig. 6.8.

#### **6.4.2 Dose Comparison of Chicken Carcass between Simulated and Experimental Data**

Fig. 6.9 shows the comparison between simulated and experimental data. The results show a discrepancy of less than 5% between simulation and the measured data. The Monte Carlo code used may be stated to be successfully tested against the experimental data, in terms of its ability to simulate dose distribution from monoenergetic electron beams in a complex shaped, inhomogeneous target such as a chicken carcass.

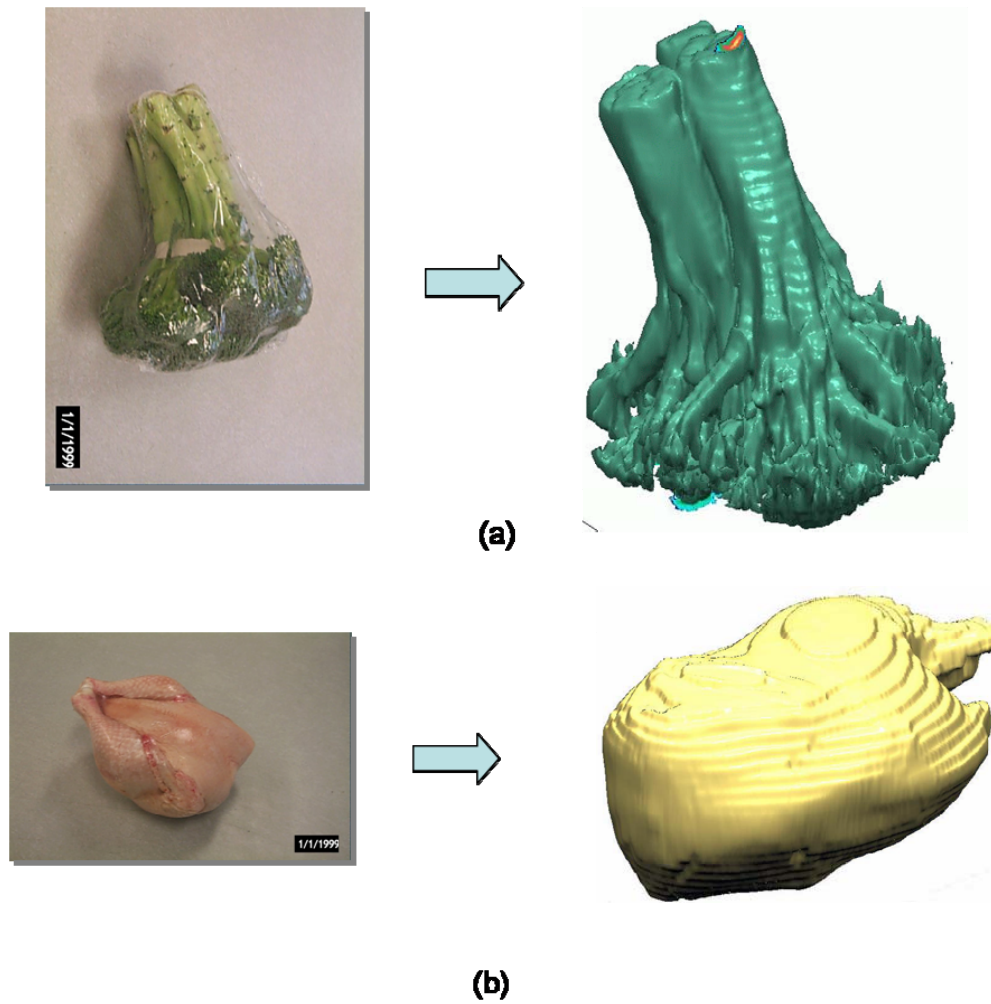


Fig. 6.7. 3-D reconstruction of CT images using Matlab, (a) a broccoli, (b) a whole chicken.

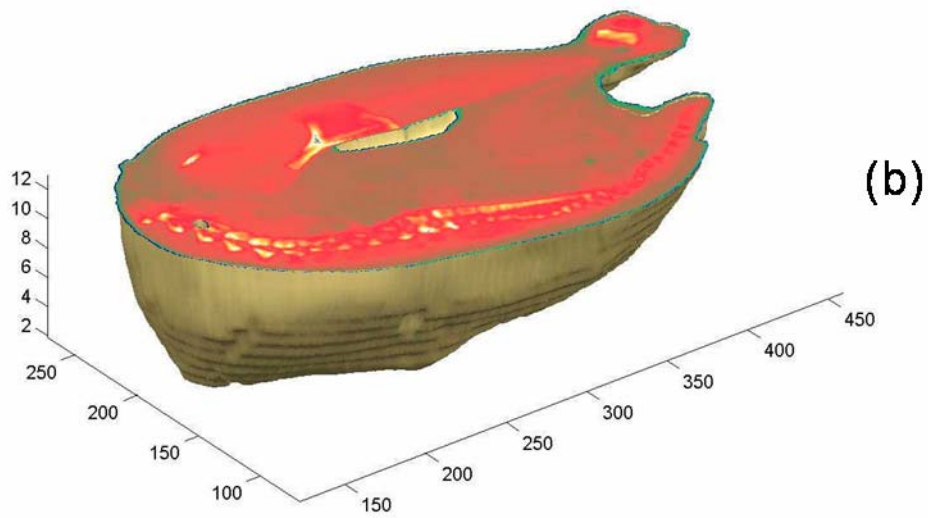
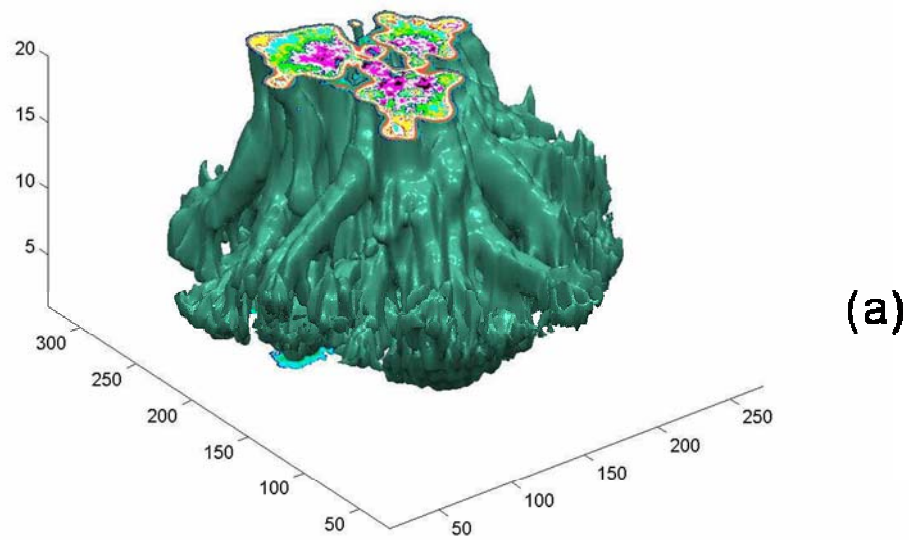


Fig. 6.8. 3-D reconstruction of CT images using Matlab showing internal composition, (a) a broccoli, (b) a whole chicken.

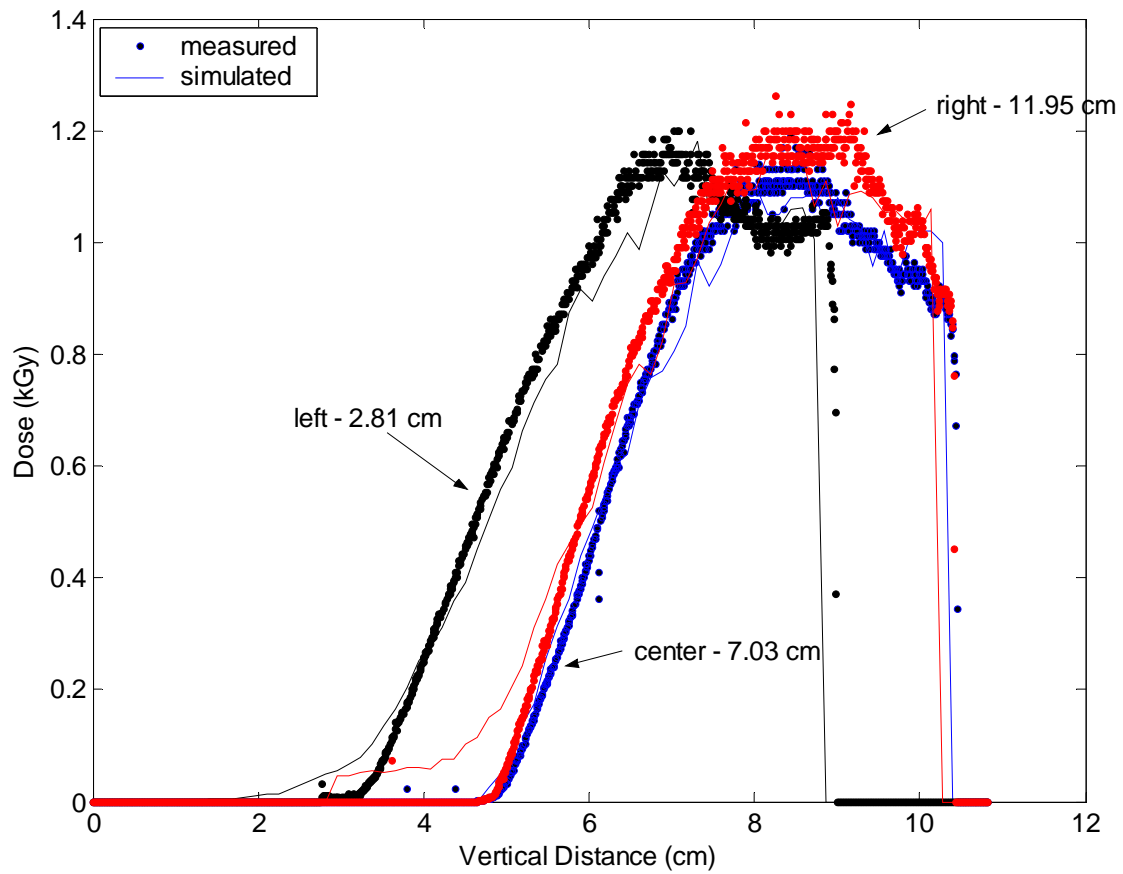


Fig. 6.9. Dose comparison between measured and simulated data in a whole chicken irradiated with a 10 MeV e-beam accelerator from an upper beam direction. Dose values evaluated at the horizontal points of 2.81 cm, 7.03cm, and 11.95 cm.

#### **6.4.3 Dose Distribution Simulations of Chicken Carcass at 1.35 MeV Electrons**

Fig. 6.10 shows the simulation results of dose distributions in a chicken carcass irradiated with a 1.35 MeV e-beam accelerator. The penetration depth was around 5-7 mm, resulting only in surface irradiation of the target.

Using either the top (Fig. 6.10a) or the bottom beam (Fig. 6.10b) was not sufficient to irradiate the whole chicken. When both beams were used (Fig. 6.10c), the whole surface of the chicken was exposed to irradiation. The maximum dose of 1.6 kGy was detected (Fig. 6.10d) at half way of the total penetration depth. A few millimeters into the chicken, the dose is highest. This is mainly due to a buildup of lower energy electrons, which increase the absorbed dose. At the surface, there was no buildup of low energy electrons, though some of the electrons were scattered away.

#### **6.4.4 Dose Distribution Simulations of Chicken Carcass at 10 MeV Electrons**

Fig. 6.11 presents the dose distribution simulation when irradiating the chicken carcass with a 10-MeV accelerator. Using only the top beam (Fig. 6.11a) resulted in a penetration depth of 5-7 cm, so only half of the carcass was irradiated. Note that the dose values around the bones of the chicken (see CT scan of Fig. 6.5) were higher than in the muscle or breast areas. This is expected since bone has a higher density and tends to shield the irradiation energy. The dose within the product rose up to 1.2 kGy (Fig. 6.11d) with increased depth and then decreased exponentially to low values.

Same results were obtained when only the bottom beam (Fig. 6.11b) was used to irradiate the product. Here we also can see the higher dose values around the bones.



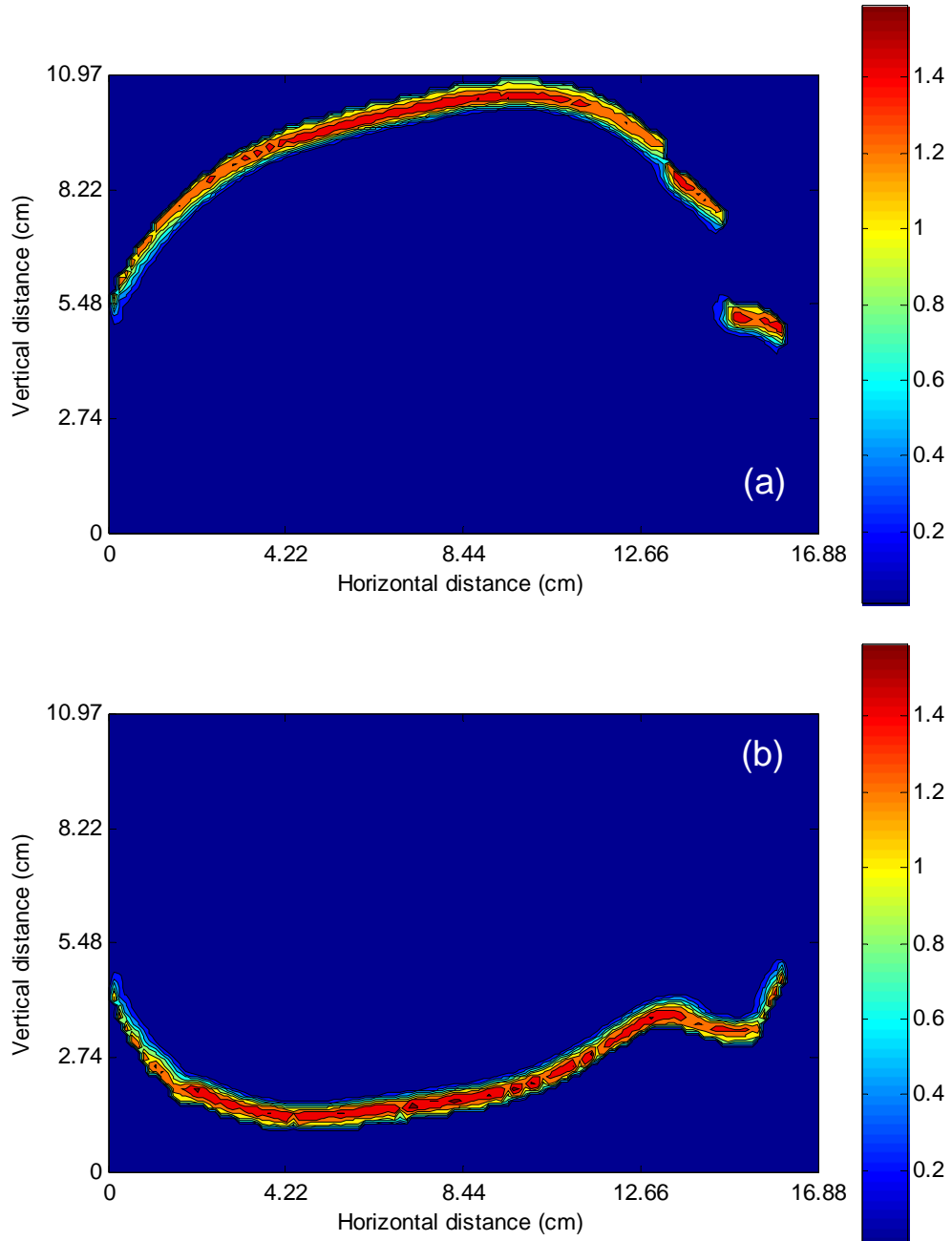


Fig. 6.10. Simulated dose distributions (in kGy) of a whole chicken at 1.35 MeV electrons. (a) at upper beam direction, (b) at lower beam direction, (c) at upper and lower beam directions, (d) at the horizontal point (8.44 cm).

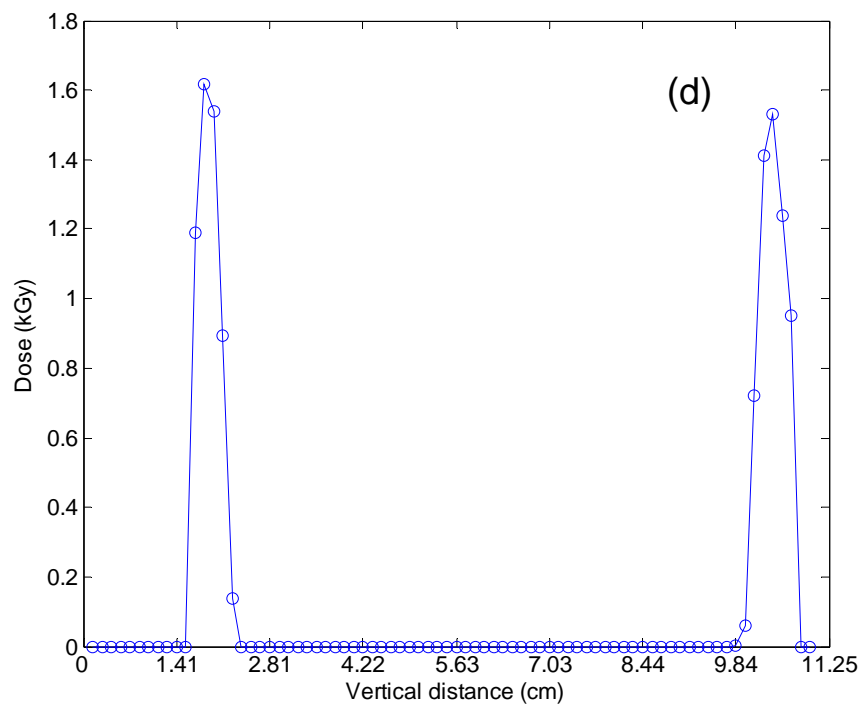
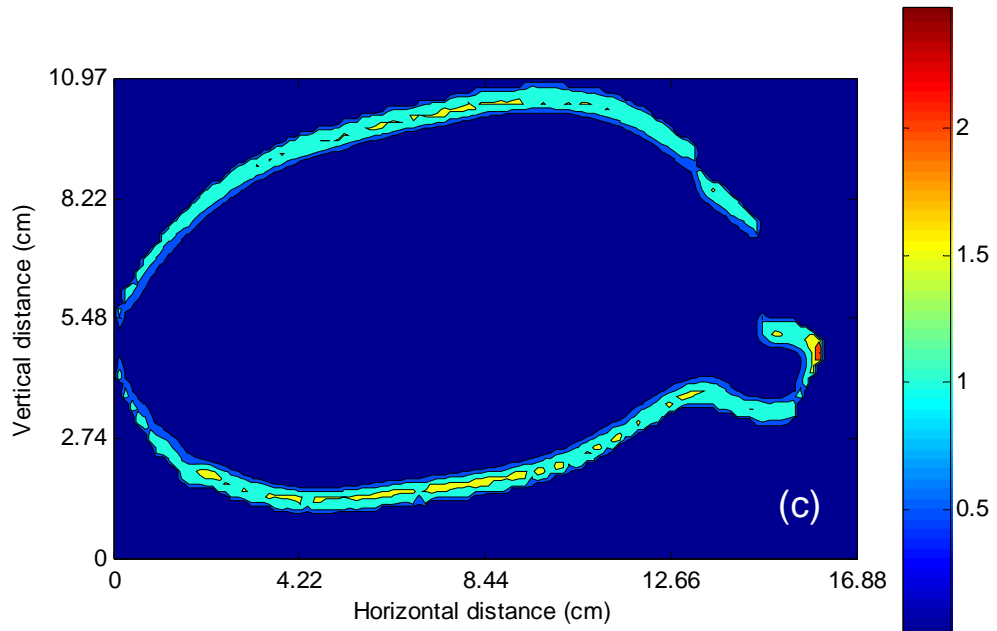


Fig. 6.10. Continued.

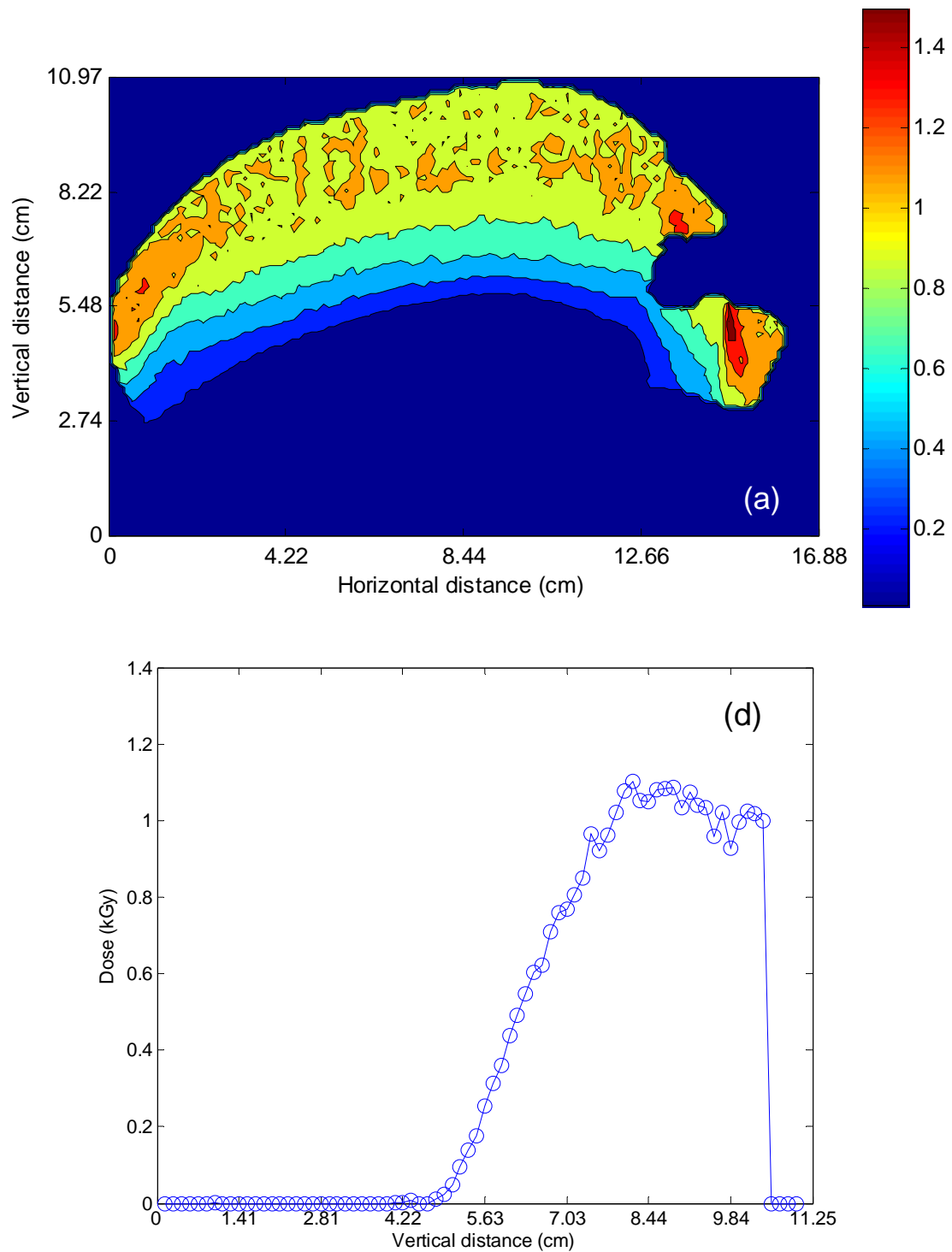


Fig. 6.11. Simulated dose distributions (in kGy) of a whole chicken at 10 MeV electrons; (a) at upper beam direction, (b) at lower beam direction, (c) at double beam direction, (d), (e), and (f) at the horizontal point (7.03 cm).

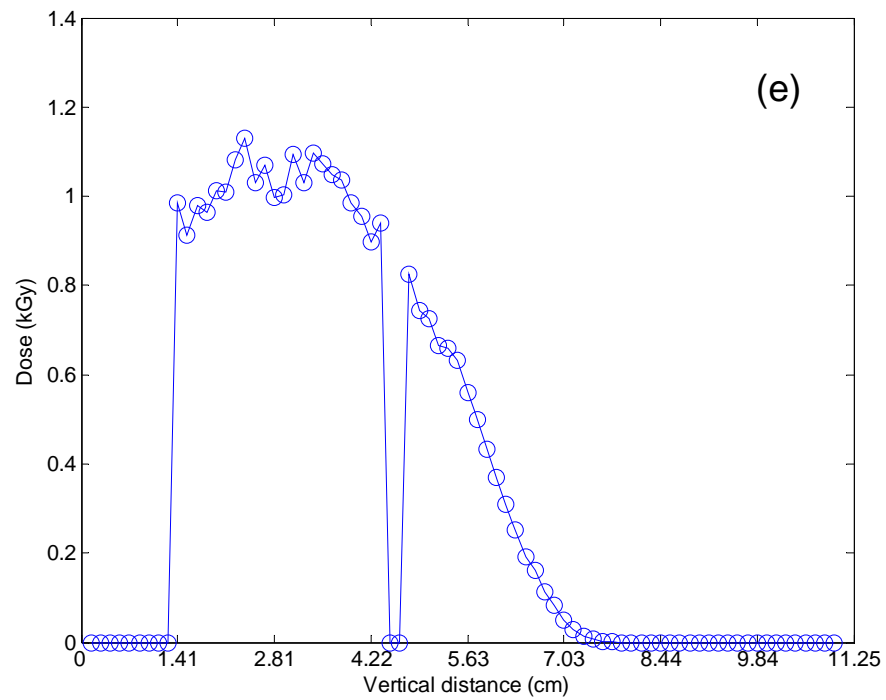
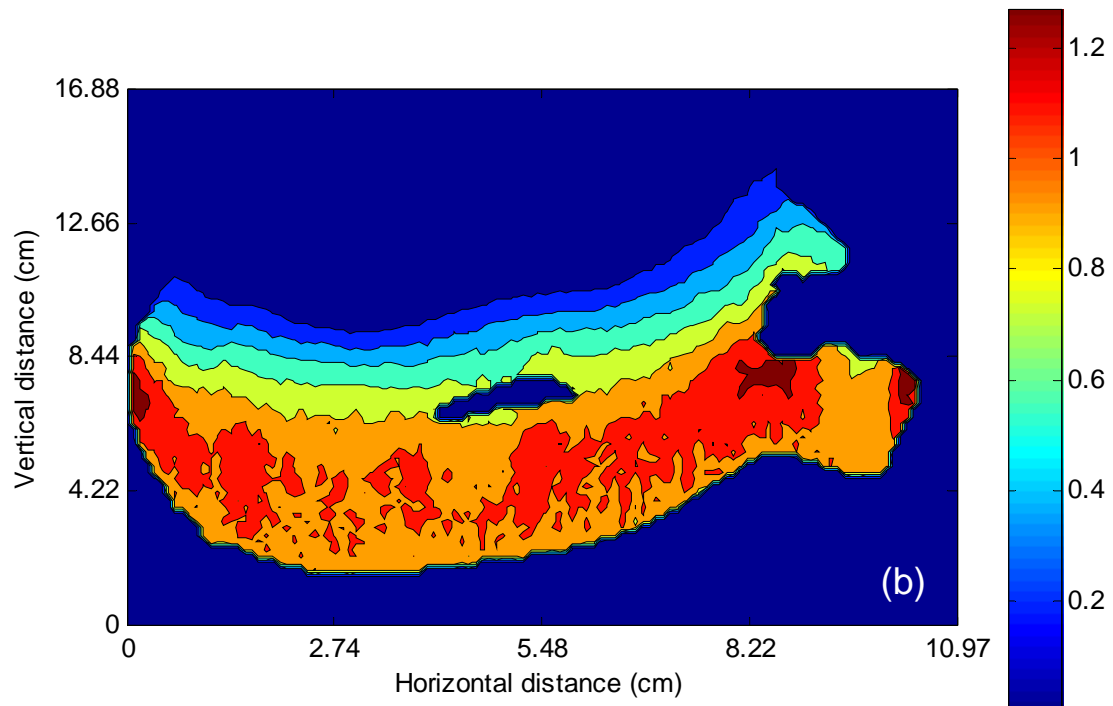


Fig. 6.11. Continued.

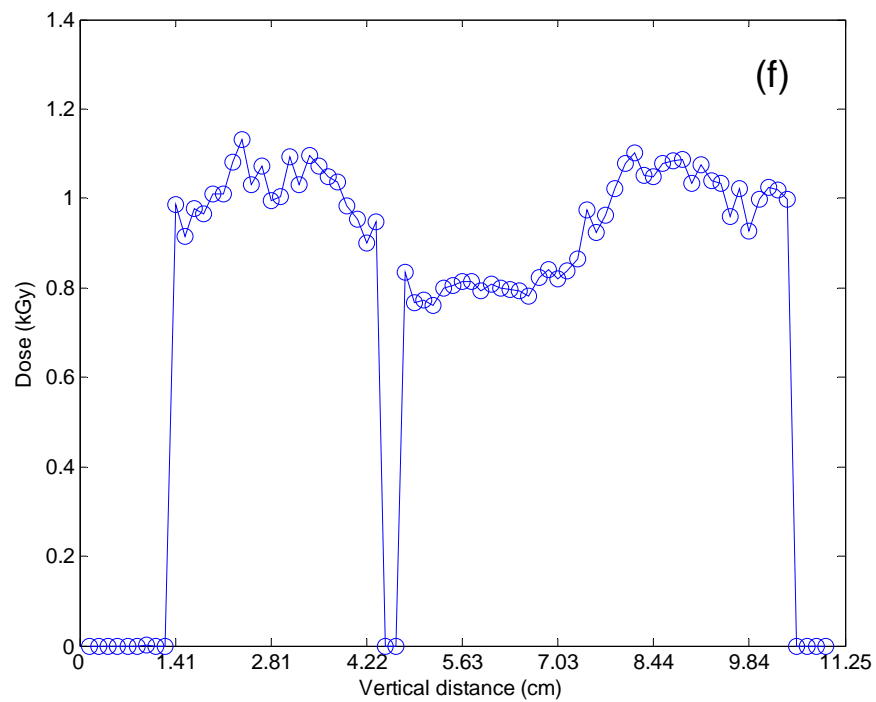
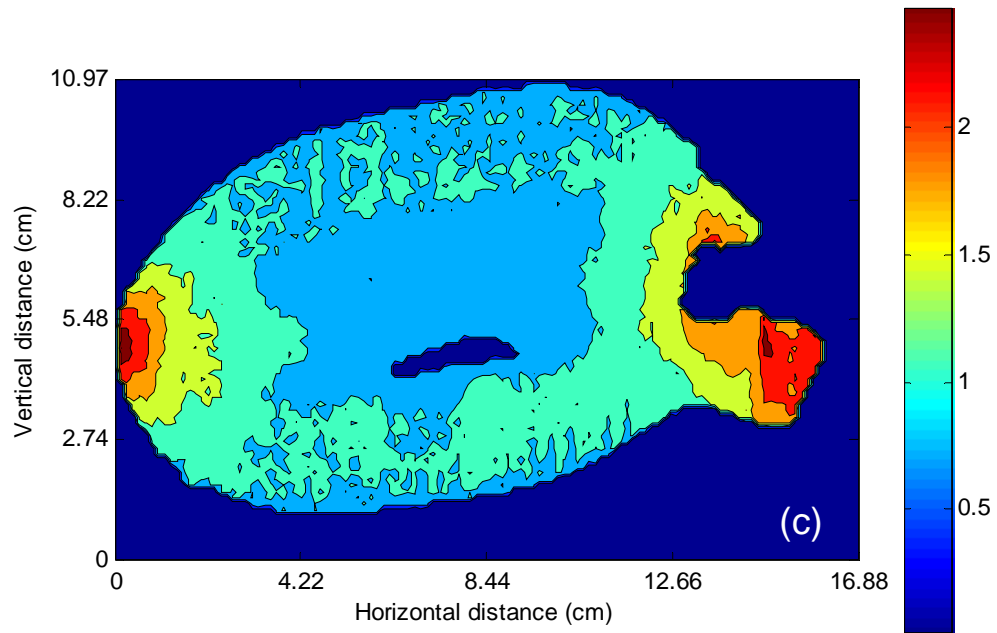


Fig. 6.11. Continued.

Note, however, that a lower dose value (almost zero) around the cavity of the chicken (Fig. 6.11e) where air was the main component.

When both top and bottom e-beam sources were used (Fig. 6.11c), the whole chicken was irradiated and a dose uniformity ratio ( $D_{max}/D_{min}$ ) of 1.6 ( $=1.175/0.75$ ) along the vertical line at the horizontal point of 7.03 cm was obtained, which is within the acceptable range of most food irradiation treatments. The dose distributions in this case mirror each other (Fig. 6.11f) with exception of the cavity region of the chicken. Dose distributions in the whole chicken are not uniform, though. Higher dose values were observed around the tip of the drumstick and at the rear area on the left-side region (Fig. 6.11c) where the dose was twice the target value of 1 kGy because of the overlap of the beam energy depth and also due to change in the component densities (skin, meat, bone, fat).

#### **6.4.5 Dose Distribution Simulations of Chicken Carcass at 5 MeV X-rays**

Fig. 6.12 shows the simulation results of dose distribution in the chicken carcass using X-rays from the 5-MeV LINAC accelerator. The results clearly show the penetration power of photons. Although the product is not homogeneous, the absorbed dose decreased continuously. However, the dose uniformity ratio was 2.5 ( $=0.95/0.38$ ) along the vertical line at the horizontal point of 7.03 cm, when the product was irradiated either from the right (Fig. 6.12a) or from the left (Fig. 6.12b) only. Two-sided X-ray irradiation improved its uniformity ratio to 1.8 ( $=1.55/0.85$ ).

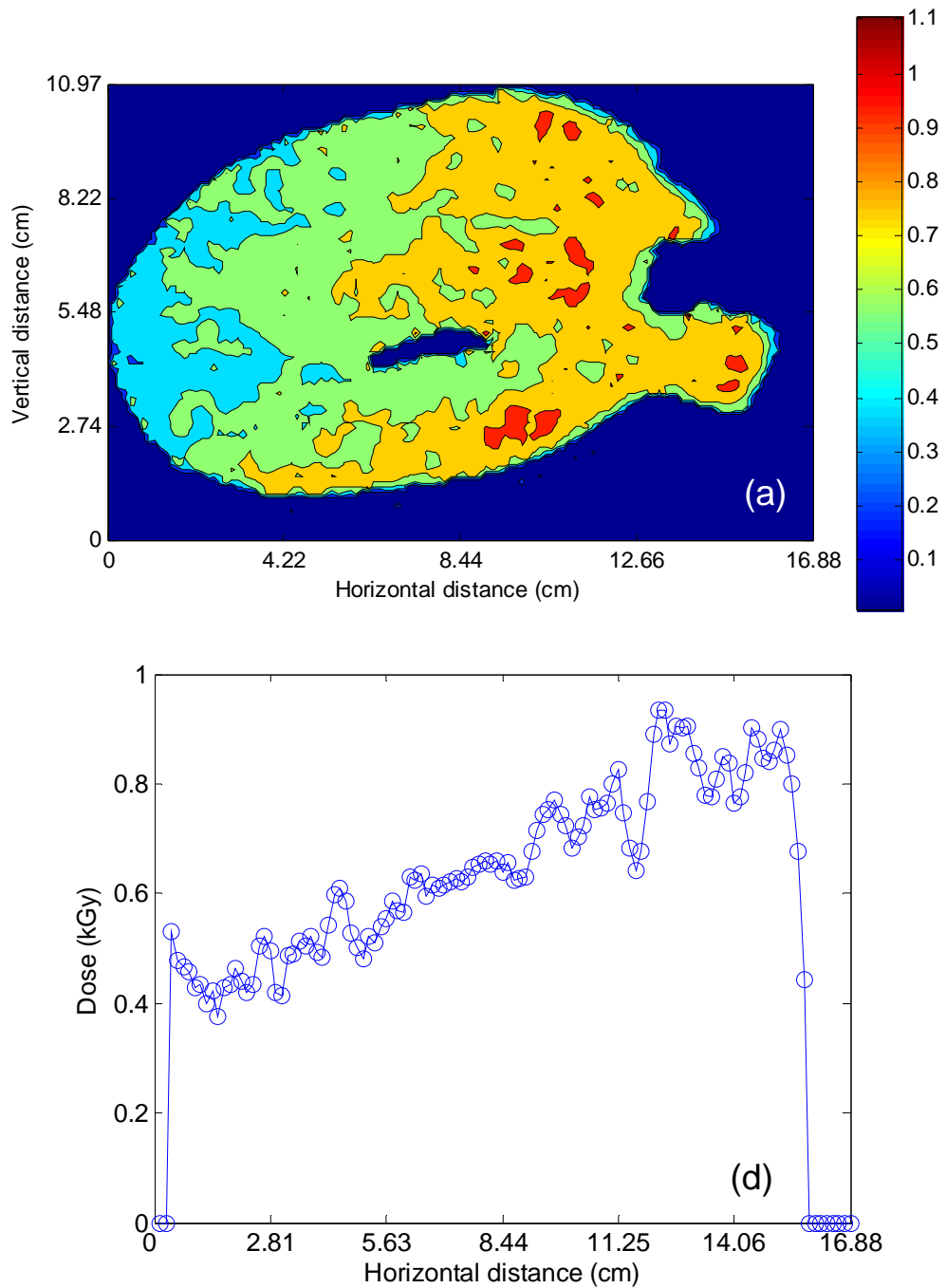


Fig. 6.12. Dose distribution (in kGy) of a whole chicken at 5 MeV X-rays: (a) at right beam direction, (b) at left beam direction, (c) at double beam direction, (d), (e), and (f) at vertical point (7.03 cm).

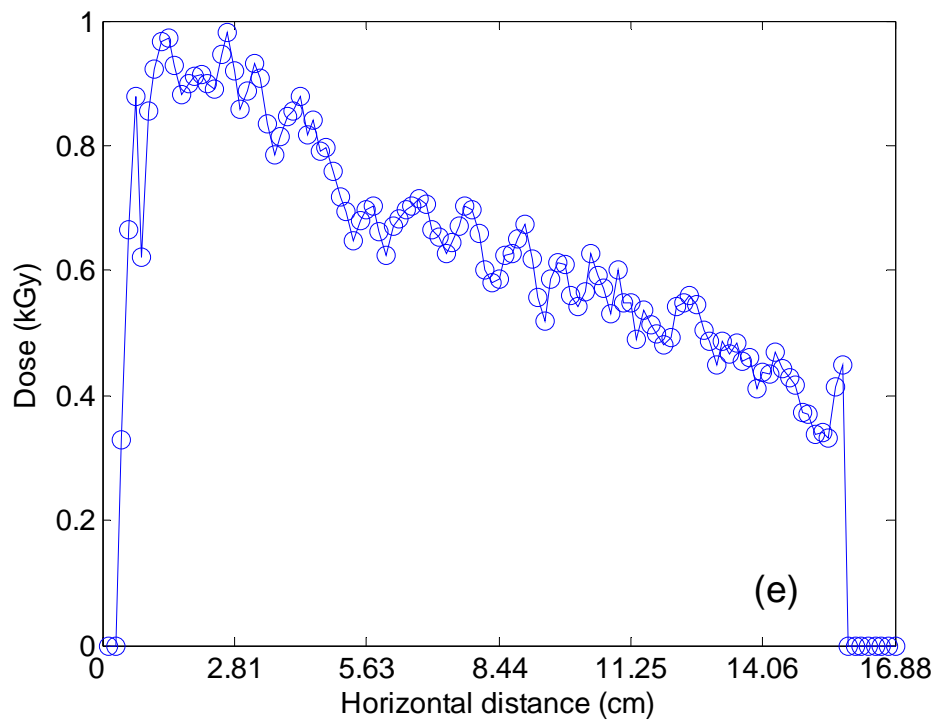
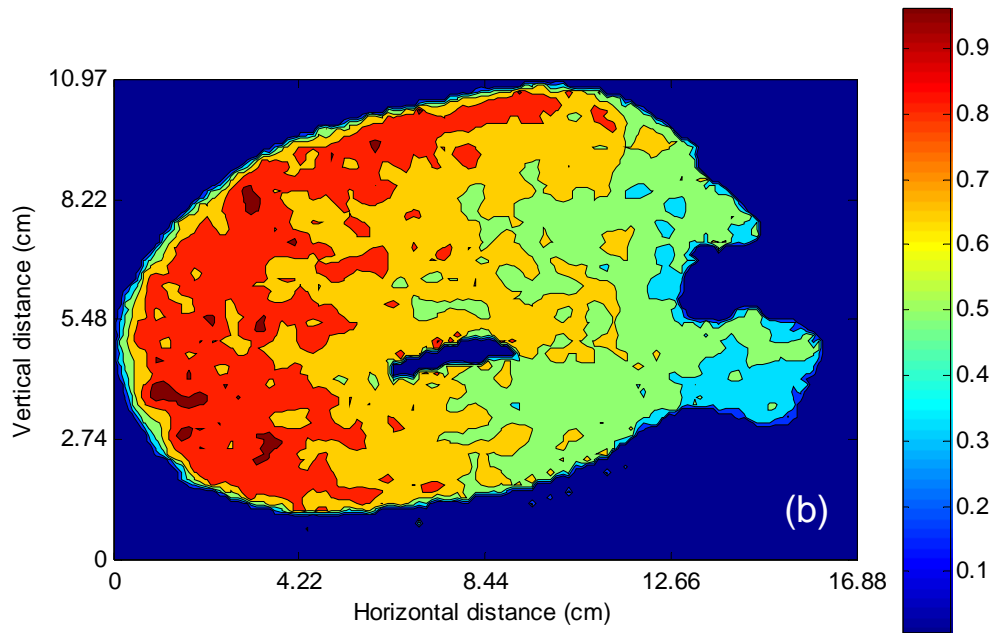


Fig. 6.12. Continued.



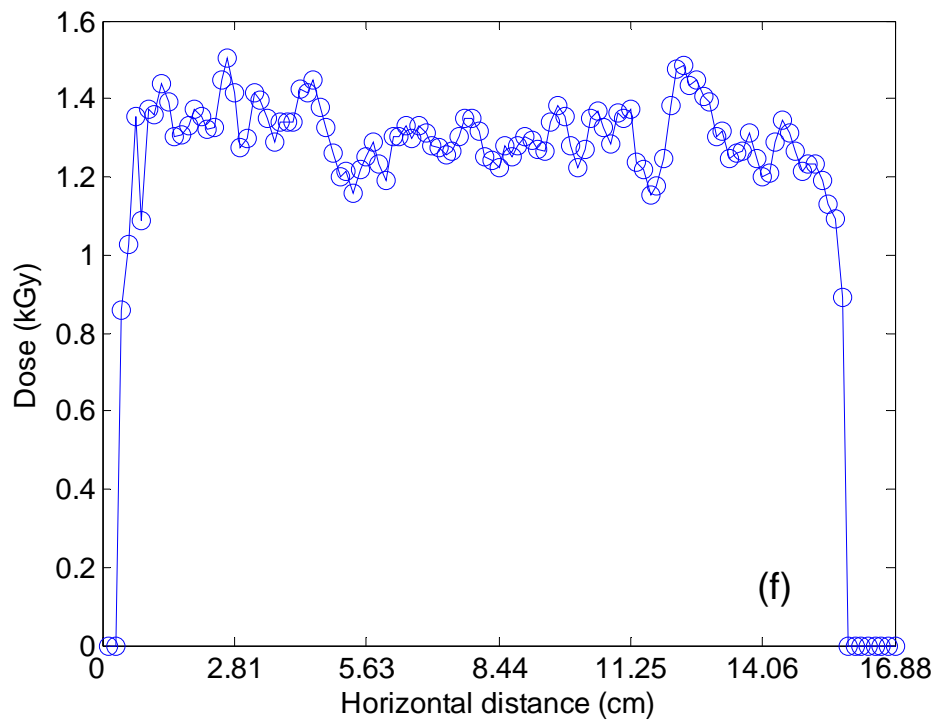
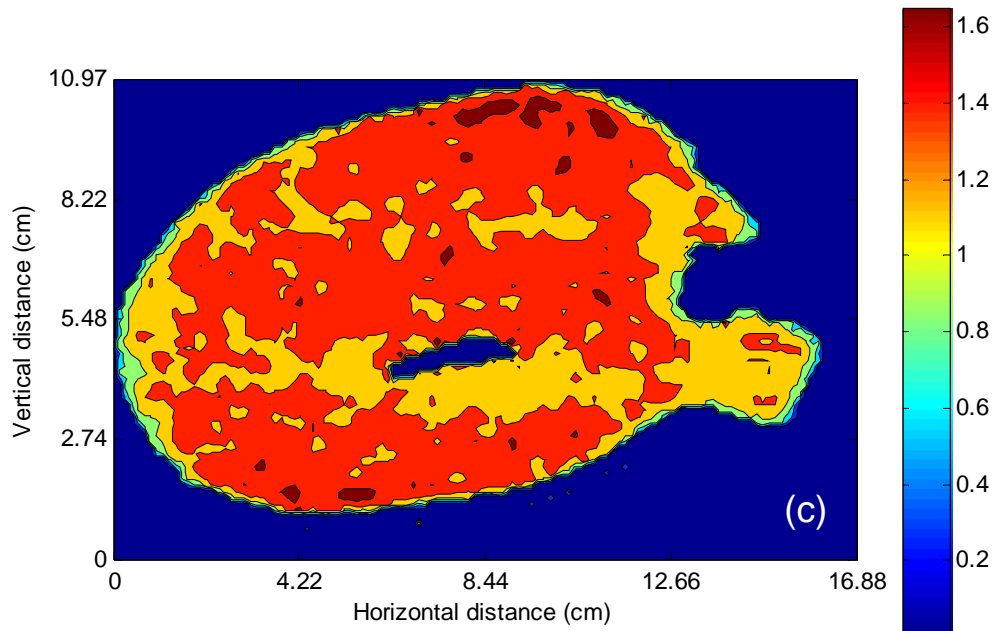


Fig. 6.12. Continued.

These results provide valuable information to develop proper procedure for irradiation of irregularly shaped and heterogeneous foods.

## **6.5 Conclusions**

This research demonstrates a successful development and application of a method to build 3-D geometrical models of food products with image processing techniques based on CT scans. The Matlab software was used to develop image processing algorithms. Procedures were developed to produce informative 3-D reconstructions. These 3-D geometrical models strongly support effective Monte Carlo simulations for the accurate calculations of uniform dose distribution on non-homogeneous food products.

For low energy irradiation (1.35 MeV), dose absorption occurred up to 5-7 mm deep, so this treatment would result on surface irradiation of the carcass. For high energy treatment (10 MeV), two-sided (top and bottom) irradiation resulted in a dose uniformity ratio of about 1.6, which is within the acceptable range of most food irradiation treatment. Although the carcass is non-homogeneous (skin, bone, meat, and fat), the absorbed dose decreased continuously when exposed to photons (5 MeV X-rays). These results provide valuable information to develop proper procedures for irradiation of irregular shaped and heterogeneous foods.

## CHAPTER VII

### A WEB-BASED INFORMATION SYSTEM FOR MCNP SIMULATION OF IRRADIATION OF COMPLEX SHAPED FOODS

#### 7.1 Overview

A web-based integrated system was developed for data manipulation and management for particle transport simulation in foods. High energy particle transport simulation of foods is an important food irradiation technique for dosimetry assessment of a given irradiation system to deliver the required dose to the products intended for treatment. A CT (Computed Tomography) based 3-D geometric modeling technique for foods was developed and is used to provide input data to the general Monte Carlo N-Particle (MCNP) code. We developed a web-based interface to provide the on-line capability to formulate input data for the MCNP and to visualize and analyze output data generated by MCNP. The integrated Matlab and Matlab Web Server programs automatically functions through the steps and procedures for data input and output during simulation. In addition, a database storing data such as  $D_{10}$  values, food nutrition composition, and quality was integrated to support food irradiation research. This system will enable flexible and reliable operations through the Internet by food irradiation engineers and researchers by providing data preparation, analysis, and interpretation during the process of irradiation simulation of complex shaped foods.

## 7.2 Introduction

Whenever electron beams (or X-rays) are used to irradiate food products, a compromise must be made between the quality of the treatment (i.e., decontamination, surface pasteurization, disinfestations) and the radiation dose received by the foods. At the optimal point, the lowest dose is applied so that it can still have the same effect, i.e., to maximize the inactivation of pathogens while minimizing produce quality losses. Thus, the goal of all irradiation treatments should be to find the minimum dose possible to achieve food security.

Simulation of absorbed dose in food products is an important technique for dosimetry assessment of a given irradiation system to deliver the required dose to the products intended for treatment. Kim, Moreira, Huang, and Castell-Perez (2007) developed a computed tomography (CT) based 3-D geometric modeling technique for foods to provide input data for the general Monte Carlo N-Particle (MCNP) simulation code (Brown, 2003). A Web-based information system for simulation of food irradiation was proposed to be available over the Internet to provide flexibility, reliability, and accuracy in data preparations, analysis, and interpretation in the process of MCNP simulation over distributed computers. Thus, users interested in food irradiation could interactively access the simulation process on-line.

The objective of this study was to develop a web-based integrated information system for data processing, visualization, and analysis for MCNP simulation irradiation of heterogeneous complex shaped foods.

## **7.3 Background**

### **7.3.1 Monte Carlo Method**

Monte Carlo method is currently the most accurate procedure for dose calculation in electron beams. The particle tracks or histories are generated by simulating the random nature of the particle interactions within the medium, so it “solves” a transport problem by simulating particle histories rather than by solving an equation. The method thus estimates dose by summing and averaging the histories of many particles. This calculation proceeds by constructing a series of trajectories, each segment of which is randomly chosen from a distribution of applicable processes. For example, the energy loss and angular deflection of the electron during each interaction can be sampled from a probability distribution based on an appropriate multiple scattering theories. By tracing a large number of particle histories, it is possible to track the interactions of individual particles in their passages through the matter and to obtain distributions of many desired physical quantities. The particle history is established as the particle undergoes a series of interactions, and it ends when the particle becomes absorbed, leaves the region of interest, or loss energy to a significant degree (Cashwell & Everett, 1959).

Nowadays, the Monte Carlo method is the most widely used in simulating the actual radiation transport in complex three dimensional geometry systems. Monte Carlo calculations, however, require large amount of computing time to obtain satisfactory precision of dose estimate. To decrease computing time, approximate trajectories using large path length steps and multiple scattering approaches to particle deflection are used (Berger, 1963). Such approximation paths may cause significant errors, particularly

when the particle tracks are generated near an interface, i.e., a surface separating two media of different compositions (e.g., air and solid). Variance reduction techniques, however, improve the efficiency of the method without increasing the computing effort. There are four classes of variance reduction techniques including truncation, population control, modified sampling, and partially-deterministic methods (Forster, Little, Briesmeister, & Hendricks, 1990).

### **7.3.2 Particle Transport Simulation Codes**

Several codes are available to calculate the transport of electrons and photons: Electron TRANsport Through Extended Media (ETRAN) (Seltzer, 1991), Integrated Tiger Series (ITS) (Halbleib et al., 1992), Electron Gamma Shower (EGS4) (Nelson et al., 1985), MCNP (Brown, 2003), PENetration and Energy Loss of Positrons and Electrons (PENELOPE) (Baro et al., 1995), and Geometry And Tracking (GEANT) (Agostinelli et al., 2003). These codes are continuously being upgraded to improve accuracy and computing time.

### **7.3.3 Monte Carlo N-Particle (MCNP) Code**

Since the first release of MCNP code (MCNP3) in 1983, new features have been added to reflect advances in computer architectures and better physical models. The version MCNP4, released in 1990, was the first UNIX version code and it included multitasking on parallel computer architectures. It also added the condensed-history electron transport algorithms. MCNP5, the latest version, included photonuclear

collision physics, superimposed mesh tallies, and parallel computing enhancement with the addition of support for MPI (Message Passing Interface) (Brown, 2003). Combined with its user-friendliness, versatility, and ability to handle complicated geometries, MCNP5 is the most promising code for a variety of applications in medical physics and dosimetry system.

To simulate electrons or X-rays interaction with matter, MCNP codes require specified geometry and definitions of material, radiation source, and tally. These items of information together formulate the input to the MCNP code.

#### **7.3.4 CT-based Geometric Modeling**

Geometry models derived from CT, Magnetic Nuclear Resonance (MRI), and other types of scans provide accurate representations of the scanned objects, including heterogeneous/complex-shaped food products. The models of these objects are difficult to approximate with other methods. CT scan is a diagnostic test that combines X-ray with computed technology. A series of X-ray beams from different angles are used to create cross sectional images of the target. This technique has been widely used in the medical field for dosimetry planning and analysis in radiotherapy (DeMarco et al., 1998; Yoriyaz et al., 2000).

### 7.3.5 GUIs of Simulation Codes

A GUI (Graphic User Interface) takes advantage of the computer's graphic capability to make the program easier to use. Nowadays, GUI tools are widely used in computer programs because of its interactive demonstration capability. After the introduction and popularization of HTML (Hyper Text Markup Language) for the web and internet browsers, web pages have been used as one of the user interfaces. Using the Hyper Text Transfer Protocol (HTTP), GUI can support not only the standalone programs, but also internet applications.

A three-dimensional user interface was designed with GEANT4 (Agostinelli et al., 2003) for process development and control in electron beam technology (Mittendorfer et al., 2004). Its input window consisted of three parts: materials (elements and compositions), detectors, and electron gun (energy and scan function). Virtual Reality Modeling Language (VRML) was used for the visualization of dose and particle trajectories.

A Java interface for a Monte Carlo code, called SimulRad, was developed to visualize pure water radiolysis (Plante, Filali-Mouhim, & Jay-Gerin, 2005). This interface enables a user to visualize either the spatial distribution of all reactive species present in the track of an ionizing particle, or an animation of the chemical development of the particle track. This interface could be expanded to include the visualization of radiation effects on aqueous solutions containing solutes or biological molecules (such as DNA, proteins, etc).



## **7.4 Materials and Methods**

### **7.4.1 Food Products**

A selection of meats, fruits, and vegetables were obtained from local grocery markets and scanned to obtain 3-D images to be used as input for the MCNP simulation. These food items were chosen because they are heterogeneous in composition (skin, flesh, bone, or seed) and complex-shaped, including whole chicken carcass, head of broccoli, whole cantaloupe, pomelo, blueberries and others.

### **7.4.2 CT Data Acquisition**

A HD-350E X-Ray CT Scanner (Universal Systems, Solon, Ohio) located in the Department of Petroleum Engineering at Texas A&M University was used to scan the food products. This scanner provides three scan modes: pilot, multiple and spiral. The multiple scan mode has been used for the food samples. When foods are scanned by a CT scanner, multi-sliced CT data are obtained and each pixel on the slice is assigned a numerical value, e.g. fat is about from  $-200$  to  $-5$ , water is about  $-5$  to  $5$ , which is related to the densities of each component of the scanned materials.

### **7.4.3 CT Data Processing and Visualization**

Based on the CT data, geometries of food samples can be modeled through image processing algorithms. When CT data were available from the scans, VoxelCalc Plus (KehlCo, Inc., Houston, Texas) was used to retrieve the data. Image processing

procedures were developed with Matlab Image Processing Toolbox (Mathworks, Natick, Massachusetts) to process, visualize, and analyze the data (Kim et al., 2007).

#### **7.4.4 Information System Modules**

Three major modules provide the capabilities for the information system to handle the input and output of the MCNP simulations: (1) MCNP input generation, (2) MCNP output visualization, and (3) food irradiation database.

##### **7.4.4.1 MCNP Input Generation**

A MCNP simulation requires a pre-determined input file containing the target geometry, energy source, and tally parameters. In general, the input file has the following form:

*(Message Block*

*Blank Line Delimiter)*

*One Line Problem Title Card*

*Cell Cards*

.

.

*Blank Line Delimiter*

*Surface Cards*

.

.

*Blank Line Delimiter*

*Data Cards*

.

.

*(Blank Line Terminator)*

*(optional)*

All input lines are limited to 80 columns. A \$ sign terminates data entry.

Anything that follows the \$ sign is interpreted as a comment. Blank lines are used as delimiters and as an optional terminator. Data entries are separated by one or more blanks.

Comment cards can be used anywhere in the input file after the problem title card and before the optional blank terminator card. Comment lines must have a C somewhere in columns 1-5 followed by at least one blank and can be 80 columns long.

Cell, surface, and data cards must all begin within the first five columns. To generate the input file for a MCNP simulation for a food product, the following information is need: food name, CT scan data, particle type (electron/photon), source are, source direction, energy level, number of particles, material components, and energy deposit tally definition. With the input information, we can generate the corresponding input file for MCNP simulation.

#### **7.4.4.2 MCNP Output Visualization**

When the simulation is finished, a defined tally output file will be generated, containing the energy deposit and relative error data. In this module, they are extracted from the output file to present the energy distribution and precision.

#### **7.4.4.3 Food Irradiation Database**

This module provides data of  $D_{10}$  (decimal reduction times) values, nutritional composition, and quality of food products under various irradiation conditions (e.g. electron beam, X-ray, etc.).

#### **7.4.5 Information System Interface**

A high performance GUI is needed between users and the system functions to enable users to interactively access the modules. The Internet provides a powerful environment to build such an interface. With the Internet client-server technique, a Web-based interface can be developed to provide on-line capabilities that generate input data file for the MCNP code, and to visualize and analyze the output data from the MCNP.

Matlab provides powerful tools capable of carrying out information processing and scientific and engineering computing, especially in handling vectors, matrices, and graphics. Matlab and its Image Processing toolbox are effective in handling MCNP input and output (Mathworks, Natick, Massachusetts).

Matlab also provides a Web server that enables individual Matlab programs to operate on the Internet. The Matlab Web Server lets users deploy any Matlab

applications via the Internet. Matlab application programs loaded on the Matlab Web Server can be implemented on any computer with Internet access using a Web browser such as Internet Explorer<sup>®</sup>. Users are not required to learn Matlab, and the Matlab does not need to be installed on the client's machine. The Matlab application resides only on the server machine controlled by the developer.

To create a Matlab Web Server application, we need an HTML input file for submitting data to Matlab and an HTML output file for displaying Matlab results. A regular M-file (Matlab function) is located between the input and output files to code the functions of the Matlab application. The M-file provides additional code as needed to accept input data from the HTML input file and to return results to the HTML output file (Fig. 7.1).

#### **7.4.6 System Server**

The Matlab Web Server was installed on a high performance Dell (Austin, Texas) server computer, PowerEdge 6650. This server computer is operated on the Linux operating system, and it is equipped with four CPUs to provide parallel computing capability. MySQL database and PHP, a server-side HTML embedded scripting language, are provided to develop web applications. Matlab toolboxes are also provided to integrate Matlab programs with the web server.

MCNP was installed on the PowerEdge computer. A PVM (Parallel Virtual Machine) is available on the machine to enable parallel computing of MCNP.

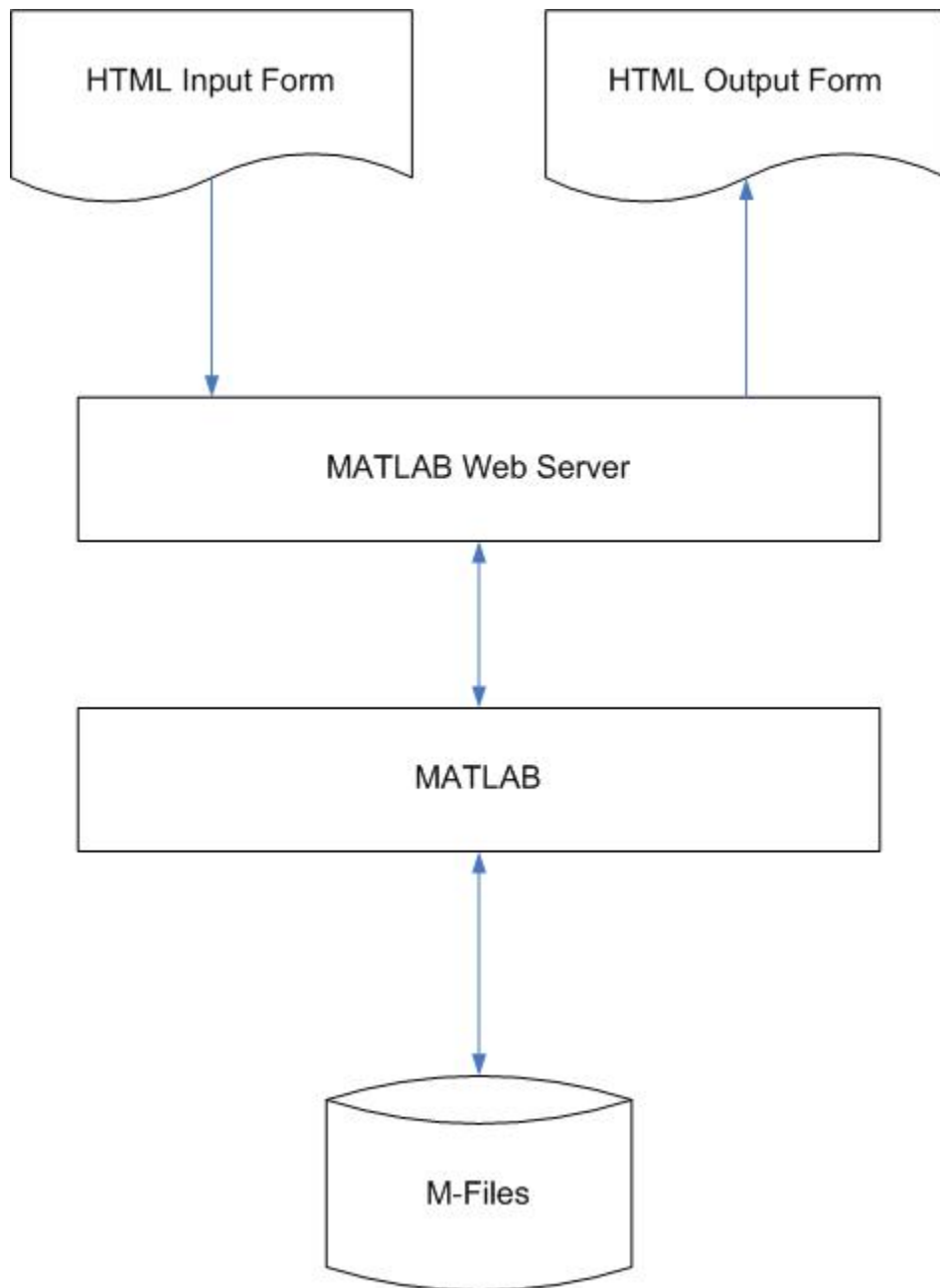


Fig. 7.1. Schematic diagram of a Matlab Web Server application.

### **7.4.7 System Structure**

Fig. 7.2 shows the structure of the Web-based information system for MCNP simulation of food irradiation. This system integrates a web browser, Matlab Web Server, and a backend database, forming a three-tier architecture.

The web browser is on the client tier. It provides the capability for users to browse the web site and access the input and output of the simulation in the inter-network environment.

The Matlab Web Server is on the application tier. It takes the users' specification of parameters for the MCNP simulation, runs the Matlab programs, and sends the program output back to the users' page.

A backend database is on the data tier. This database contains three tables that store attribute data items of food samples, CT scans, and MCNP simulations, respectively. These data are useful for simulation analysis and information system implementation.

### **7.5 System Testing and Demonstration**

Once the system was developed, we tested it to check and fix errors among the three tiers. The system restricts user access. After the user login, the front page comes up (Fig. 7.3). This page shows the connections to the three modules of the system: MCNP input generation, MCNP output visualization, and food irradiation database.

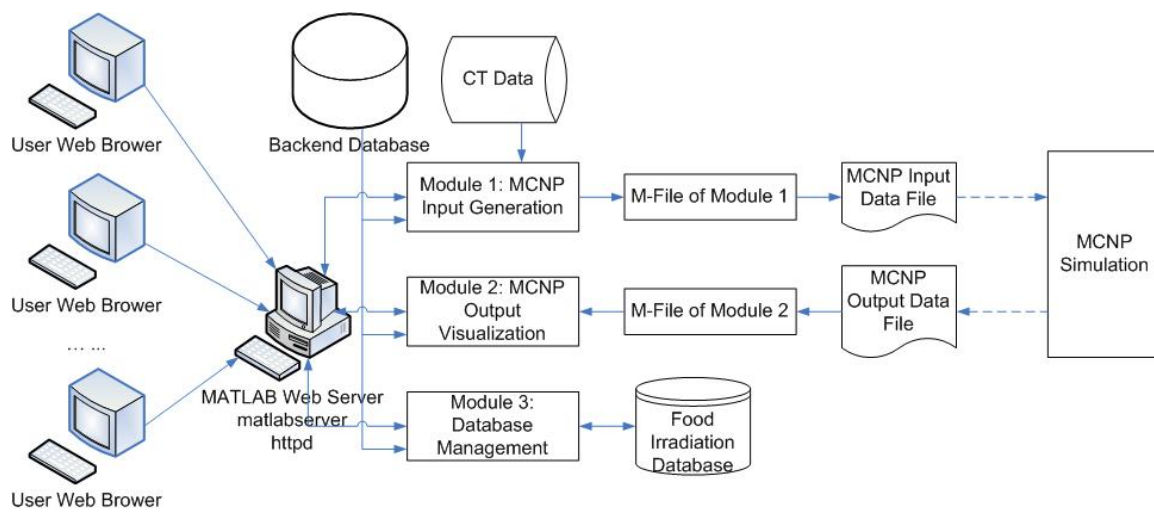



Fig. 7.2. Structure of web-based information system for MCNP simulation of food irradiation.



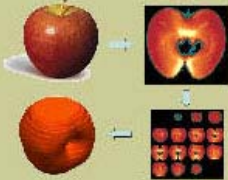


## Food Safety Engineering

The following links will provide examples of dose distribution calculation in selected food products.

[Logout](#)

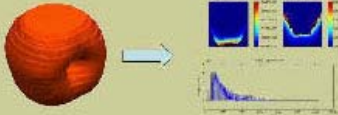
---



### MCNP Input Generation

The image generator creates the input data required to evaluate the dose distribution in the real food products. Once a product is scanned, using a CAT-scanner, the generated data is then transformed to the format required to run the MCNP irradiation simulator. The image generated provides information on the shape and composition of the product.


---



### MCNP Output Visualization

The MCNP irradiation simulator calculates all the energy deposited throughout the whole product. The data is then converted to dose to evaluate the distribution of the energy absorbed by the product.

---



### Food Irradiation Database

The database presented here provides information about composition and D-values for a variety of products and irradiation situations.

Fig. 7.3. Front page of the web-based information system for MCNP simulation of food irradiation.

### 7.5.1 MCNP Input Demonstration

Clicking on MCNP input generation module would get the user into the following page (Fig. 7.4). This page shows that the MCNP input module can work on the following food products: apple, blackberry, blueberry, broccoli, cantaloupe, chicken, mango, and pomelo.

Fig. 7.5 shows the HTML input data form for an apple, for instance. This page provides the default values of the parameters for MCNP simulation. Users can specify these parameters as needed.

In the Source Definition section, users can specify the irradiation source type (electrons or photons), the source area using  $x$ ,  $y$ , and  $z$  coordinates, energy source level in MeV (typically between 1 and 10), and number of particles.

In the Material Component Definition section, users can specify the weight fractions for  $C$  (Carbon),  $H$  (Hydrogen),  $O$  (Oxygen), and  $N$  (Nitrogen), which are the main atomic components of biological materials.

In the Tally Definition section, users can specify the position of  $x$ ,  $y$ , and  $z$  to define the tally area.

In general, MCNP simulations are time consuming. If we process with the CT data in original resolution, the simulation may take from a few hours up to a few days depending on the specified parameters. To allow rapid simulation prototyping, this system provides an option to simulate in high or low resolution under the Voxel Resolution Option. The low resolution simulation may be finished in a few minutes to provide preliminary results before implementing high resolution simulation.

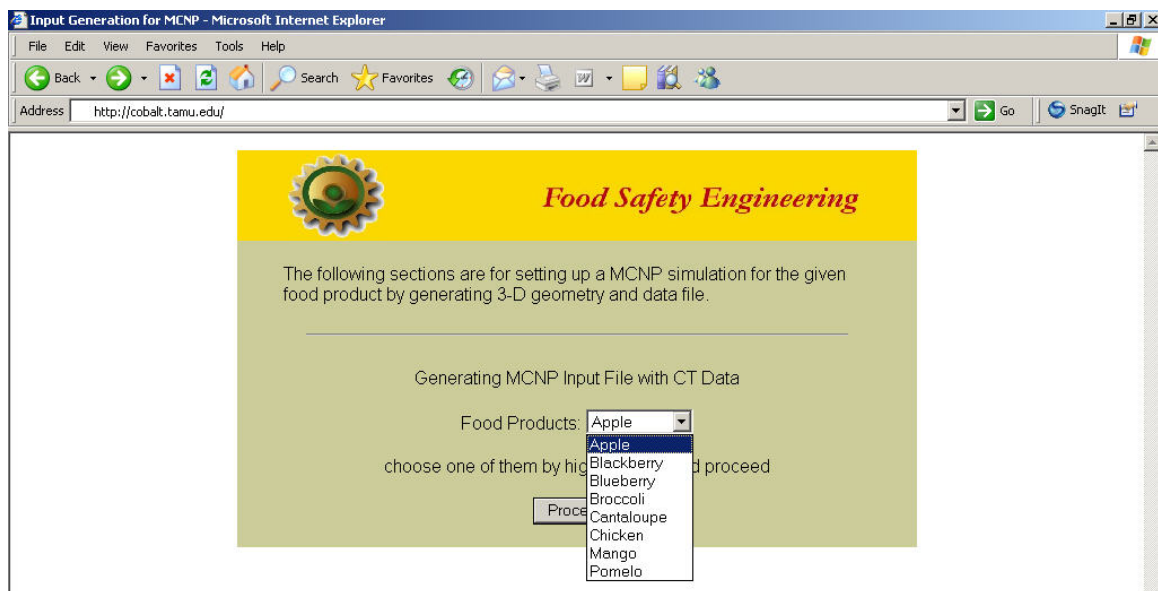



Fig. 7.4. Food product list page in the MCNP input module.



## Food Safety Engineering

The following sections are for setting up a MCNP simulation for the given food product by generating 3-D geometry and data file.

---

Apple (first scanned) CT data has 15 slices.  
 x (slice thickness): 5.0 mm; y (row size): 0.9 mm; z (col size): 0.9 mm

<p style="text-align: center;">Energy Source Definition</p> <p>Particle Type: <input type="text" value="electron"/> <input type="text" value="photon"/></p> <p>Source Area: <input type="text" value="-0.5"/> <input type="text" value="0.5"/></p> <p>x (cm): <input type="text" value="-0.5"/> <input type="text" value="0.5"/></p> <p>y (cm): <input type="text" value="-0.5"/> <input type="text" value="0.5"/></p> <p>z (cm): <input type="text" value="10.0"/> <input type="text" value="10.0"/></p> <p>Energy Level (MeV): <input type="text" value="2.0"/></p> <p>Number of Particles: <input type="text" value="10000"/></p>	<p style="text-align: center;">Material Component Definition (Weight Percentage)</p> <p>C (%): <input type="text" value="0.2"/> H (%): <input type="text" value="0.3"/></p> <p>O (%): <input type="text" value="0.3"/> N (%): <input type="text" value="0.2"/></p> <p style="text-align: center;">Energy Deposit Tally Definition</p> <p>x (cm): <input type="text" value="0"/></p> <p>y (cm): <input type="text" value="NA"/></p> <p>z (cm): <input type="text" value="NA"/></p>
--	---

Voxel Resolution Option

Fig. 7.5. Apple parameter specification page for MCNP simulation input.

After submitting the specified parameters, the simulation input is generated (Fig. 7.6) with the display of graphics of a representative slice image of the CT scanned food. Fig. 7.6 shows a CT slice image deck of a scanned apple, 3-D slice contour image, and a reconstructed 3-D apple that is the basis of the voxel model for the MCNP input. In addition, this page enables viewing the generated MCNP input file on the web. The same file is stored physically on the hard disk of the PowerEdge 6650 server computer. The simulation can then be run under MCNP with the input file.

Similar operations can be implemented on other food products. Fig. 7.7 shows the MCNP input generation pages for broccoli, cantaloupe, chicken, and pomelo.

### **7.5.2 MCNP Output Demonstration**

Fig. 7.8 displays the graphics of the MCNP simulation output of an apple prototype including energy deposit distribution, relative error distribution, and the energy deposit plot. This simulation was conducted with a 10 MeV electron beam source (single upper-beam mode) to the 3-D geometry of the apple in the voxel resolution of  $5 \times 0.3 \times 0.3$  mm (Kim, Moreira, Rivadeneira, & Castell-Perez, 2006a). This page is also shown the energy deposition and corresponding relative error, which are stored on the hard disk of the PowerEdge 6650 server computer for further analysis. Fig. 7.9 shows a screen capture of MCNP output visualization for a broccoli, cantaloupe, chicken, and pomelo.

## Food Safety Engineering

The 3-D voxel data have been generated and the corresponding MCNP input data has been filled into the file of [min-e](#). You can left-click on the file name to view the content and right-click to save it on your local drive in order to use it to run MCNP simulation.

CT Graphics

Save Simulation Setting Parameters

A CT Slice of Apple

CT Slice Deck of Apple

3D Contour Slices of Apple

Reconstructed 3D Geometry of Apple

Fig. 7.6. Product page of MCNP simulation input generation for an apple.



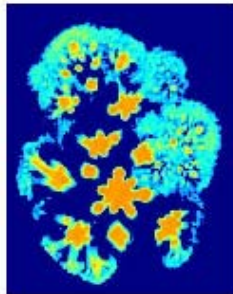
## Food Safety Engineering

The 3-D voxel data have been generated and the corresponding MCNP input data has been filled into the file of [min-e](#). You can left-click on the file name to view the content and right-click to save it on your local drive in order to use it to run MCNP simulation.

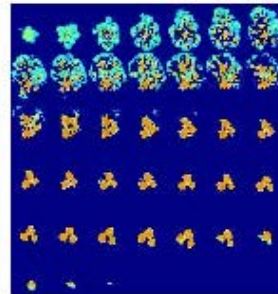
CT Graphics

Save Simulation Setting Parameters

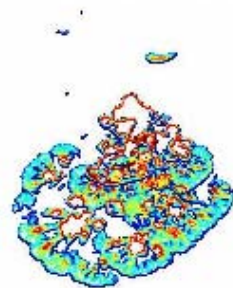
A CT Slice of Broccoli



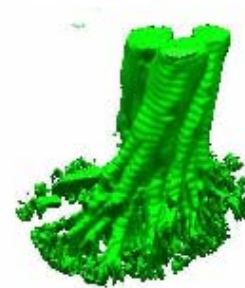
CT Slice Deck of Broccoli



3D Contour Slices of Broccoli



Reconstructed 3D Geometry of Broccoli



(a)

Fig. 7.7. Product pages of MCNP simulation input generation for a (a) bunch of broccoli, (b) cantaloupe, (c) chicken, and (d) pomelo.





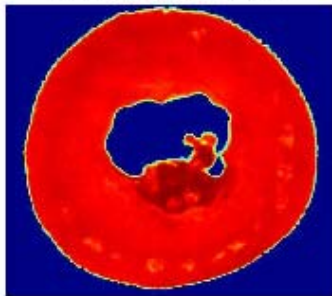
## Food Safety Engineering

The 3-D voxel data have been generated and the corresponding MCNP input data has been filled into the file of [min-e](#). You can left-click on the file name to view the content and right-click to save it on your local drive in order to use it to run MCNP simulation.

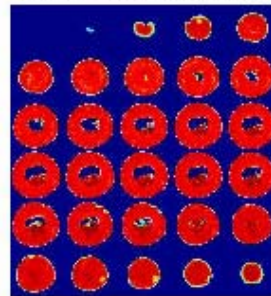
### CT Graphics

Save Simulation Setting Parameters

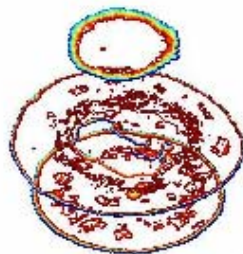
A CT Slice of Cantaloupe



CT Slice Deck of Cantaloupe



3D Contour Slices of Cantaloupe



Reconstructed 3D Geometry of Cantaloupe



(b)

Fig. 7.7. Continued.





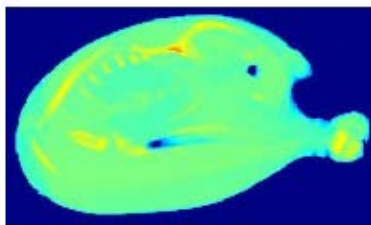
## Food Safety Engineering

The 3-D voxel data have been generated and the corresponding MCNP input data has been filled into the file of [min-e](#). You can left-click on the file name to view the content and right-click to save it on your local drive in order to use it to run MCNP simulation.

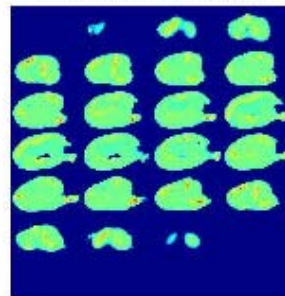
### CT Graphics

Save Simulation Setting Parameters

A CT Slice of Chicken



CT Slice Deck of Chicken



3D Contour Slices of Chicken



Reconstructed 3D Geometry of Chicken



(c)

Fig. 7.7. Continued.



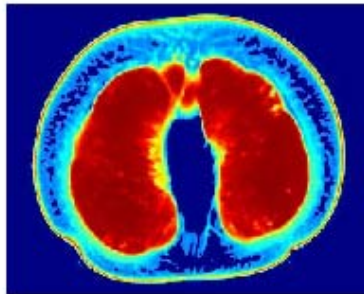
## Food Safety Engineering

The 3-D voxel data have been generated and the corresponding MCNP input data has been filled into the file of [min-e](#). You can left-click on the file name to view the content and right-click to save it on your local drive in order to use it to run MCNP simulation.

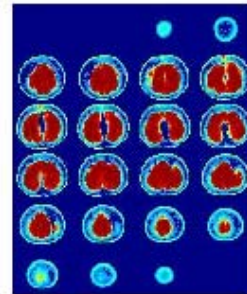
### CT Graphics

Save Simulation Setting Parameters

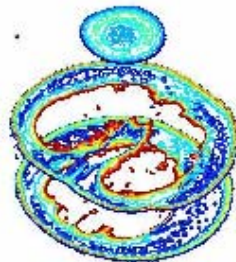
A CT Slice of Pomelo



CT Slice Deck of Pomelo



3D Contour Slices of Pomelo



Reconstructed 3D Geometry of Pomelo



(d)

Fig. 7.7. Continued.

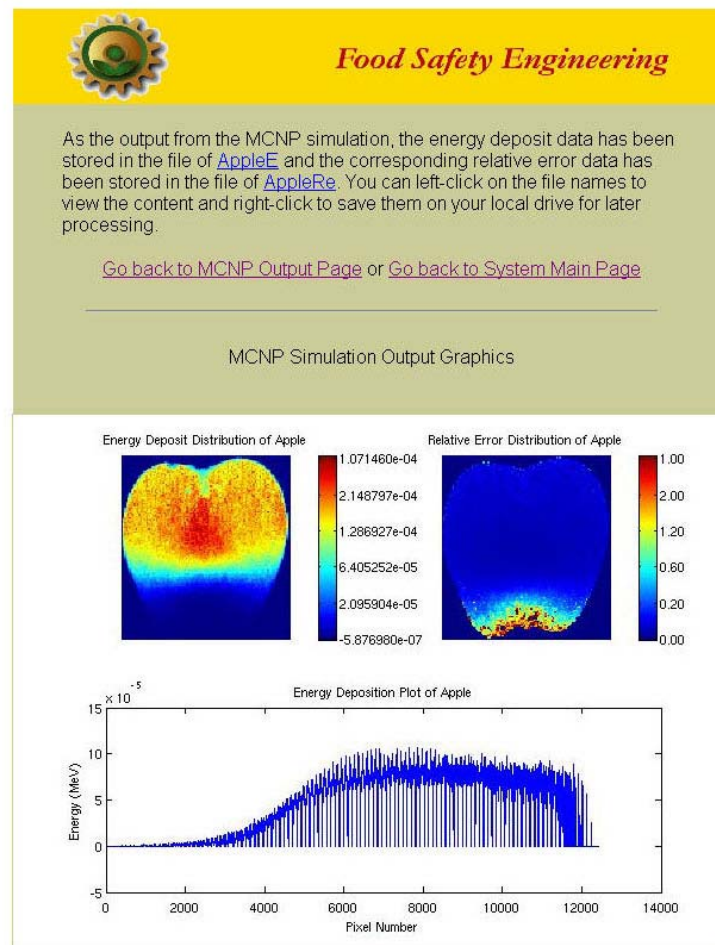


Fig. 7.8. Product page of MCNP simulation output visualization for an apple phantom.

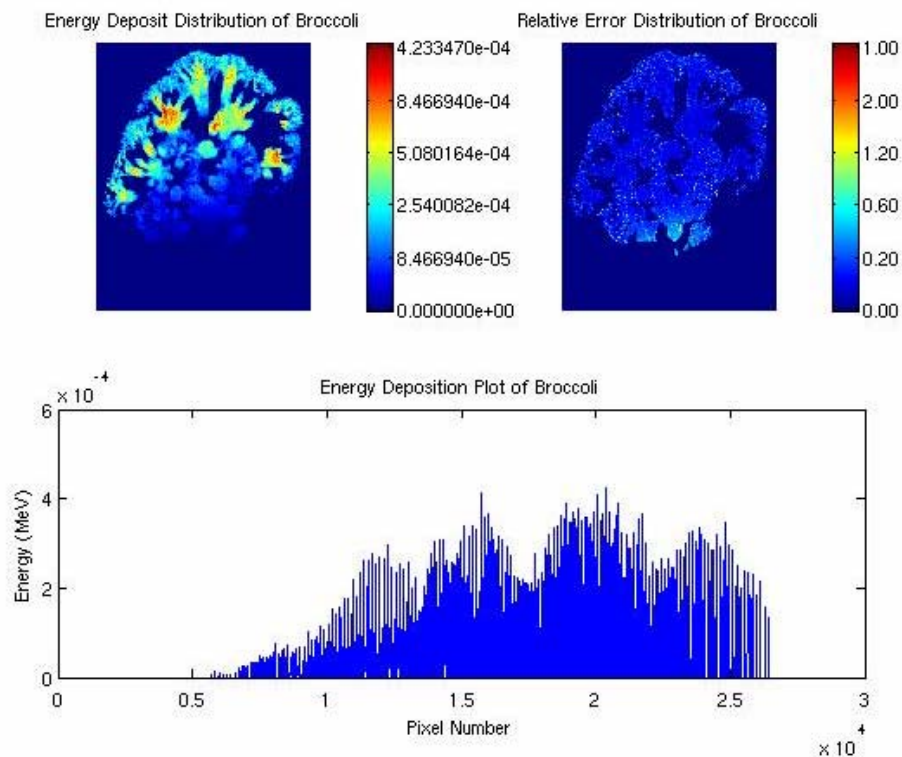


## Food Safety Engineering

As the output from the MCNP simulation, the energy deposit data has been stored in the file of [BroccoliE](#) and the corresponding relative error data has been stored in the file of [BroccoliRe](#). You can left-click on the file names to view the content and right-click to save them on your local drive for later processing.

[Go back to MCNP Output Page](#) or [Go back to System Main Page](#)

### MCNP Simulation Output Graphics



(a)

Fig. 7.9. Product pages of MCNP simulation output visualization for a (a) bunch of broccoli, (b) cantaloupe, (c) chicken, and (d) pomelo.

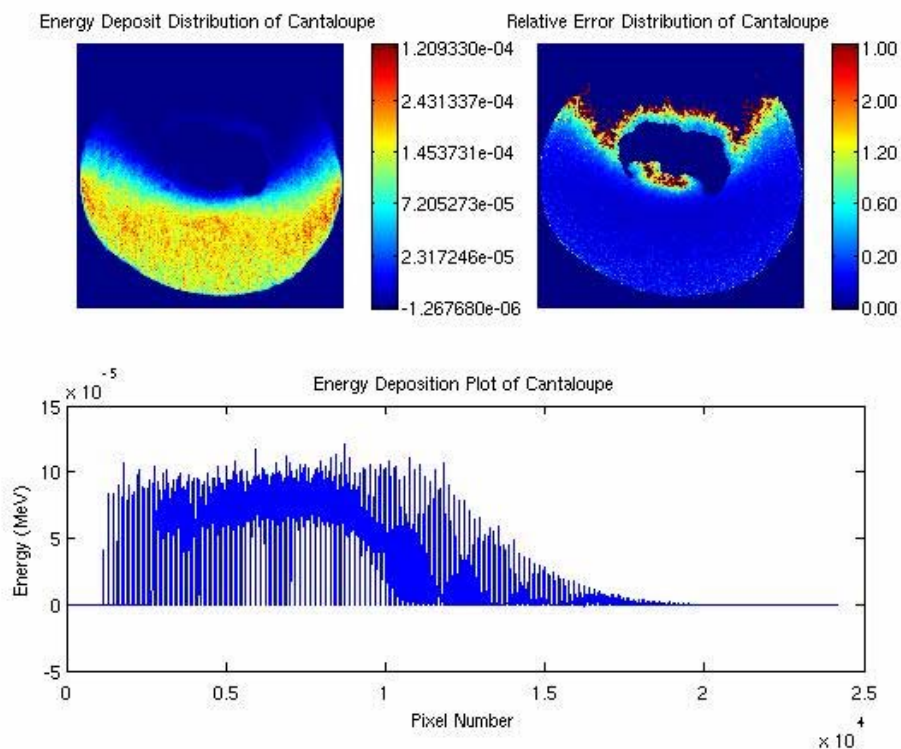


## Food Safety Engineering

As the output from the MCNP simulation, the energy deposit data has been stored in the file of [CantaloupeE](#) and the corresponding relative error data has been stored in the file of [CantaloupeRe](#). You can left-click on the file names to view the content and right-click to save them on your local drive for later processing.

[Go back to MCNP Output Page](#) or [Go back to System Main Page](#)

### MCNP Simulation Output Graphics



(b)

Fig. 7.9. Continued.



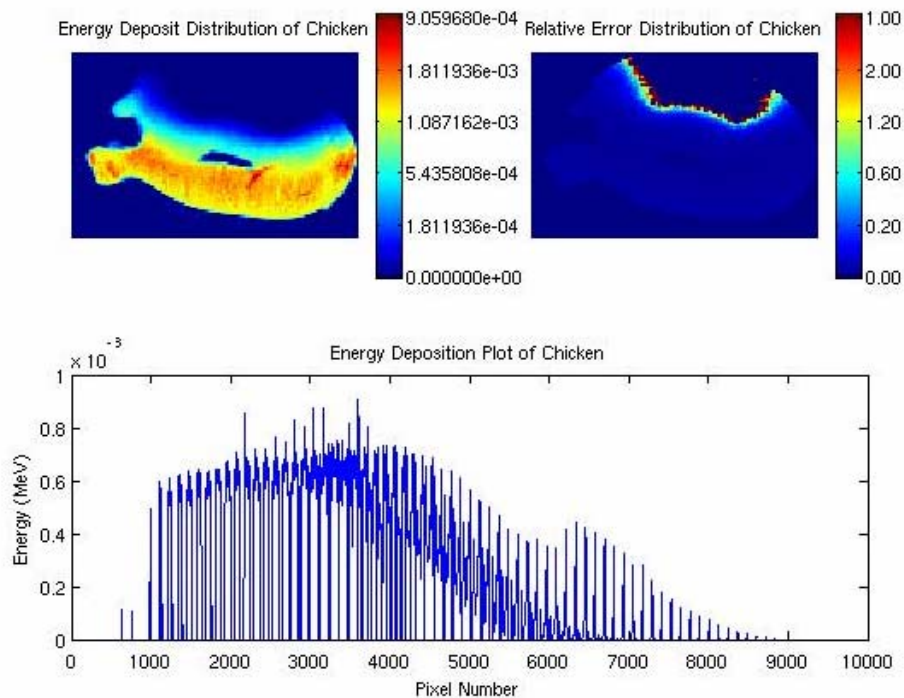


## Food Safety Engineering

As the output from the MCNP simulation, the energy deposit data has been stored in the file of [ChickenE](#) and the corresponding relative error data has been stored in the file of [ChickenRe](#). You can left-click on the file names to view the content and right-click to save them on your local drive for later processing.

[Go back to MCNP Output Page](#) or [Go back to System Main Page](#)

### MCNP Simulation Output Graphics



(c)

Fig. 7.9. Continued.

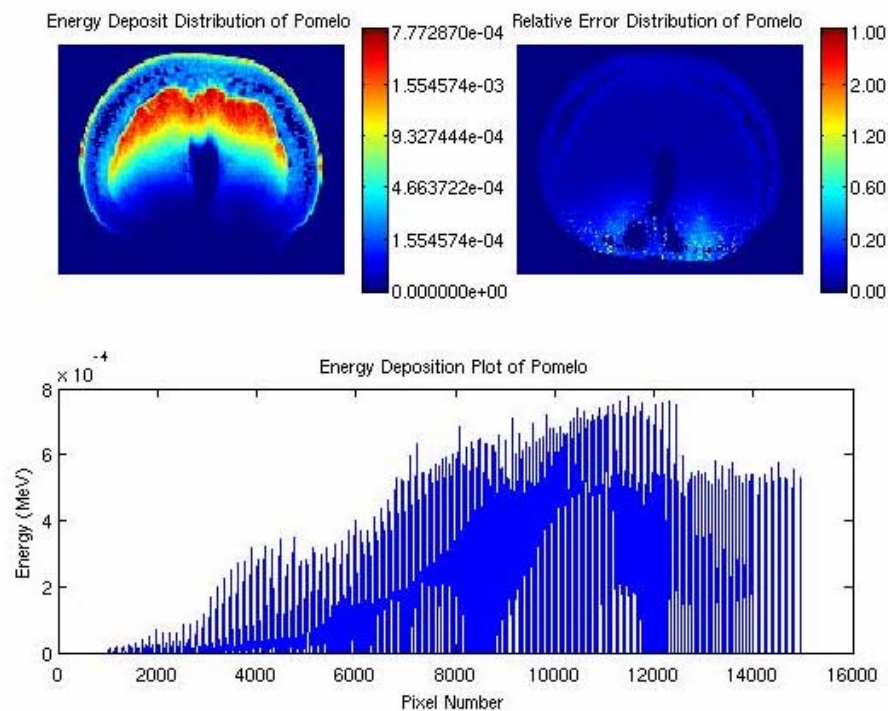


## Food Safety Engineering

As the output from the MCNP simulation, the energy deposit data has been stored in the file of [PomeloE](#) and the corresponding relative error data has been stored in the file of [PomeloRe](#). You can left-click on the file names to view the content and right-click to save them on your local drive for later processing.

[Go back to MCNP Output Page](#) or [Go back to System Main Page](#)

### MCNP Simulation Output Graphics



(d)

Fig. 7.9. Continued.

### 7.5.3 Food Irradiation Database Demonstration

Fig. 7.10 is the screen capture of the microorganism survival rate data of mushroom. The table contains specific foods, microorganisms, conditions,  $D_{10}$  values, and references. The data were collected from the respected references and are being updated.

Fig. 7.11 shows broccoli's nutritional data using USDA National Nutrient Database (USDA, 2006), and its weight-based atomic composition for MCNP simulation. The percentage, except the main atomic components ( $C$ ,  $H$ ,  $O$ , and  $N$ ) is only 0.5%, which could be negligible in radiation simulation.

Fig. 7.12 is the screen capture of the quality data of papaya. The first table shows the relation between the papaya's firmness (N/g) and the absorbed dose (kGy) based on a source (Zhao, Moy, & Paul, 1996). Clicking on the button at the Self Calculation row (Fig. 7.13a), we can calculate the firmness at the intended dose (Fig. 7.13b); e.g., 60.73 N/g at 1.0 kGy.

### 7.6 System Application Example with Broccoli

We used the developed information system to simulate irradiation of several complex-shaped foods. Here we present results from the simulation for a head of broccoli, which consists of green flower heads, and the attached portion of stem. Broccoli contains large amount of vitamin C and soluble fiber, and is popular as a raw vegetable. In general, fruits and vegetables are easily contaminated with various



foodborne pathogens during the handling and processing. The broccoli compact cluster head can be easily exposed to microorganisms.

**Food Safety Engineering**

### The D-value data for *Mushroom*

<b>Food</b>	mushrooms in cream sauce
<b>Microorganism</b>	<i>Clostridium sporogenes</i>
<b>Temperature (°C)</b>	-40
<b>Temperature Variation (°C)</b>	NA
<b>Temperature Range (°C)</b>	NA
<b>Atmosphere</b>	vacuum
<b>Special Conditions</b>	spores
<b>D<sub>10</sub> (kGy)</b>	NA
<b>D<sub>10</sub> Variation (kGy)</b>	NA
<b>D<sub>10</sub> Range (kGy)</b>	3.1 - 4.03
<b>Reference</b>	International Commission on Microbiological Specifications for Foods. Microorganisms in foods 5 : characteristics of microbial pathogens / ICMSE. New York : Blackie Academic & Professional, 1996.

Close This Window

Fig. 7.10. The microorganism (*Clostridium sporogenes*) survival rate data (D-value) of mushroom.



### The nutritional data for *Broccoli*

Scientific Name	Brassica oleracea
Type	NA
Condition	raw
%Water	90.69
%Protein	2.98
%Total Lipad (Fat)	0.35
%Ash	0.92
%Carbonhydrate, by difference	5.24
%Fiber, toatl dietary	3
<b>Weight Based Composition Percentage (The calculation is based on the data extracted from USDA National Nutrient Database. The results are adjusted to 4 decimal points for the use of MCNP program)</b>	
C	3.2399%
H	10.7458%
O	85.2278%
N	0.2875%
Ca	0.0486%
Fe	0.0009%
Mg	0.0253%
P	0.0669%
K	0.3293%
Na	0.0274%
Zn	0.0004%
Cu	NA
Mn	0.0002%
F	NA
S	NA
Ar	NA
Cl	NA
Reference	USDA National Nutrient Database for Standard Reference

Fig. 7.11. Broccoli's nutritional data and chemical composition (USDA, 2006).

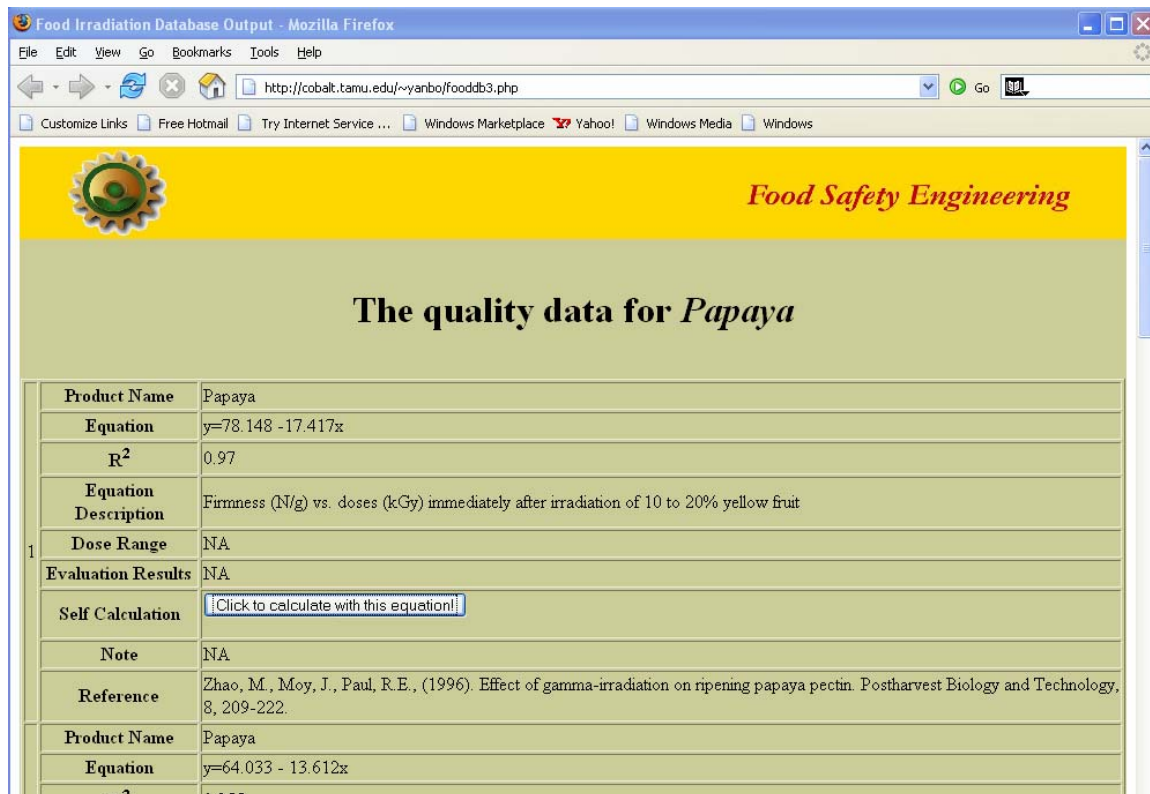
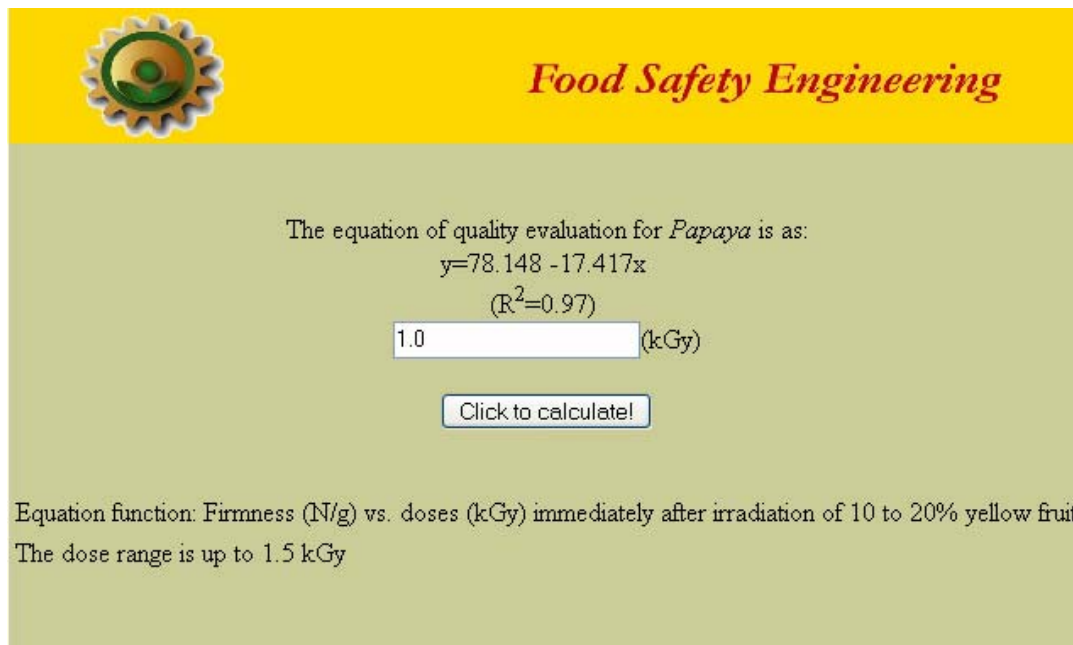


Fig. 7.12. Papaya's quality data.

(a)



**Food Safety Engineering**

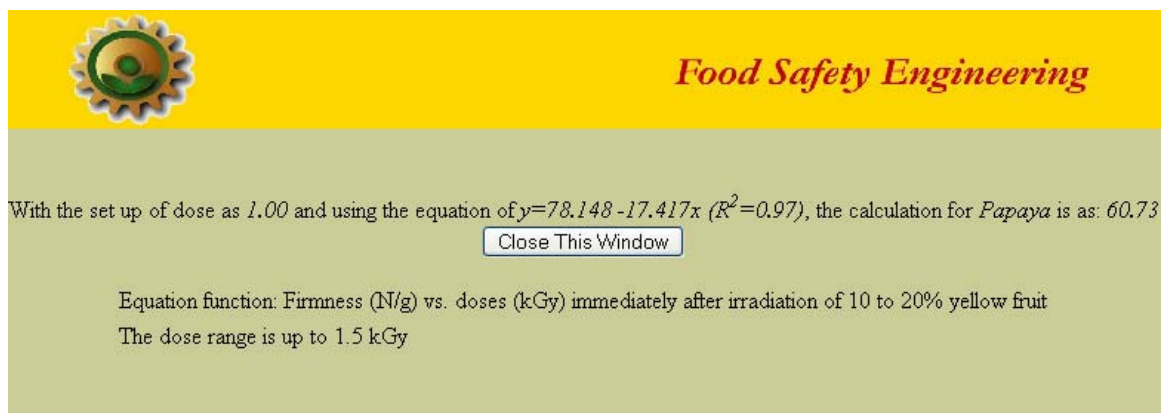
The equation of quality evaluation for *Papaya* is as:  
 $y=78.148 - 17.417x$   
 $(R^2=0.97)$

1.0 (kGy)

Click to calculate!

Equation function: Firmness (N/g) vs. doses (kGy) immediately after irradiation of 10 to 20% yellow fruit  
 The dose range is up to 1.5 kGy

(b)



**Food Safety Engineering**

With the set up of dose as 1.00 and using the equation of  $y=78.148 - 17.417x$  ( $R^2=0.97$ ), the calculation for *Papaya* is as: 60.73

Close This Window

Equation function: Firmness (N/g) vs. doses (kGy) immediately after irradiation of 10 to 20% yellow fruit  
 The dose range is up to 1.5 kGy

Fig. 7.13. Self calculation of papaya's firmness: (a) the dose input and (b) the firmness calculation output.

### 7.6.1 MCNP Input File Generation for Broccoli Simulation

There are two types of radiation source, electron, or photon, widely used in food irradiation treatments. Low energy electrons (e.g., less than 2 MeV) are applied for the surface treatment of food, because they have limited penetration capability. Photons (or X-rays), on the other hand, have greater penetrating capability and are used for processing of relatively thick or dense products. In the case of the bunch of broccoli, we tested the system for both types of radiation source.

After choosing the radiation source, the source area needs to be specified. For instance, if the source is directed from the top to the bottom, the  $z$  coordinate values should be the same and positive (Fig. 7.14). If the source direction is reverse, the  $z$  coordinate values should be negative.

The maximum energy allowed, in food irradiation, from a linear accelerator (LINAC) is 5 MeV for X-rays and 10 MeV for electrons (Kim et al., 2006a). For surface irradiation, the energy level was 1.35 MeV, an electron kinetic energy value for surface treatment of food using a Van de Graaff accelerator, for example (Kim et al., 2007).

Generally, a total of  $10^6 - 10^7$  histories are required to obtain statistically reliable results. However, since it takes enormous amount of computing time, we can check the particle's trajectory in less than 5 minutes by using a smaller number of histories (50-100) (Fig. 7.15). We used this procedure to verify if the simulation was on the right track. For example, to determine the penetration depth of the electrons or how did they behave on the sample boundary.

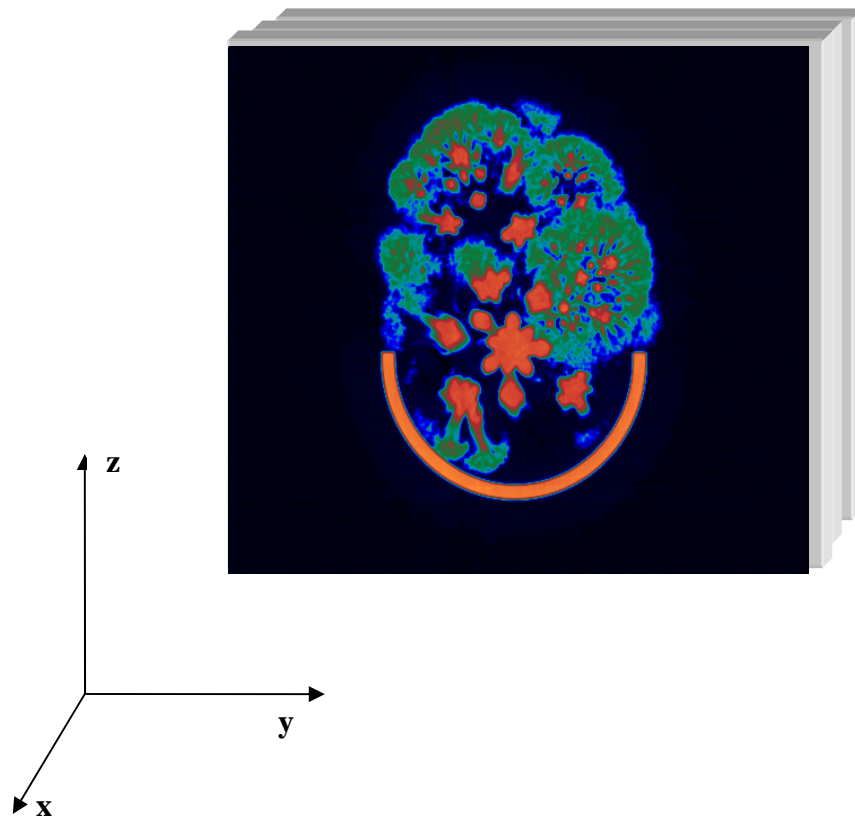


Fig. 7.14.  $xyz$  coordinates for the scanned broccoli's position.

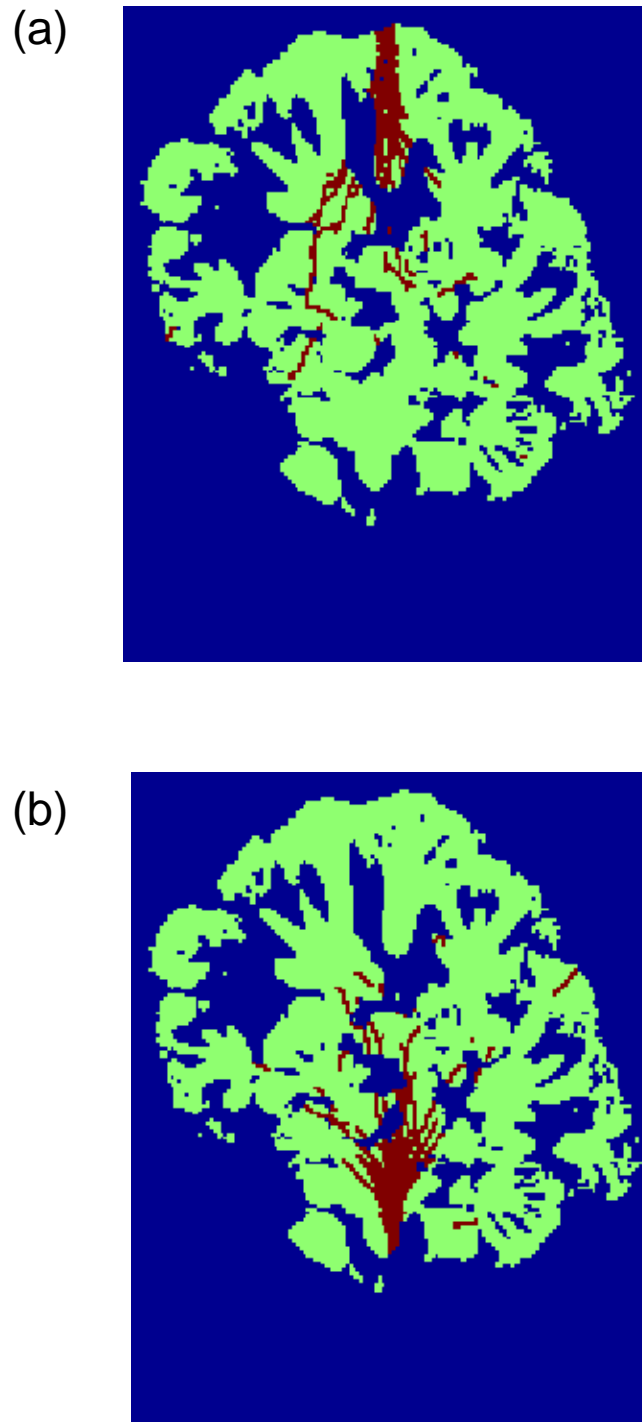


Fig. 7.15. Particle trajectories at 10 MeV electrons with 100 particle histories; (a) upper beam direction, (b) lower beam direction.

*C*, *H*, *O*, and *N* are the common elements of biological body tissue. Using the food irradiation database in this system, we can calculate the weight fractions of a variety of food products. Broccoli, for example, contains 4.5% of carbon, 10.5% of hydrogen, 83.9% of oxygen, and 0.5% of nitrogen by weight.

In the Tally Definition section, the cross section can be specified. For example, if the source is directed from the top to the bottom, a *x*-cross section shows a dose distribution at a plane along the beam direction and a *z*-cross section shows a dose distribution at a plane perpendicular to the beam direction (see Fig. 7.14).

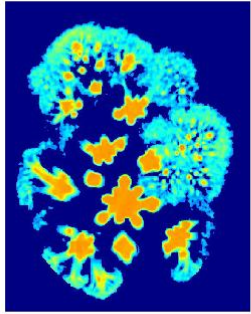
CT images of a bunch of broccoli were taken from the head to the stem with 5 mm thickness (Fig. 7.16). The CT scan images of the broccoli head show the compact cluster of flowers and the looser stems. The density (Fig. 7.17) of the flowery component ( $0.4 - 0.5 \text{ g/cm}^3$ ) of the head is much less than that of the stem ( $0.9 - 1.0 \text{ g/cm}^3$ ). The flower buds seem to be clustered compactly; however, air spaces are present, thus reducing the density values of the broccoli head.

### **7.6.2 Broccoli Output Visualization**

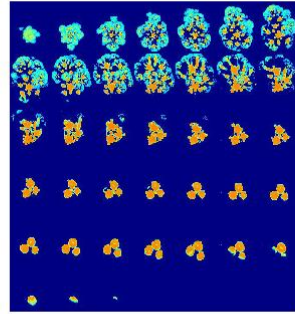
For the surface irradiation treatment using 1.35 MeV electron beams, the energy distribution at the broccoli head is strongly related to the electrons entrance angle and the sample's density (Fig. 7.18, upper left corner of). As the entrance angle increases, the electrons penetrate more and their energy is absorbed at that point, even though electrons inherently scatter easily. In addition, at the penetration points the relative error is relatively large (Fig. 7.18, upper right corner of), because the number of particles



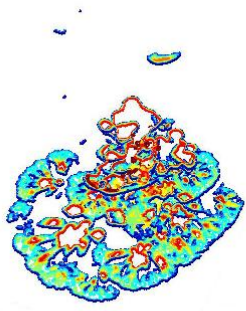
A CT Slice of Broccoli



CT Slice Deck of Broccoli



3D Contour Slices of Broccoli



Reconstructed 3D Geometry of Broccoli

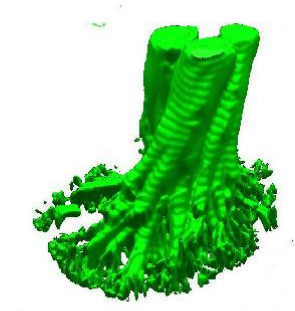


Fig. 7.16. Broccoli's CT scan images.

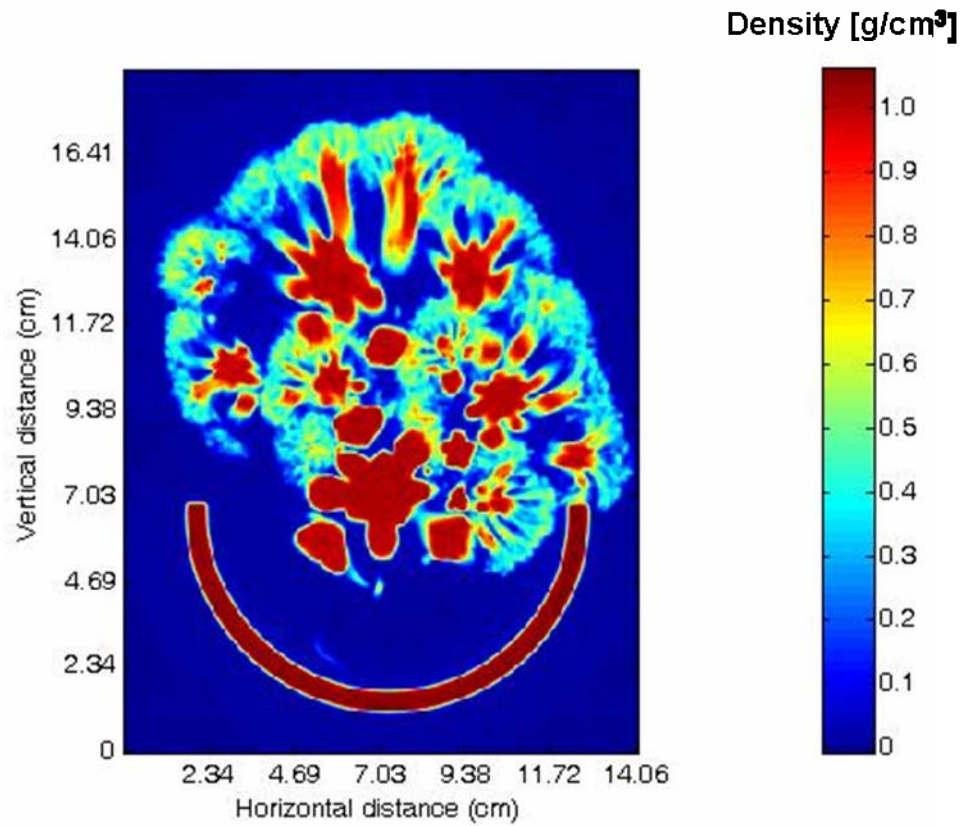


Fig. 7.17. Density distribution of a broccoli head.

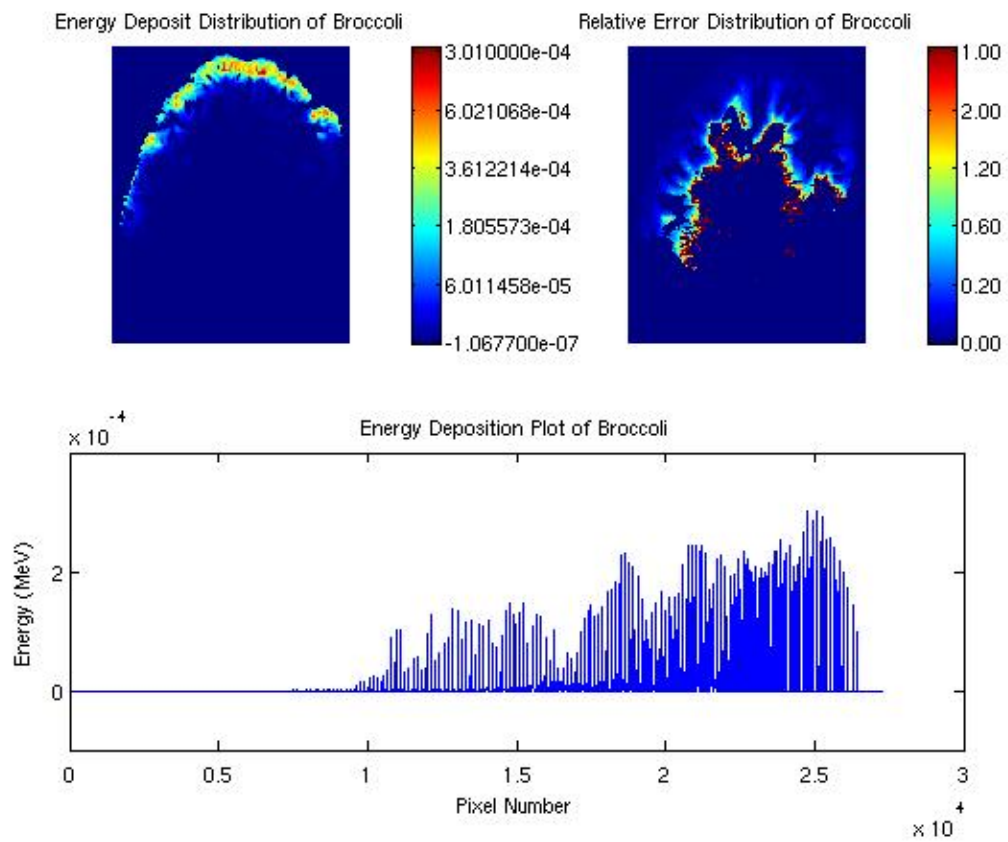


Fig. 7.18. Energy distribution around the broccoli head using 1.35 MeV electron source.

reaching the area is very small. The energy deposition plot (Fig. 7.18, bottom) represents the energy distribution around the broccoli head. The Pixel number at the  $x$ -axis was counted from the bottom to the top as illustrated in the energy deposition distribution plot (Fig. 7.18, bottom).

For a high-energy irradiation treatment using 10 MeV electrons (LINAC), the energy distribution at the head did not show a clear pattern because of its complex geometry (Fig. 7.19). The energy at the small stems attached to the flower head is relatively higher than the energy at the interior stem. Unlike the 1.35 MeV electrons source that provided only surface treatment (penetration less than 5 mm), the absorbed energy shown in this figure covered the whole broccoli head. The largest vertical distance the electrons penetrated in the broccoli head was about 9.8 cm, significantly longer than the normal penetration depth (4 cm) achieved with 10 MeV electrons in water (density of 1 g/cm<sup>3</sup>).

For X-rays treatment using a 5 MeV X-rays source, the absorbed energy at the stem component of the flowery head was higher than the values outside the flower buds (Fig. 7.20). Usually, when X-rays penetrate a surface, there is an energy buildup region near the incident surface, followed by exponential energy decay to greater depths (Attix, 1986). However, in the case, no buildup regions were present, because of the different interface densities in the flower head at the point of interaction.

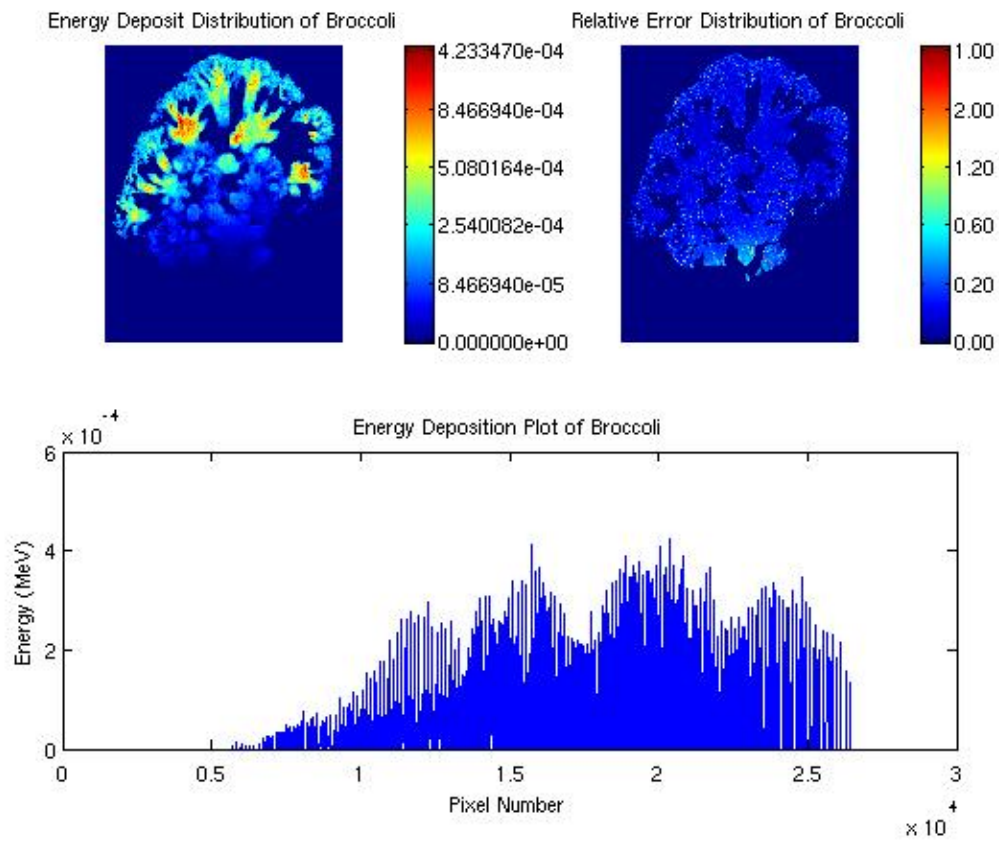


Fig. 7.19. Energy distribution around the broccoli head using 10 MeV electron source (LINAC).

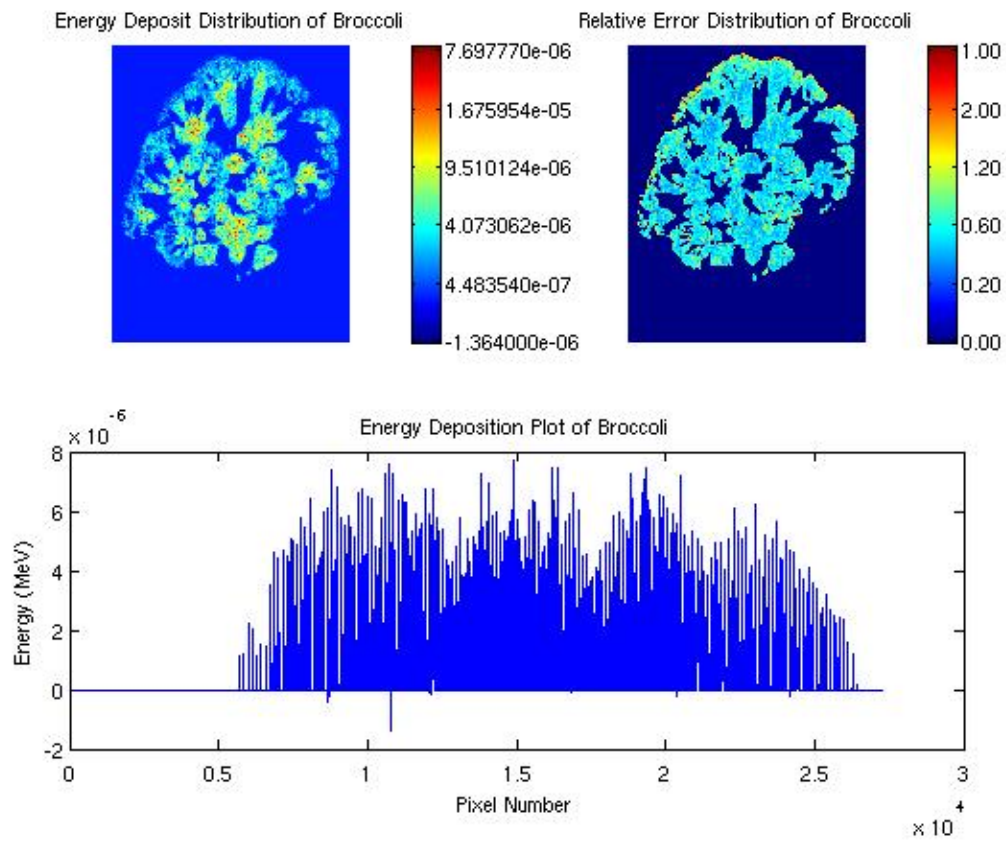


Fig. 7.20. Energy distribution around the broccoli head using 5 MeV X-rays source.

## 7.7 Conclusion

A Web-based information system was developed to enable flexible and reliable operations through the Internet by food irradiation engineers and researchers. The system provides data preparation, analysis, and interpretation for irradiation simulation of complex-shaped food products. A Web-based interface provides the on-line capability to formulate input data for the MCNP code and to visualize and analyze output data from the MCNP program. The integrated Matlab and Matlab Web Server programs scheme automatically obtain the data input to and the output from MCNP simulations. A database containing microbial decimal reduction  $D_{10}$ -values, food nutritional composition, and food quality attributes was built to support food irradiation analysis and research. This information system provides a powerful tool for irradiation simulation studies of complex-shaped foods.

## CHAPTER VIII

### CONCLUSIONS

A dose calculation methodology was developed to provide accurate 3-D dose distribution in complex-shaped food products using Monte Carlo simulation with CT scan technology. This methodology was validated with experimental dosimetry data using both an apple phantom and a chicken carcass at machine-generated radiation sources (1.35 and 10 MeV electron, and 5 MeV X-ray). A Web-based food irradiation information system was developed to provide a powerful tool for irradiation treatment of food products. The following conclusions are then obtained:

1. The apple phantom showed electron interaction characteristics very similar to an actual apple.
2. The measured and calculated dose distributions in the apple phantom showed good agreement, thus supporting the validity of using the simulation method and chemical phantom techniques for accurate planning of food irradiation treatments.
3. For a Lucite thickness of 3 cm (target dose of 1.0 kGy), the measured dose confirmed a uniform irradiation treatment at the top and bottom regions with a maximum dose of 1.3 kGy located at the top left region of the apple.
4. The simulated results predicted very well the dose distribution (5% discrepancy) measured in the apple phantom.



5. The geometric and composition CT data of a real apple was generated, by using the Monte Carlo code to simulate the dose distribution in an apple irradiated by 1 and 5 MeV photon beams.
6. For the 5 MeV photon simulations, a lesser amount of energy was deposited closer to the surface (at the right side surface) of the apple.
7. For 1 MeV simulation, a higher energy was distributed at the right half of the apple, and there was no warming-up region.
8. 3-D geometrical models of food products were developed with image processing techniques based on CT scan.
9. The 3-D geometric models strongly support effective Monte Carlo simulations for the accurate calculations of dose distribution on food products.
10. For low energy irradiation (1.35 MeV) treatment of a chicken carcass, dose absorption occurred up to 5-7 mm deep, so this treatment would result on surface irradiation of the carcass.
11. For high energy irradiation (10 MeV) treatment of a chicken carcass, two-sided (top and bottom) irradiation resulted in a dose uniformity ratio of about 1.6, which is within the acceptable range of most food irradiation treatments.
12. Although the chicken carcass is non-homogeneous (skin, bone, meat, and fat), the absorbed dose decreased continuously when exposed to 5 MeV X-rays.
13. The Web-based food irradiation information system provides data preparation, analysis, and interpretation for irradiation simulation of complex-shaped food products.

14. A Web-based interface provides the on-line capability to formulate input data for the MCNP code and to visualize and analyze output data from the MCNP code.
15. A database containing microbial decimal reduction  $D_{10}$  values, food nutritional composition, and food quality attributes was built to support food irradiation analysis and research.

**CHAPTER IX**  
**RECOMMENDATIONS FOR FURTHER STUDY**

The following are recommendations for future study.

1. Develop new phantom dosimetry materials to simulate the heterogeneous components of food products, e.g., bone, flesh, skin, and fat.
2. Search more effective and economical methods to obtain 3-D geometry, such as 3-D laser scan digitizer using reverse engineering technique.
3. Apply the radiation transport Monte Carlo code (GEANT4), used at nano scale simulation, to describe DNA destruction of pathogens in specific food products.
4. Generate food product's pathogen survival distribution, and quality (color, texture, etc.) distribution for irradiation treatments, using their relation with dose distribution.

## REFERENCES

- Agostinelli, S., Allison, J., Amako, K., Apostolakis, J., Araujo, H., Arce, P., et al. (2003). GEANT4 – a simulation toolkit. *Nuclear Instruments and Methods in Physics Research A*, 506, 250-303.
- Alva, H., Mercado-Uribe, H., Rodríguez-Villafuerte, M., & Brandan, M. E. (2002). The use of a reflective scanner to study radiochromic film response. *Physics in Medicine and Biology*, 47, 2925-2933.
- Andreo, P. (1991). Monte Carlo technique in medical physics *Phys. Med. Biol.*, 36, 861-920.
- ASTM (2002a). ASTM Standards E1441: Standard guide for computed tomography (CT) imaging. *Annual Book of ASTM Standards*, West Conshohocken, PA: ASTM International.
- ASTM (2002b). ASTM Standards E2232: Standard guide for selection and use of mathematical methods for calculating absorbed dose in radiation processing applications. *Annual Book of ASTM Standards*, West Conshohocken, PA: ASTM International.
- ASTM (2002c). ISO/ASTM 51262: Standard guide for selection and calibration of dosimetry systems for radiation processing. *Annual Book of ASTM Standards*, West Conshohocken, PA: ASTM International.

- ASTM (2002d). ISO/ASTM 51607: Standard practice for use of the Alanine-EPR dosimetry system. *Annual Book of ASTM Standards*, West Conshohocken, PA: ASTM International.
- ASTM (2003). ASTM Standards E2303: Standard guide for absorbed-dose mapping in radiation processing facilities. *Annual Book of ASTM Standards*, West Conshohocken, PA: ASTM International.
- Attix, F. H. (1986). *Introduction to Radiological Physics and Radiation Dosimetry*. New York: John Wiley & Sons.
- Aydarous, A. S., Darley, P. J., & Charles, M. W. (2001). A wide dynamic range, high-spatial-resolution scanning system for radiochromic dye films. *Physics in Medicine and Biology*, 46, 1379-1389.
- Barcelon, E. G., Tojo, S., & Watanabe, K. (1999). X-ray CT imaging and quality detection of peach at different physiological maturity. *Transactions of the ASAE*, 42(2), 435-441.
- Baro, J., Sempau, J., Fernandez-Varea, J. M., & Salvat, F. (1995). PENELOPE: An algorithm for Monte Carlo simulation of the penetration and energy loss of electrons and positrons in matter. *Nuclear Instruments and Methods in Physics Research B*, 100, 31-46.
- Berger, M. J. (1963). Monte Carlo calculation of the penetration and diffusion of fast charged particles. In B. Alder, S. Fernbach, & M. Rotenberg (Eds.), *Methods in Computational Physics*. New York: Academic Press.

- Berger, M.J. & Wang, R. (1988). Multiple-scattering angular deflections and energy loss straggling. In T. M. Jenkins, W. R. Nelson, & A. Rindi (Eds.), *Monte Carlo Transport of Electrons and Photons*. New York: Plenum Press.
- Bethe, H. A. & Heitler, W. (1934). On the stopping of fast particles and on the creation of positive electrons. *Proceedings of the Royal Society of London. Series A, Containing Papers of a Mathematical and Physical Character*, 146, 83-112.
- Beuchat, L. R. (1996). Pathogenic microorganisms associated with fresh produce. *J. Food Protection* 59, 204-216.
- Beuchat, L. R. (1998). Surface decontamination of fruits and vegetables eaten raw: a review. *Report to FAO and WHO*, University of Georgia, Griffin, GA. Center for Food Safety and Quality Enhancement.
- Bielajew, A. F. (2001). *Fundamentals of the Monte Carlo method for neutral and charged particle transport*. <http://www-personal.engin.umich.edu/~bielajew>.
- Borisov, N., Franck, D., de Carlan, L., & Laval, L. (2002). A new graphical user interface for fast construction of computation phantoms and MCNP calculations: application to calibration of in vivo measurement systems. *Health Physics*, 83(2), 272-279.
- Borsa, J., Chu, R., Sun, J., Linton, N., & Hunter, C. (2002). Use of CT scans and treatment planning software for validation of the dose component of food irradiation protocols. *Radiation Physics and Chemistry*, 63, 271-275.

- Börsch-Supan, W. (1961). On the evaluation of the function  $\phi(\lambda) = \frac{1}{2\pi i} \int_{\sigma-i\infty}^{\sigma+i\infty} e^{\mu \ln \mu + \lambda \mu} d\mu$  for real values of  $\lambda$ . *Journal of Research of the National Institute of Standards and Technology*, 65B, 245.
- Braby, L. (2004). Personal communication. Department of Nuclear Engineering, Texas A&M University. College Station, TX.
- Brecht, J. K., Shewfelt, R. L., Garner, J. C., & Toller, E. W. (1991). Using X-ray computed tomography (X-ray CT) to nondestructively determine maturity of green tomatoes. *HortScience*, 26, 45-47.
- Brescia, G., Moreira, R., Braby, L., & Castell-Perez, E. (2003). Monte Carlo simulation and dose distribution of low energy electron irradiation of an apple. *Journal of Food Engineering*, 60, 31-39.
- Brown, F. B. (2003). *MCNP-A General Monte Carlo N-Particle Transport Code, Version 5*. Los Alamos National Laboratory, Oak Ridge, TN.
- Burnett, S. L., Chen, J., & Beuchat, L. R. (2000). Attachment of *Escherichia coli* O157:H7 to the surfaces and internal structures of apples as detected by confocal scanning laser microscopy. *Applied and Environmental Microbiology*, 66(11), 4679-4687.
- Cashwell, E. D., & Everett, C. J. (1959). *A Practical Manual on the Monte Carlo Method for Random Walk Problem*. New York: Pergamon Press.
- CDC (Centers for Disease Control and Prevention) (1996). Outbreaks of *Escherichia coli* O157:H7 infection associated with drinking unpasteurized commercial apple

juice — British Columbia, California, Colorado, and Washington, October 1996.

*Morbidity and Mortality Weekly Report*, 45(44), 975.

CDC (Centers for Disease Control and Prevention) (1997). Outbreaks of *Escherichia coli* O157:H7 infection and cryptosporidiosis associated with drinking unpasteurized apple cider — Connecticut and New York, October 1996. *Morbidity and Mortality Weekly Report*, 46(01), 4-8.

Chilton, A. B., Shultis, J. K., & Faw, R. E. (1984). *Principles of Radiation Shielding*, Englewood Cliffs, New Jersey: Prentice-Hall, Inc.

Cleland, M. R., Lisanti, T. F., & Galloway, R. A. (2004). Comparisons of Monte Carlo and ICRU electron vs. range equations. *Radiation Physics and Chemistry*, 71, 583-587.

Cody, S. H., Glynn, M. K., Farrar, J. A., Cairns, K. L., Griffin, P. M., Kobayashi, J., et al. (1999). An outbreak of *Escherichia coli* O157:H7 infection from unpasteurized commercial apple juice. *Annals of Internal Medicine*, 130(3), 202-209.

Cunningham, I. A., & Judy, P. F. (2003). Computed tomography. In K. M. Mudry, R. Plonsey, & J. D. Bronzino (Eds.), *Biomedical Imaging*. New York: CRC Press.

Datta, R. P., Altekar, S. D., Ray, A. K., & Morel, J. E. (1996). Computational model for coupled electron-photon transport in two dimensions. *Physical Review E*, 53(6), 6514-6522.

Davies, H., Bethe, H. A., & Maximon, L. C. (1954). Theory of bremsstrahlung and pair production. II. Integral cross section for pair production. *Physical Review*, 93, 788-795.



- DeMarco, J. J., Sloberg, T. D., & Smathers, J. B. (1998). A CT-based Monte Carlo simulation tool for dosimetry planning and analysis. *Medical Physics*, 25(1), 1-11.
- Drumm, C. R. (1997). Multidimensional electron-photon transport with standard discrete ordinates codes. *Nuclear Science and Engineering*, 127, 1-21.
- Drumm, C. R., Fan, W. C., & Renken, J. H. (1991). Forward and adjoint methods and applications for deterministic electron-photon transport. *Nuclear Science and Engineering*, 108, 16-49.
- Evans, J. F., Blue, T., Gupta, N. (2001). Absorbed dose estimates to structures of the brain and head using a high-resolution voxel-based head phantom. *Medical Physics*, 28(5), 780-786.
- FAO/IAEA. (1995). *Consultant Meeting on the Development of X-ray Machines for Food Irradiation*. Vienna, Food and Agriculture Organization (FAO)/International Atomic Energy Agency (IAEA).
- Finney, E. E., & Noris, K. H. (1978). X-rays scans for detecting hollow heart in potatoes. *American Potato Journals*, 55, 95-105.
- Forster, R. A., Little, R. C., Briesmeister, J. F., & Hendricks, J. S. (1990). MCNP capabilities for nuclear well logging calculations. *IEEE Transactions on Nuclear Science*, 37(3), 1378-1385.
- Fu, K. S., Gonzalez, R. C., & Lee, C. S. G. (1987). *Robotics: Control, Sensing, Vision, and Intelligence*. New York: McGraw-Hill.
- Garth, J. C. (1989). Calculations of dose enhancement in device structures. *Nuclear Instruments and Methods in Physics Research B*, 40, 1266-1270.

- Goudsmit, S., & Saunderson, J. L. (1940). Multiple scattering electrons. *Physical Review*, 57, 24-29.
- Graves, M., Smith, A., & Batchelor, B. (1998). Approaches to foreign body detection in foods. *Trends in Food Science & Technology*, 9, 21-27.
- Halbleib, J. A. (1999). *RSICC Computer Code Collection, ITS 3.0. Integrated TIGER Series of Coupled Electron/Photon*. Oak Ridge National Laboratory, Oak Ridge, TN.
- Halbleib, J. A., Kensek, R. P., Valdez, G. D., Seltzer, S. M., & Berger, M. J. (1992). ITS: The integrated TIGER series of electron/photon transport codes – version 3.0. *IEEE Transactions on Nuclear Science*, 39(4), 1025-1030.
- Hallman, G. J., & Martinez, L. R. (2001). Ionizing irradiation quarantine treatment against Mexican fruit fly (Diptera: Tephritidae) in citrus fruits. *Postharvest Biology and Technology*, 23, 71-77.
- Han, Y. J., Bowers, S. V., & Dodd, R. B. (1992). Nondestructive detection of split-pit peaches. *Transactions of the ASAE*, 35(6), 2063-2067.
- Haug, E. (1975). Bremsstrahlung and pair production in the field of free electrons. *Z. Naturforsch*, 30, 1099.
- Hellborg, R. (2005). *Electrostatic Accelerators: Fundamentals and Applications*. New York: Springer.
- High Voltage Engineering Corporation. (1954). *Instruction Manual HVI-42 for the Van de Graaff high voltage accelerator: Type AK, Model S, 2 MeV electron accelerator*, Cambridge, MA

- Hogstrom, K. R., Mills, M. D., & Almond, P. R. (1981). Electron beam dose calculations. *Physics in Medicine and Biology*, 26, 445-459.
- Hounsfield, G. N. (1980). Nobel award address: computed medical imaging. *Medical Physics*, 7(4), 283-290.
- Hsieh, J. (2003). *Computed Tomography: Principles, Design, Artifacts, and Recent Advances*. Bellingham, WA: SPIE Press.
- ICRU. (1984). *Radiation Dosimetry: Electron Beams with Energies Between 1 and 50 MeV*. Bethesda, MD: International Commission on Radiation Units and Measurements, Report No. 35.
- ICRU. (1989). *Tissue Substitutes in Radiation Dosimetry and Measurement*. Bethesda, MD: International Commission on Radiation Units and Measurements, Report No. 44.
- Ito, A. (1987). Three-dimensional dose calculation for total body irradiation. In T. M. Jenkins, W. R. Nelson, & A. Rindi (Eds.), *Monte Carlo Transport of Electrons and Photons* (pp. 573-598). New York: Plenum Press.
- Janicki, C., & Seuntjens, J. (2004). Accurate determination of dose-point-kernel functions close to the origin using Monte Carlo simulations. *Medical Physics*, 31(4), 814-818.
- Janicki, C., Duggan, D. M., & Rahdert, D. A. (2001). A dose-point-kernel model for a low energy gamma-emitting stent in a heterogeneous medium. *Medical Physics*, 28(7), 1397-1405.

- Jun, S., & Puri, V. M. (2004). Development of interactive computational model of temperature and moisture distribution of microwaved foods. *Applied Engineering in Agriculture*, 20(5), 677-682.
- Keagy, P. M., Parvin, B., & Schatzki, T. F. (1996). Machine recognition of naval orange worm damage in X-ray images of pistachio nuts. *LWT-Food Science and Technology*, 29, 140-145.
- Khan, F. M. (1984). *The Physics of Radiation Therapy*. Baltimore: Williams & Wilkins.
- Kim, J., Moreira, R. G., Huang, Y., & Castell-Perez, M.E. (2007). 3-D dose distributions for optimum radiation treatment planning of complex foods. *Journal of Food Engineering*, 79, 312-321.
- Kim, J., Moreira, R. G., Rivadeneira, R., & Castell-Perez, M. E. (2006a). Monte Carlo-based food irradiation simulator. *Journal of Food Process Engineering*, 29(1), 72-88.
- Kim, J., Rivadeneira, R. G., Castell-Perez, M. E., & Moreira, R. G. (2006b). Development and validation of a methodology for dose calculation in electron beam irradiation of complex-shaped foods. *Journal of Food Engineering*, 74, 359-369.
- Koch, H. W., & Motz, J. W. (1959). Bremsstrahlung cross-section formulas and related data. *Reviews of Modern Physics*, 31(4), 920-955.
- Lammertyn, J., Jancsok, P., Dresselaers, T., Van Hecke, P., Wevers, M., De Baerdemaeker, J., et al. (2001). X-ray CT and magnetic resonance imaging to study the development of core breakdown in 'Conference' pears. Presented at the ASAE International Meeting, Sacramento, CA, June 2001. ASAE Paper 016037.

- Landau, L. (1944). On the energy loss of fast particles by ionization. *Journal of Physics, USSR*, 8, 201.
- Lisanti, T. F. (2004). Calculating electron range values mathematically. *Radiation Physics and Chemistry*, 71, 579-582.
- Loaharanu, P. (1995). Food irradiation: current status and future prospects. In *New Methods of Food Preservation*. G. W. Gould (Ed.). New York: Blackie Academic & Professional.
- Lorence, L. J. (1992). CEPXS/ONELD Version 2.0: A discrete ordinates code package for general one-dimensional coupled electron-photon transport. *IEEE Transactions on Nuclear Science*, 39(4), 1031-1034.
- Lorensen, W. E., & Cline, H. E. (1987). Marching cubes: a high resolution 3D surface construction algorithm. *Proceedings of ACM SIGGRAPH*, 163-170.
- Mackie, T. R. (1990). Applications of the Monte Carlo method in radiotherapy. In K. Kase, B. Bjarngard, & F. H. Attix (Eds.), *Vol. III of Dosimetry of Ionizing Radiation*. New York: Academic Press.
- McKeown, J., Armstrong, L., Cleland, M. R., Drewell, N. H., Dubeau, J., Lawrence, C. B. et al. (1998). Photon energy limits for food irradiation: a feasibility study. *Radiation Physics and Chemistry*, 53, 55-61.
- McLaughlin, W. (1970). Film, radiochromic dye-cyanide dosimeters, In N. W. Holm, & R. J. Berry (Eds.), *Manual on Radiation Dosimetry*. New York: Marcel Dekker.

- McLaughlin, W. L., Jarrett, R. D., & Olejuik, T. A. (1982). Dosimetry, In E. S. Josephson, & M. S. Peterson (Eds.). *Preservation of Food by Ionizing Radiation* (Vol. I). Boca Raton, FL: CRC Press.
- Meissner, J., Abs, M., Cleland, M. R., Herer, A. S., Jongen, Y., Kuntz, F. et al. (2000). X-ray treatment at 5 MeV and above. *Radiation Physics and Chemistry*, 57, 647-651.
- Miller, R. B. (2003). Food irradiation using bremsstrahlung X-rays. *Radiation Physics and Chemistry*, 68, 963-974.
- Miller, R. B. (2005). *Electronic Irradiation of Foods: An Introduction to the Technology*. New York: Springer.
- Miller, A., Batsberg, W., & Karman, W. (1988). A new radiochromic thin-film dosimeter system. *Radiation Physics and Chemistry*, 31, 491-496.
- Mittendorfer, J., Colon, M., & Gratzel, F. (2004). Monte Carlo methods for process development and control in electron beam technology. In *Emerging applications of radiation processing*, Vienna, Austria.
- Mohsenin, N. N. (1986). *Physical Properties of Plant and Animal Materials*. Second Edition, New York: Gordon and Breach Science Publishers.
- Molière, G. (1947). Theorie der streuung schneller geladener teilchen I: Einzelstreuung am abgeschirmten Coulomb-Feld. *Z. Naturforsch*, 2a, 133.
- Møller, C. (1932). Zur Theorie des Durchgangs schneller Elektronen durch Materie. *Ann. Physik*, 14, 531-585.
- Morehouse, K. M. (2002). Food irradiation – US regulatory considerations. *Radiation Physics and Chemistry*, 63, 281-284.

- Mott, N. F. (1929). The scattering of fast electrons by atomic nuclei. *Proceedings of the Royal Society of London. Series A, Containing Papers of a Mathematical and Physical Character*, 124, 425-442.
- Murano, E. A. (1995). Irradiation of fresh meats. *Food Technology*, 49(5), 52.
- Nahum, A. E. (1985). The Computation of Dose Distribution in Electron Beam Radiotherapy, University of Umea, S-901 85 Umea, Sweden.
- NCRP. (2003). *Radiation protection for particle accelerator facilities: recommendations of the National Council on Radiation Protection and Measurements*. Bethesda, MD: National Council on Radiation Protection & Measurements, Report No. 144.
- Nelson, W. R., Hirayama, H., & Rogers, D. W. O. (1985). *The EGS4 Code System*. Stanford, CA: Stanford Linear Accelerator Center.
- Olsen, H. (1955). Outgoing and ingoing waves in final states and bremsstrahlung. *Physical Review*, 99, 1335-1336.
- Oppelt, A. (2005). *Imaging Systems for Medical Diagnostics*. Erlangen, Germany: Publics Corporate Publishing.
- Pawlicki, T., & Ma, C. M. (2000). Effects of CT streaking artifacts in Monte Carlo dose distributions for head and neck cancer. In *Proceedings of the 13<sup>th</sup> International Conference on the Use of Computers in Radiotherapy (Heidelberg)* (pp. 414-416). Springer, Berlin.
- Peiris, K. H. S., Dull, G. G., Leffler, R. G., Burns, J. K., Thai, C. N., & Kays, S. J. (1998). Nondestructive detection of section drying, an internal disorder in tangerine. *HortScience*, 33(2), 310-312.

- Piña-Villalpando, G., & Sloan, D. P. (1998). Dose distribution studies of a gamma industrial irradiator using PC code. *Radiation Physics and Chemistry*, 52, 563-567.
- Plante, I. L., Filali-Mouhim, A., & Jay-Gerin, J. (2005). SimulRad: a Java interface for a Monte-Carlo simulation code to visualize in 3D the early stages of water radiolysis. *Radiation Physics and Chemistry*, 42(10), 917-941.
- Podgorsak, E. B., Rawlinson, J. A., & Johns, H. E. (1975). X-ray depth doses from linear accelerators in the energy range from 10 to 32 MeV. *American Journal of Roentgenology*, 123, 182-191.
- Potsaid, M. S. (1963). Dosimeters, solid "phantom". In G. L. Clark (Ed.), *The Encyclopedia of X-rays and Gamma rays* (pp. 279-289). New York: Reinhold Publishing Corporation.
- Pratt, R. H., Tseng, H. K., Lee, C. M., Kissel, L., MacCallum, C., & Riley, M. (1977). Bremsstrahlung energy spectra from electrons of kinetic energy  $1 \text{ keV} \leq T_1 \leq 2000 \text{ keV}$  incident on neutral atoms  $2 \leq Z \leq 92$ . *Atomic Data and Nuclear Data Tables*, 20(2), 175-209.
- Rakhno, I. L., & Roginets, L. P. (1998). Dose field simulation for products irradiated by electron beams: formulation of the problem and its step by step solution with EGS4 computer code. In *Techniques for High Dose Dosimetry in Industry, Agriculture and Medicine*, Vienna, Austria: International Atomic Energy Agency (IAEA).
- Regulla, D. F., & Deffner, U. (1982). Dosimetry by electron-spin-resonance spectroscopy of alanine. *International Journal of Applied Radiation and Instrumentation*, 33, 1101-1114.



- Rivadeneira, R. (2004). Development of a chemical dosimeter for electron beam food irradiation. MS Thesis. Texas A&M University, College Station, TX.
- Rutherford, E. (1911). The scattering of  $\alpha$  and  $\beta$  particles by matter and the structure of the atom. *Philosophical Magazine*, 21, 669.
- Salvat, F., Fernandez-Varea, J. M., Acosta, E., & Sempau, J. (2001). *Penelope – A code system for Monte Carlo simulation of electron and photon transport* (pp. 149-171). OECD Nuclear Energy Agency Data Bank, Issy-les-Moulineaux, France.
- Scharf, W. H. (1994). *Biomedical particle accelerators* (pp. 52-64). Woodbury. New York.
- Schatzki, T. F., Witt, S. C., Wilkins, D. E., & Lenker, D. H. (1981). Characterization of growing lettuce from density contours – I. Head selection. *Pattern Recognition*, 13(5), 333-340.
- Seltzer, S. M. (1988a). Cross sections for Bremsstrahlung production and electron-impact ionization. In T. M. Jenkins, W. R. Nelson, & A. Rindi (Eds.), *Monte Carlo Transport of Electrons and Photons*. New York: Plenum Press.
- Seltzer, S. M. (1988b). An overview of ETRAN Monte Carlo methods. In T. M. Jenkins, W. R. Nelson, & A. Rindi (Eds.), *Monte Carlo Transport of Electrons and Photons*. New York: Plenum Press.
- Seltzer, S. M. (1991). Electron-photon Monte Carlo calculations: The ETRAN code. *Applied Radiation and Isotopes*, 42(10), 917-941.

- Seltzer, S. M., & Berger, M. J. (1985). Bremsstrahlung spectra from electron interactions with screened atomic nuclei and orbital electrons. *Nuclear Instruments and Methods in Physics Research B*, 12, 95-134.
- Shahin, M. A., Tollner, E. W., & Prussia, S. E. (1999). Filter design for optimal feature extraction from X-ray images. *Transactions of the ASAE*, 42(6), 1879-1887.
- Sonega, L., Ben-Arie, R., Raynal, J., & Pech, J. C. (1995). Biochemical and physical evaluation of textural characteristics of nectarines exhibiting woolly breakdown: NMR imaging, X-ray computed tomography and pectin composition. *Postharvest Biology and Technology*, 5, 187-198.
- Stenger, V., Halmavánszki, J., Falvi, L., Fehér, I., & Demirizen, Ü. (1998). Dose planning, dosimeter reading and controls using PC for gamma radiation facility. In *Techniques for High Dose Dosimetry in Industry, Agriculture and Medicine*, Vienna, Austria: International Atomic Energy Agency (IAEA).
- Sternhemier, R. M., & Peierls, R. F. (1971). General expression for the density effect for the ionization loss of charged particles. *Physical Review B*, 3(1), 3681-3692.
- Stichelbaut, F., Bol, J. L., Cleland, M. R., Grégoire, O., Herer, A. S., Jongen, Y. et al. (2004a). The Palletron<sup>TM</sup>: a high-dose uniformity pallet irradiator with X-rays. *Radiation Physics and Chemistry*, 71, 289-293.
- Stichelbaut, F., Bol, J. L., Lundhal, B., Martin, F., Rose, G., Schlecht, J. et al. (2004b). X-ray dosimetry: comparing Monte Carlo simulations and experimental data. *Radiation Physics and Chemistry*, 71, 343-347.

- Tabata, T., Andreo, P., & Shinoda, K. (1996). An analytical formula for the extrapolated range of electrons in condensed materials. *Nuclear Instruments and Methods in Physics Research B*, 119, 463-470.
- Tabata, T., Ito, R., Kuriyama, I., & Moriuchi, Y. (1989). Simple method of evaluating absorbed dose in electron-beam processing. *Radiation Physics and Chemistry*, 33(5), 411-416.
- Tan, D., & Heaton, B. (1994). Simple empirical relations for electron CSDA range and electron energy loss. *Applied Radiation and Isotopes*, 45(4), 527-528.
- Tollner, E. W., Hung, Y. C., Upchurch, B. L., & Prussia, S. E. (1992). Relating X-ray absorption to density and water content in apples. *Transactions of the ASAE*, 35(6), 1921-1928.
- Tsoufanidis, N. (1995). *Measurement and Detection of Radiation*. Taylor & Francis. New York.
- USDA (1999). Economic Research Service. *Fruit and Tree Nuts Situation and Outlook Report*. Washington, DC, March 1999.
- USDA (October 23, 2006). <http://www.nal.usda.gov/fnic/foodcomp/search>.
- USDA ARS (May 21, 2007). <http://ars.usda.gov/Services/docs.htm?docid=6786>, United States Department of Agriculture Agricultural Research Service (USDA ARS).
- Van Riper, K. A. (2005). A CT and MRI scan to MCNP input conversion program. *Radiation Protection Dosimetry*, 115, 513-516.

- Vazquez-Polo, G., Valdivia, H. L., Abrego, H. C., Mijangos, R. R., & Garcia, R. G. (2002). Calculation of absorbed dose of low-energy electron beam by and approximation method. *Radiation Physics and Chemistry*, 64, 181-187.
- Wan, Y. N., Lin, C. M., & Chiou, J. F. (2002). Rice quality classification using an automatic grain quality inspection system. *Transactions of the ASAE*, 45(2), 379-387.
- Wang, D., Fon, D., Fang, W. (2002). Development of simulation software regarding air properties and grain drying using MATLAB. Presented at the ASAE International Meeting, Chicago, IL, July 2002. ASAE Paper 026117.
- Wilson, E. J. (2001). *An Introduction to Particle Accelerators*. New York: Oxford University Press.
- Yoriyaz, H., Santos, A. D., Stabin, M. G., & Cabezas, R. (2000). Absorbed fractions in a voxel-based phantom calculated with the MCNP-4B code. *Medical Physics*. 27(7), 1555-1562.
- Zhao, M., Moy, J., & Paul, R. E. (1996). Effects of gamma-irradiation on ripening papaya pectin. *Postharvest Biology and Technology*, 8, 209-222.

## APPENDIX A

### A.1 Matlab Script File for Reading CT Data

```
%
% ***** CTImChk_brcl01.m *****
%
% Script file which can check broccoli CT data
%
%
% Tuesday, 01/28/04
%
%
% Open CT data

fid=fopen('Broccoli.raw','r'); % Open CT raw data file
data=fscanf(fid,'%d'); % Read its data

% Extracting CT number

data1=reshape(data,4,4718592); % 18*512*512

data2=data1(4,:);

data3=reshape(data2,18,512,512);

% Presenting CT image

slice_number = 9;

data4=squeeze(data3(slice_number,:,:));

figure, imagesc(data4);

axis image;
```

## A.2 Matlab File for 3D Visualization

```
%  
% CT_3D_vis02.m => 3D Visualization of CT data  
%  
%           Thursday, 02/08/07  
%  
  
for findex=1:25  
    name='sl';  
    extension='.dat';  
    input_file_name=strcat(name,num2str(findex),extension);  
  
    fid=fopen(input_file_name,'r');  
    data=fscanf(fid,'%d');  
  
    data_a(:,:,findex)=reshape(data,221,373);  
  
end  
  
D1 = smooth3(data_a);  
  
D = D1(221:-1:1, :, :);  
  
[x y z D] = subvolume(D, [nan nan nan nan nan nan]);  
  
p = patch(isosurface(x,y,z,D, 5), 'FaceColor',[0.957, 0.3951, 0.1152],  
    ...  
    'EdgeColor','none');  
p2 = patch(isocaps(x,y,z,D, 5), 'FaceColor','interp','EdgeColor', ...  
    'none');  
  
colormap('default');  
  
view(3); axis tight; daspect([1 1 .14])  
  
camlight; lighting gouraud  
  
isonormals(x,y,z,D,p);
```

## APPENDIX B

### B.1 Matlab Script File for Generating Rotation Matrix

```

%
% tr02.m => Script file for a rotation of alpha angle
%           about x axis followed by a rotation of beta
%           angle about r axis (z')
%
%           Tuesday, 06/08/04

clear;

% Rotation of alpha angle about x axis (CCW)

Alpha = 37.5*pi/180;

% R axis (Rx, Ry, Rz)

R_x = 0;
R_y = -sin(37.5*pi/180);
R_z = cos(37.5*pi/180);

% Rotation angle about new z axis

Theta = 0;           % degree

% Center point

C_x = -0.25;
C_y = -0.0351563;
C_z = 0;

Thetal = Theta*pi/180;           % Changed to radian

% If the vector is not a unit vector, we need to normalize
% it and find its components along the principals axes

SqR = (R_x^2 + R_y^2 + R_z^2)^(0.5);

r_x = R_x / SqR;
r_y = R_y / SqR;
r_z = R_z / SqR;

V_theta = 1 - cos(Thetal);
S_theta = sin(Thetal);
C_theta = cos(Thetal);

% Calculate Transform matrix (3x3)

R11 = r_x^2 * V_theta + C_theta;

```

```

R12 = r_x * r_y * V_theta + r_z * S_theta;
R13 = r_x * r_y * V_theta - r_y * S_theta;
R21 = r_x * r_y * V_theta - r_z * S_theta;
R22 = r_y^2 * V_theta + C_theta;
R23 = r_y * r_z * V_theta + r_x * S_theta;
R31 = r_x * r_z * V_theta + r_y * S_theta;
R32 = r_y * r_z * V_theta - r_x * S_theta;
R33 = r_z^2 * V_theta + C_theta;

% Calculate Transform matrix Rx,30

X11 = 1;
X12 = 0;
X13 = 0;
X21 = 0;
X22 = cos(Alpha);
X23 = sin(Alpha);
X31 = 0;
X32 = sin(Alpha) * (-1);
X33 = cos(Alpha);

% Making transformation matrix

R = [ R11 R12 R13; R21 R22 R23; R31 R32 R33];
R1 = R';

X = [ X11 X12 X13; X21 X22 X23; X31 X32 X33];
X1 = X';

TR = R1 * X1;

C1 = [ C_x C_y C_z];
C2 = C1';

C3 = TR * C2;

% Saving transformation matrix

fod = fopen('Trmatrix','w');

fprintf(fod,'New center point\n');

fprintf(fod,'% .9f\n',C3);

fprintf(fod,'\n');

fprintf(fod,'R11');

```



```
fprintf(fod, ' %.9f\n', TR(1,1));

fprintf(fod, 'R12');
fprintf(fod, ' %.9f\n', TR(2,1));

fprintf(fod, 'R13');
fprintf(fod, ' %.9f\n', TR(3,1));

fprintf(fod, 'R21');
fprintf(fod, ' %.9f\n', TR(1,2));

fprintf(fod, 'R22');
fprintf(fod, ' %.9f\n', TR(2,2));

fprintf(fod, 'R23');
fprintf(fod, ' %.9f\n', TR(3,2));

fprintf(fod, 'R31');
fprintf(fod, ' %.9f\n', TR(1,3));

fprintf(fod, 'R32');
fprintf(fod, ' %.9f\n', TR(2,3));

fprintf(fod, 'R33');
fprintf(fod, ' %.9f\n', TR(3,3));

fclose(fod);
```

## B.2 MCNP Input File for Wax Apple Simulation

```

CT voxel test: New Wax Apple (mwap32 Wednesday, 09/21/05)
C
C mwap32 =>voxel structure of Wax Apple
C
C     - Using 'nwap42' and 'xrap42'
C
C     - x (-7:8)
C     - 5 MeV X-ray simulation (Upper direction)
C       => mode:e p
C     - Using px,py, and pz, instead of rpp
C     - Y direction source area has been corrected
C
C     - Tally
C       : *f8:e,p x(1:1)
C     - Fixing x=0 geometry data
C
C     - NPS = 1e6
C
C cell cards
C
1  0 -7
   lat=1 fill=-7:8 -53:53 -57:58
   100 100 100 100 100 100 100 100 100 100 100 100 100 100 100 100
   100 100 100 100 100 100 100 100 100 100 100 100 100 100 100 100
   100 100 100 100 100 100 100 100 100 100 100 100 100 100 100 100
   100 100 100 100 100 100 100 100 100 100 100 100 100 100 100 100
   100 100 100 100 100 100 100 100 100 100 100 100 100 100 100 100
   100 100 100 100 100 100 100 100 100 100 100 100 100 100 100 100
   100 100 100 100 100 100 100 100 100 100 100 100 100 100 100 100
   100 100 100 100 100 100 100 100 100 100 100 100 100 100 100 100
   100 100 100 100 100 100 100 100 100 100 100 100 100 100 100 100
   100 100 100 100 100 100 100 100 100 100 100 100 100 100 100 100
   100 100 100 100 100 100 100 100 100 100 100 100 100 100 100 100
   .....
   100 100 100 100 100 100 100 100 176 181 100 100 100 100 100
   100 100 100 100 100 100 100 100 100 242 257 100 100 100 100
   100 100 100 100 100 100 100 100 211 226 291 298 173 100 100
   100 100 100 100 100 100 100 100 206 275 277 303 303 199 100
   100 100 100 100 100 100 100 100 100 246 300 299 303 303 225
   100 100 100 100 100 100 100 100 100 100 276 303 303 303 303
   249 100 100 100 100 100 100 100 100 100 100 294 303 303 303
   303 270 100 100 100 100 100 100 100 100 100 100 302 302 302
   303 303 289 100 100 100 100 100 100 100 100 100 177 303 302
   303 303 303 300 100 100 100 100 100 100 100 100 100 190 303
   303 302 303 303 303 100 100 100 100 100 100 100 100 100 206
   303 302 302 303 303 303 100 100 100 100 100 100 100 100 100
   223 303 302 303 303 303 303 180 100 100 100 100 100 100 100
   100 239 302 302 302 303 303 303 196 100 100 100 100 100 100

```



```

1136 1 -0.869343 -20 u=304 imp:p,e=1
1137 1 -0.873644 -20 u=305 imp:p,e=1
1138 1 -0.877944 -20 u=306 imp:p,e=1
1187 2 -0.001124 -20 u=100 imp:p,e=1
1188 0 -1 fill=1000 (-0.25 0 -0.03515625) imp:p,e=1
1191 0 -10 1 imp:p,e=1
1192 0 10 imp:p,e=0
C
C end of cell cards
C

C
C surface cards
C
1      rpp -4 4 -3.76171875 3.76171875 -4.078125 4.078125
7      rpp -0.25 0.25 -0.03515625 0.03515625 -0.03515625 0.03515625
10     so 200.0
20     so 100.0
C
C end of surface cards
C

C
C data cards
C
mode p e
C
C
C source definition cards (upper direction)
C
SDEF X=D1 Y=D2 Z=4.08 ERG=D3 DIR=1 VEC=0 0 -1 PAR=2
SI1 -0.75 1.25 $ x axis
SP1 0 1
SI2 -3.77 3.77 $ y axis
SP2 0 1
SI3 0.000 0.219 0.438 0.658 0.877 1.096 1.315 1.534 1.753 1.973
      2.192 2.411 2.630 2.849 3.068 3.288 3.507 3.726 3.945 4.164
      4.383 4.603 4.821 5.041 5.260
SP3 0.000e+00 2.115e-04 6.614e-04 4.581e-04 3.089e-04 2.215e-04
      1.697e-04 1.325e-04 1.062e-04 8.552e-05 7.128e-05 6.030e-05
      5.138e-05 4.314e-05 3.739e-05 3.032e-05 2.655e-05 2.300e-05
      1.942e-05 1.526e-05 1.196e-05 8.988e-06 5.826e-06 1.404e-06
      1.360e-08
C
C material cards
C
M1      6000 -0.701220          $ Paraffin wax material data
      1000 -0.120590
      17000 -0.178185
      7000 -0.000005
M2      6012 0.000125 7014 0.6869 8016 0.301248 18040 0.011727 $ Air
C
C tally cards
C

```

```
*f8:p,e ((1002 135i 1138)<1[1:1 -53:53 -57:58])  
C  
C number of source particles  
C  
nps 1e6  
C  
C print  
C  
prdmp 2j -1 2j
```

## VITA

Jongsoon Kim received his Bachelor and Master of Engineering degrees in agricultural engineering (Agricultural Machinery major) at Seoul National University, Seoul, Korea in 1996 and 1998, respectively. He entered the Agricultural Engineering Department at Texas A&M University in September 1999. He completed his Ph.D. in August 2007.

During his graduate study, he installed and operated 2 MeV Van de Graaff electron accelerators to perform irradiation research of agricultural products. He also developed and validated a methodology for dose calculation in electron beam irradiation of complex-shaped food using the Monte Carlo method and CT scan technology. He has received a College of Engineering Endowed fellowship for 2004-2005, and published four articles in major scientific journals.

He may be reached at the Department of Biological & Agricultural Engineering, Texas A&M University, College Station, TX 77843-2117. His email address is [jongsoonkim@hotmail.com](mailto:jongsoonkim@hotmail.com).